Industrial Mathematics and Statistical Modeling Workshop for Graduate Students, July 21 - July 29, 2003

Edited by H.T. Banks, Pierre Gremaud, Jeffrey B. Hood, Alan Karr, Negash G.Medhin, and Ralph C. Smith.

Participants

Graduate Students

1. Ananthasayanam, Balajee, Clemson University
2. Bakewell, Edward, University of North Carolina-Wilmington
3. Bao, Yujuan, Duke University
4. Bergeron , Deana, Louisiana State University
5. Chan, Edna , North Carolina State University
6. Chen, Pengwen, University of Florida
7. Choe , Dong-Kyoung , North Carolina State University
8. Davis, Jimena, Clemson University
9. Edmonds , Bartlett , Virginia Commonwealth University
10. Ernstberger , Jon , Murray State University
11. Fricks , John , University of North Carolina, Chapel Hill
12. Ghosh , Krishnendu , University of Wisconsin-Milwaukee
13. Gilbert , James , University of South Florida
14. Grove , Sarah , Youngstown State University
15. Huang , Yujun , Georgia Institute of Technology
16. Jackson , Billy , University of Georgia
17. Jalali , Mohmmadreza , University of North Carolina-Charlotte
18. Jiang , Dongming , University of Cincinnati
19. Kala , Sirish , Mississippi State University
20. Lapin, Serguei, University of Houston
21. Lavrik , Ilya , Georgia Institute of Technology
22. Lawler , Stacey , Murray State University
23. Malaugh , James , University of Alabama at Birmingham
24. Minh , Ha Quang , Brown University
25. Nfodjo , David , University of Louisville

26. Rus , George , Western Illinois University
27. Sabuwala , Adnan , University of Florida
28. Samyono Widodo , Old Dominion University
29. Schoen, Rob, University of North Carolina-Asheville
30. Stroud , Lara , North Carolina State University
31. Thatcher , Aaron , University of North Carolina-Wilmington
32. Twagilimana , Joseph , University of Louisville
33. White , Gentry , University of Missouri-Columbia
34. Wong , Andrea , University of North Carolina-Greensboro
35. Xu , Xiangrong , Florida State University
36. Zeng , Bo , Purdue University
37. Zhou, Yingchun, Boston University

Problem Presenters

1. David Dausch, and Scott, Goodwin, MCNC Research and Development Institute
2. Hunter, William, C., Federal Reserve Bank of Chicago
3. Karr, Alan, National Institute of Statistical Sciences
4. Barton, Hugh, and Setzer, Woodrow, Environmental Protection Agency
5. Royal, Tony, Jenike & Johanson, Inc.
6. Maldague, Pierre, Jet Propulsion Laboratory

Faculty Advisors

1. Banks, H.T
2. Buche, Robert
3. Gremaud, Pierre
4. Haider, Mansoor
5. Ito, Kazi
6. Li, Zhilin
7. Pang, Tao
8. Smith, Ralph
9. Tran, Hien

Contents

Preface

This volume contains the proceedings of the Industrial Mathematics Modeling Workshop for Graduate Students that was held at the Center for Research in Scientific Computation at North Carolina State University (NCSU), Raleigh, North Carolina, July 21 - July 29, 2003. This workshop which was the ninth one held at NCSU brought together 38 graduate students. These students represented a large number of graduate programs including Brown University, Boston University, Clemson University, Duke University, Florida State University, Georgia Institute of Technology, Louisiana State University, Mississippi State University, Murray State University, North Carolina State University, Old Dominion University, Purdue University, UNC Chapel Hill, UNC Charlotte, UNC Wilmington, University of Alabama at Birmingham, University of Cincinnati, University of Florida, University of Georgia, University of Houston, University of Louisville, University of Missouri-Columbia University of North Carolina-Asheville, University of North Carolina-Greensborro, University of South Florida, Virginia Commonwealth University, Western Illinois University, Youngstown State University.

The students were divided into six teams to work on "industrial mathematics" problems presented by industrial scientists. These were not the neat, well-posed academic exercises typically found in coursework, but were challenging real world problems from industry or applied science. The problems, which were presented to the students on the first day of the workshop, required fresh insights for their formulation and solution. Each group spent the first eight days of the workshop investigating their project and then reported their findings in half-hour public seminars on the last day of the workshop.

The following is a list of the presenters and the projects they brought to the workshop.

- **David Dausch and Scott Goodwin** (MCNC Research and Development Institute) *Electrostatic Operation and Curvature of a MEMS Flexible Film Actuator*
- **William C. Hunter** (Federal Reserve Bank of Chicago) *Rational Price Limits/Circuits Breakers in Futures/Equity Markets*
- **Alan Karr** (National Institute of Statistical Sciences) *Modeling of Conductivity of Cement*
- **Hugh Barton and Woodrow Setzer** (Environmental Protection Agency) *Evaluating a Physiologically-Based Pharmacokinetic Model Proposed for Use in Environmental Risk Assessment*
- **Tony Royal** (Jenike & Johanson, inc) *Effect of Interstitial Gas on Powder Flow*
- **Pierre Maldague** (Jet Propulsion Laboratory) *Planning and Scheduling Strategy for Non-deterministic Events*

These problems represent a broad spectrum of mathematical topics and applications. Although nine days is a short time for a full investigation of some of the aspects of such industrial problems, the reader will observe remarkable progress on all projects.

We, the organizers, strongly believe that this type of workshop provide very valuable non-academic research related experiences for graduate students while contributing to the research efforts of industrial participants. In addition, this type of activity facilitates the development of graduate students' ability to communicate and interact with scientists who are not traditional mathematicians but require and employ mathematical tools in their work. By providing a unique experience of how Mathematics is applied outside Academia, the workshop has helped many students in deciding what kind of career they aspire to. In some cases in past workshops,

this help has been in the form of direct hiring by the participating companies. By broadening the horizon beyond what is usually presented in graduate education, students interested in academic careers also find a renewed sense of excitement about Applied Mathematics.

The success of the workshop was greatly enhanced by active participation in a very friendly atmosphere and almost uninterrupted work during the nine days of attendance. The organizers are most grateful to participants for their contributions. Funding for the workshop was provided by the Statistical and Applied Mathematical Sciences Institute (SAMSI) with additional financial support, personnel, and facilities provided by the Center for Research in Scientific Computation (CRSC) and the Department of Mathematics at North Carolina State University. Finally, we would like to thank Brenda Currin, Kathleen McGowan, Robin Eason-Ryan, and Rory Schnell for their efforts and help in all administrative matters. We are also grateful to Brian Adams, Brandy Benedict, and Nathan Gibson for their help in providing transportation, setting up computer accounts, and many other ways that made the workshop a success.

H.T. Banks, Pierre Gremaud, Alan Karr, Negash G. Medhin, Ralph Smith
Raleigh, 2003.

Chapter 1

Electrostatic Operation and Curvature Modeling for a MEMS Flexible Film Actuator

Bartlett Edmonds, Jr.[1], Jon Ernstberger[2], Krishnendu Ghosh[3], James Malaugh[4], David Nfodjo[5], Widodo Samyono[6], Xiangrong Xu[7]

Problem Presenters:
David Dausch and Scott Goodwin
MCNC Research and Development Institute

Faculty Mentor:
Ralph Smith
North Carolina State University

Abstract

In this investigation we develop a mathematical model to simulate the actuation of a multilayer metallic strip. In the first step of the model development, we employ the theory of Judy [4] and Timoshenko [5] to quantify the radius of curvature in the unimorph due to differing thermal coefficients in the constituent materials. The resulting radius of curvature is subsequently used to compute the voltage required to uncurl the actuator. Numerical experiments were performed with the model and the trends were found to be in agreement with experimental data.

1.1 Introduction and Motivation

The electrostatic flexible film actuator, also known as the "Artificial Eyelid," is a unique MEMS (Micro-Electronic Mechanical System) actuator fabricated from polyimide and thin metal films which provide high mechanical displacement (100's of microns) and high operational frequency (>5 kHz). The device is comprised of a polyimide/Au/polyimide structure in the flexible film portion of the actuator and a metal or transparent

[1]Virginia Commonwealth University
[2]North Carolina State University
[3]University Wisconsin-Milwaukee
[4]University of Alabama at Birmingham
[5]University of Louisville
[6]Old Dominion University
[7]Florida State University

electrode on the substrate (Si, quartz, sapphire, etc.) surface. Actuation of the device is achieved by applying a voltage between the electrode in the flexible film and the electrode on the substrate, causing the flexible film to flatten or uncurl across the substrate surface due to electrostatic attraction. When the voltage is removed, the actuator recoils to its curled state. Applications of this device include optical shutters, electrical switches and microfluidic valves.

A sacrificial release layer film is deposited between the flexible film and the substrate is etched away after forming the flexible film portion. Due to stresses in the films caused by thermal expansion mismatch during the polyimide cure at 410^o C, removal of the release film causes the flexible film portion of the actuator to curl. The degree of curl can be altered by changing the thicknesses of the flexible film constituents, and the electrostatic operating voltage is dependent on the radius of curvature (and thus stress) of the film. Actuators with tight curl have operating voltage in the range of 220-340 V, whereas actuators with less curl operate in the range of 100-180 V.

The objective of this project is to develop a baseline characterization method for determining the expected operating voltage for a given radius of curvature or film stress. The assumption is that the thermal stresses causing the film to curl must be overcome by the electrostatic force in order to uncurl the actuator. This should provide the threshold voltage where the actuator begins to uncurl. Concurrently, we would like to confirm our method for determining the radius of curvature expected in the actuator based on film thicknesses and mechanical properties. We currently perform calculations based on the mathematical model proposed by Judy [4] and Timoshenko [5]. The current calculation provides reasonably accurate trends, but further optimization is needed in the model.

1.2 Modeling Issues to Predict Curvature and Displacement as Functions of Material Proportion

The different actuator models are constructed using appropriate mathematical relations to predict curvature and displacement as functions of material thickness. The model used for actuator simulation is quantified using characteristics of the material and temperature. Experiments were carried out to evaluate the variation of the thickness of the top layer of the multilayer strip with the radius of curvature of the actuator. The mathematical model for the actuator, used for computing the operating voltages for various dimensions of the radius of curvature of the actuator, is described by Judy [4] as

$$\frac{\sigma_1}{E_1} + \frac{P_1}{E_1 a_1 b} + \frac{a_1}{2\rho} = \frac{\sigma_2}{E_2} - \frac{P_2}{E_2 a_2 b} - \frac{a_2}{2\rho} \tag{1.1}$$

where a_1 and a_2 are the thicknesses of the layer, from top to bottom, E_1 and E_2 denote the respective Young's moduli, and b is the width of the strip. We also consider the ratios

$$m = \frac{E_1}{E_2}, n = \frac{a_1}{a_2}.$$

The equation gives an insight into the radius of curvature with respect to thickness of the material of the topmost layer. The force required to uncurl the actuator is calculated from the radius of curvature specified by the model. Hence the electrostatic voltage can be computed to uncurl the actuator.

1.2.1 Two-Layer Case

The model of the two-layer case was developed by using the models of Judy [4] and Timoshenko [5]. Both authors describe the motion of small cantilevers (Timoshenko in relation to thermostats). Although the films that are discussed in this paper have notably different properties, the two previously mentioned papers make note of properties that also apply to this problem.

The model summarizes the forces placed on the bi-metal strip and can be applied to the films given different Young's moduli E_i, residual stresses σ_i, axial force P (since it is assumed that although there are two axial forces, in a two-layer case they are the same), and the force due to curvature (ρ).

Combining the methods used in both [4] and [5], we propose a new model to compute the radius of the actuator:

$$\alpha_1 \Delta T + \frac{\sigma_1}{E_1} + \frac{P_1}{E_1 a_1 b} + \frac{a_1}{2\rho} = \alpha_2 \Delta T + \frac{\sigma_2}{E_2} - \frac{P_2}{E_2 a_2 b} - \frac{a_2}{2\rho}. \tag{1.2}$$

Here α is the corresponding coefficient of expansion for each layer of the film and ΔT is the change in temperature of the respective layer. Note that a_i is the thickness of the strip and that b is the width of the strip (which Timoshenko takes as unity).

With manipulation the force due to curvature (ρ) can be found to be

$$\frac{1}{\rho} = \frac{(\alpha_2 - \alpha_1)\,\Delta T - \frac{\sigma_1}{E_1} + \frac{\sigma_2}{E_2}}{\frac{a_1+a_2}{2} + 2\left(\frac{E_1 a_1^3 - E_2 a_2^3}{12}\right)\left(\frac{1}{E_1 a_1} - \frac{1}{E_2 a_2}\right)}. \tag{1.3}$$

1.2.2 Three-Layer Case

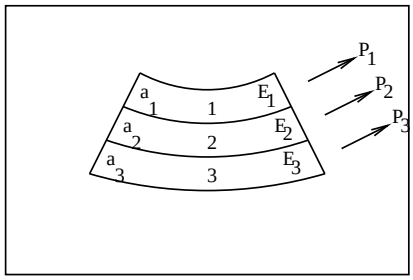

Figure 1.1: Three-layer film with respective Young's moduli, thicknesses, and thermal conductivity coefficients.

For the previous two-layer case, we had seen that Judy [4] and Timoshenko [5] give models and examples. However, the three-layer case depicted in Figure 1 is similar in nature and is modeled on the assumptions similar to that of two-layered case. There is a relation for the axial stress P_i given by

$$P_1 - P_2 - P_3 = 0. \tag{1.4}$$

Going through P_1 the sum of the moments is given by

$$m_1 + m_2 + m_3 = P_2\left(\frac{a_2}{2} + \frac{a_1}{2}\right) + P_3\left(\frac{a_3}{2} + a_2 + \frac{a_1}{2}\right) \tag{1.5}$$

There is a relationship established between ρ and the moment m_i for each i from one to three.

$$m_1 = \frac{E_1 I_1}{\rho}, m_2 = \frac{E_2 I_2}{\rho}, m_3 = \frac{E_3 I_3}{\rho}.$$

There is (similar to the two-layer case) a relationship made between the stresses between the first and second layers and the second and third layers.

$$\alpha_1 \Delta T + \frac{\sigma_1}{E_1} + \frac{P_1}{E_1 a_1 b} + \frac{a_1}{2\rho} = \alpha_2 \Delta T + \frac{\sigma_2}{E_2} - \frac{P_2}{E_2 a_2 b} - \frac{a_2}{2\rho} \tag{1.6}$$

$$\alpha_2 \Delta T + \frac{\sigma_2}{E_2} - \frac{P_2}{E_2 a_2 b} + \frac{a_2}{2\rho} = \alpha_3 \Delta T + \frac{\sigma_3}{E_3} - \frac{P_3}{E_3 a_3 b} - \frac{a_3}{2\rho}. \tag{1.7}$$

Finally, the connection between ρ and the axial stresses P_i can be expressed as

$$\frac{E_1 I_1 + E_2 I_2 + E_3 I_3}{\rho} = P_2\left(\frac{a_2}{2} + \frac{a_1}{2}\right) + P_3\left(\frac{a_3}{2} + a_2 + \frac{a_1}{2}\right). \tag{1.8}$$

If we solve our system of equations for ρ, we're left with

$$\frac{1}{\rho} = \frac{z}{y + \frac{a_2+a_3}{2}} \tag{1.9}$$

where

$$z = x - \Delta T\left(\alpha_2 - \alpha_3\right) + \frac{\sigma_3}{E_3} - \frac{\sigma_2}{E_2} \tag{1.10}$$

$$x = \frac{\sigma_2 a_2}{E_2 a_2} + \frac{a_1 + a_2}{E_3 a_3\left(a_3 + a_1 + 2a_2\right)} \tag{1.11}$$

$$y = 2\frac{E_1 I_1 + E_2 I_2 + E_3 I_3}{E_3 b a_3 (a_3 + a_1 + 2a_2)}. \tag{1.12}$$

1.2.3 Five-Layer Case

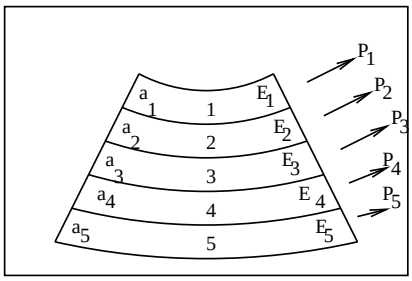

Figure 1.2: Five-layer varies from the three-layer case in that two chromium layers surround the inner gold conducting layer.

The five-layer case depicted in Figure 2 is a direct extension from the three-layer case in that two layers of chromium were added around the original gold-conducting layer. However, both cases are similar. The basic equation to start with:

$$P_1 - P_2 - P_3 - P_4 - P_5 = 0. \tag{1.13}$$

Going through P_1, the sum of the moments is given as

$$\begin{aligned} m_1 + m_2 + m_3 + m_4 + m_5 &= P_2\left(\frac{a_2}{2} + \frac{a_1}{2}\right) + P_3\left(\frac{a_3}{2} + a_2 + \frac{a_1}{2}\right) \\ &+ P_4\left(\frac{a_4}{2} + a_3 + a_2 + \frac{a_1}{2}\right) + P_5\left(\frac{a_5}{2} + a_4 + a_3 + a_2 + \frac{a_1}{2}\right). \end{aligned} \tag{1.14}$$

The moments, m_j, are once again given by

$$m_j = \frac{E_j I_j}{\rho} \text{ for } j = 1, \ldots, 5. \tag{1.15}$$

This yields the resulting four relations

$$\alpha_1\Delta T + \frac{\sigma_1}{E_1} + \frac{P_1}{E_1 a_1 b} + \frac{a_1}{2\rho} = \alpha_2\Delta T + \frac{\sigma_2}{E_2} - \frac{P_2}{E_2 a_2 b} - \frac{a_2}{2\rho} \tag{1.16}$$

$$\alpha_2\Delta T + \frac{\sigma_2}{E_2} - \frac{P_2}{E_2 a_2 b} + \frac{a_2}{2\rho} = \alpha_3\Delta T + \frac{\sigma_3}{E_3} - \frac{P_3}{E_3 a_3 b} - \frac{a_3}{2\rho} \tag{1.17}$$

$$\alpha_3\Delta T + \frac{\sigma_3}{E_3} - \frac{P_3}{E_3 a_3 b} + \frac{a_3}{2\rho} = \alpha_4\Delta T + \frac{\sigma_4}{E_4} - \frac{P_4}{E_4 a_4 b} - \frac{a_4}{2\rho} \tag{1.18}$$

$$\alpha_4\Delta T + \frac{\sigma_4}{E_4} - \frac{P_4}{E_4 a_4 b} + \frac{a}{2\rho} = \alpha_5\Delta T + \frac{\sigma_5}{E_5} - \frac{P_5}{E_5 a_5 b} - \frac{a_5}{2\rho}. \tag{1.19}$$

The relation between the E_jI_j's and ρ are given by the following equation

$$\frac{\sum_{j=1}^{5} E_jI_j}{\rho} = \frac{EI}{\rho} = \sum_{k=2}^{5} P_kL_k \tag{1.20}$$

where the $L_i's$ are denoted by

$$L_2 = \frac{a_2}{2} + \frac{a_1}{2} \tag{1.21}$$

$$L_3 = \frac{a_3}{2} + a_2 + \frac{a_1}{2} \tag{1.22}$$

$$L_4 = \frac{a_4}{2} + a_3 + a_2 + \frac{a_1}{2} \tag{1.23}$$

$$L_5 = \frac{a_5}{2} + a_4 + a_3 + a_2 + \frac{a_1}{2}. \tag{1.24}$$

After following a similar process, as was found in both the two and the three-layer case, ρ was specified by

$$\frac{1}{\rho} = \frac{(M+N)}{\frac{a_3+a_2}{2} - \frac{EI}{L_2E_2a_2b}} \tag{1.25}$$

where

$$M = \alpha_3\Delta T + \frac{\sigma_3}{E_3} - \frac{P_3}{E_3a_3b} + \frac{L_3}{L_2E_2a_2b} + \frac{L_4E_4a_4}{L_2E_3a_3E_2a_2b} + \frac{L_5E_5a_5}{L_2E_2E_3a_2a_3b} \tag{1.26}$$

$$N = -\alpha_2\Delta T - \frac{\sigma_2}{E_2} - \frac{L_4k}{L_2E_2a_2b} - \frac{L_5q}{L_2E_2a_2} \tag{1.27}$$

and

$$k + \frac{P_3E_4a_4}{E_3a_3} = P_4, \tag{1.28}$$

$$q + \frac{\left(k + \frac{P_3E_4a_4}{E_3a_3}\right)E_5a_5}{E_4a_4} = P_5. \tag{1.29}$$

We can solve the system of equations using a line search Newton Method.

1.3 Modeling Of Electrostatic Forces Required to Unbend Eyelid

In the manufacturing process, as discussed earlier, the device is curled by internal forces leading to a tip deflection δ. The reactive force, R, is the force necessary to annihilate the deflection (i.e., to flatten or uncurl the device; See Timoshenko [5]). Here R is defined as

$$R = \frac{48EI}{EL^3}\rho\left(1 - \sqrt{1 - \left(\frac{L}{\rho}\right)^2}\right) \tag{1.30}$$

(See Young [6]). In a parallel plate capacitor, the electrostatic force F between the plates is given by

$$F = \frac{1}{2}\frac{\epsilon AV^2}{d^2} \tag{1.31}$$

where d is the distance between the capacitor plates, ϵ is the dielectric constant, A is area, and V is applied voltage. This can be modified to apply to the case where the top plate is curved. Similarly, we can look at the electrostatic force exerted upon the actuator arm.

$$\mathcal{F} = \int_0^L \frac{1}{2}\frac{\epsilon AV^2}{[d+\delta(l)]^2}dl \tag{1.32}$$

where L is the length corresponding to Figure 1.3 and

$$\delta(l) = \rho \left[1 - \sqrt{1 - \left(\frac{l}{\rho} \right)^2} \right]. \tag{1.33}$$

Setting $F = R$ yields the relation

$$V = \left[\frac{96EI}{5L^3 \epsilon A} \frac{\rho \left(1 - \sqrt{1 - \left(\frac{L}{\rho} \right)^2} \right)}{\int_0^L \frac{1}{[d+\delta(l)^2]} dl} \right]^{\left(\frac{1}{2}\right)} \tag{1.34}$$

specifying the voltage required to actuate the device.

1.3.1 Computation of an Equivalent EI

The equivalent flexural beam strength EI is computed in order to calculate the reactive force and therefore the voltage. In this study, we calculate EI using an equivalent width technique.

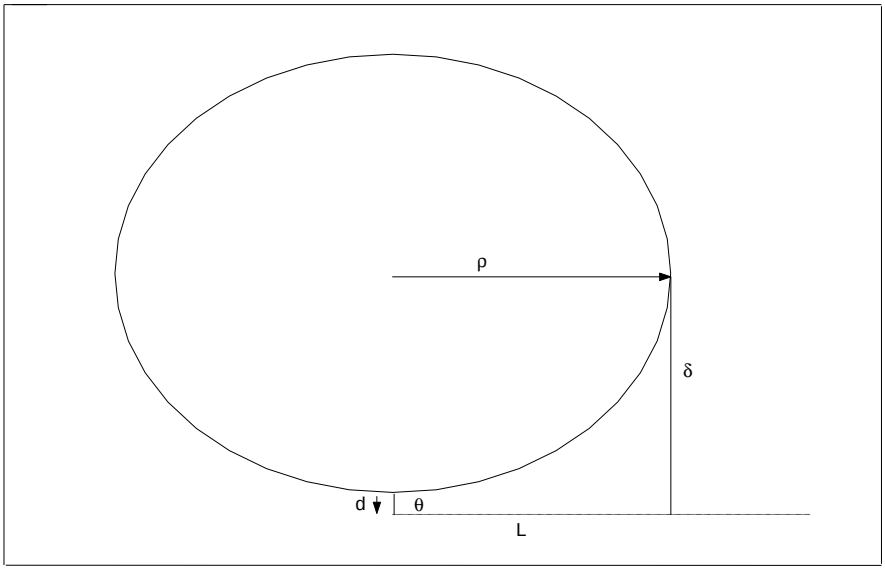

Figure 1.3: Geometry used to visualize the motion of the film.

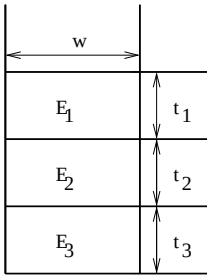

Figure 1.4: Side view of the individual layers given respective Young's moduli E_i, thicknesses t_i and lengths w.

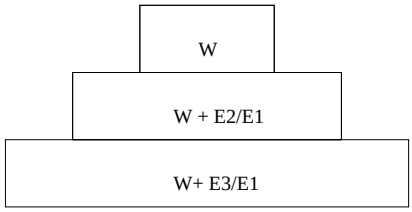

Figure 1.5: Side-view depicting increasing widths due to addition of the ratio of the Young's moduli.

First, a cross section of the beam width w is considered in Figure 1.4. In general, each section has a different Young's modulus (E=stress/strain). One of the materials is chosen as the assumed material (with Young's Modulus E_a). This material maintains the width of the cross-section. The widths of the other materials are given by $w + E_i/E_a$, where E_i is the Young's modulus of the material in question. This leads to a cross section like the one in Figure 1.5 in which the entire beam consists of the assumed material.

Secondly, the centroid ($\bar{y}$) must be located using the relation

$$\bar{y}_n = \frac{\sum_{i=1}^{n} A_i' t_i h_i}{\sum_{i=1}^{n} A_i'} \tag{1.35}$$

where $A_i^{'}$ is the area of the modified beam section, h_i is the height of the center of the i^{th} beam section, t denotes thickness of the material, and n is the number of layers.

Finally, the inertial moment ($I^{'}$) for the centroidal axis must be determined. This can be acquired from

$$I' = \sum_{i=1}^{n} \frac{w_i' \left(t_i^3\right)}{12} + A_i' \left(h_i - \bar{y}\right)^2 \tag{1.36}$$

where w' is the width of the modified beam section. The equivalent flexural beam strength is given by $EI = E_a I'$.

1.4 Numerical Examples

With a varying array of MEMS, it was thought prudent to consider trends involving this model rather than to look at specific cases. In the two and three-layer cases, we examine varying aspects which are made easier to understand due to the restriction of fewer layers. In the five-layer case we sought to look at trends by examining computed results and seeing if our model was giving desired results for varying a_i.

1.4.1 Computation of ρ For Two-Layer Case

Using the data provided by MCNC that was known or physically observed, our values for ρ were easily computed for varying the top layer of the multilayered strip. This information was among the most coveted in that the initial curvature can be optimized for minimum voltage and still be useful. The two-layer case seemed most reasonable to view this change.

Figure 1.6 demonstrates the variation of ρ with thickness of the top layer of the multilayered strip. The model used to compute the phenomena is based on a modified form of Judy [4]. Notice that the figure confirms that as the top layer of the polyimide becomes thicker, the radius of curvature increases. This lends to the idea that not only does the top-layer work against the curvature but it also lessens resistance against the electrical forces wishing to bring the film to contact with the fixed layer on the substrate.

1.4.2 Computation of ρ versus Temperature for Three-Layer Case

An investigation of the relationship between change in temperature in the cooling processes of the polyimide versus ρ was also desired. When our computations were completed, we noted that for greater temperature changes during the cooling of the polyimide, the radius of curvature of the film decreases rapidly. Once again

we aimed for the trends of the model. In Figure 1.7, we present the model predictions which we see agree to within a factor of ten.

1.4.3 Computation of ρ for Five-Layer Case

We were left with a non-linear system of equations that we had to solve for ρ. The line search Newton's Method (which converges quadratically provided a reasonably accurate starting point) was the tool of choice and left us with satisfying results.

Thickness (a_3)	Measured	Calculated
5.00e-08 m.	45μ m	4.5021e-05 m
4.50e-07 m.	120μ m	1.1994e-04 m
8.00e-07 m.	250μ m	2.5689e-04 m

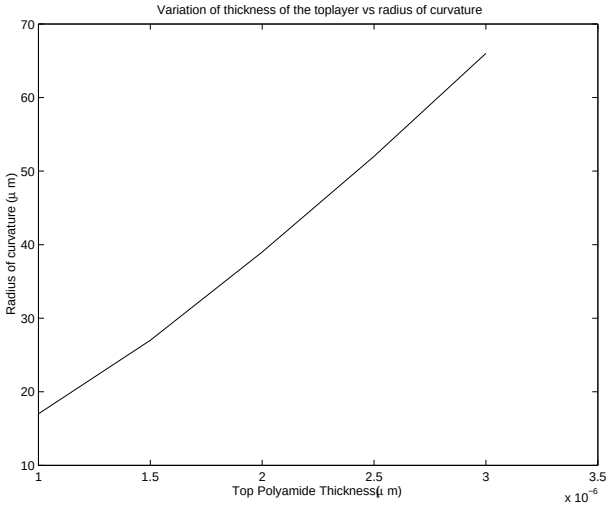

Figure 1.6: Dependence of the radius of curvature on the thickness of the top polyimide layer.

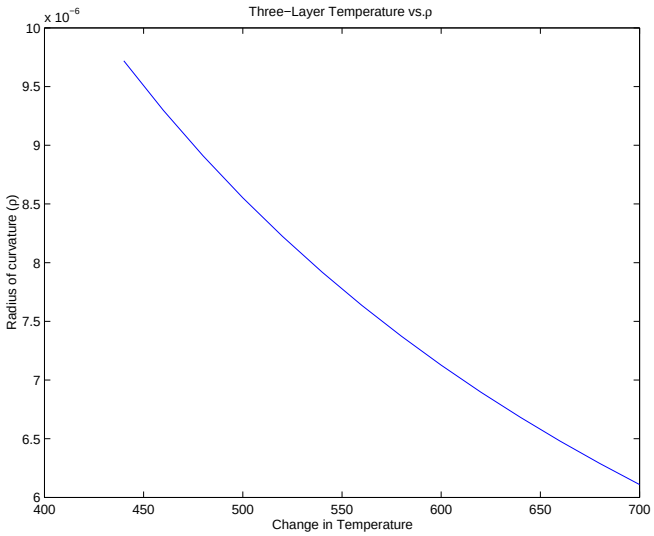

Figure 1.7: Decrease in the radius of curvature as a function of temperature.

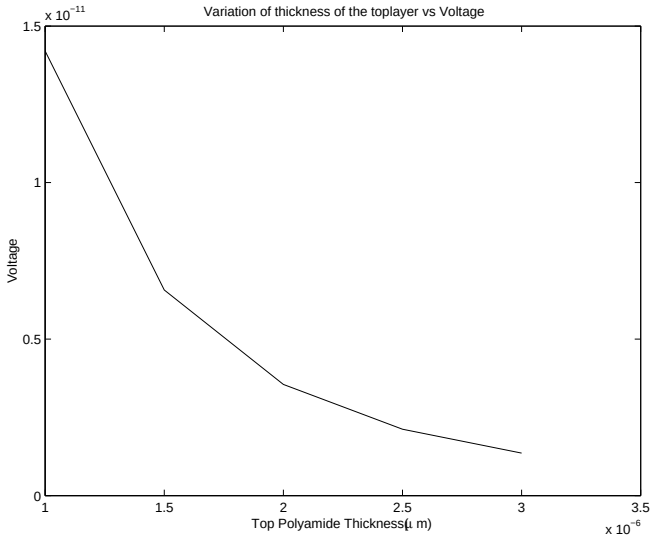

Figure 1.8: Decrease in the voltage required to lower the cantilever as a function of the thickness of the top polyimide layer.

Notice that the thicknesses of the layer a_3 increase according to the table. In actual laboratory measurements, the film was shown to have radii of 45, 120 and 250 μm. According to the model, using the line search, our measurements had approximately .000467, .0005, and 2.8 percent relative errors.

1.4.4 Computation of $E(V)$

The computation of $E(V)$ is little more than an integral which may or may not be difficult to solve depending upon $\delta(l)$ given ρ, EI, and L. This can be computed using either textbook methods or by computer. What becomes more interesting are the variations of voltage against both top-layer thickness and radius of curvature.

In the two layer case, top-layer thickness was varied in order to see how the voltage varied. According to Figure 1.8, as the thickness of the top layer increases the voltage drops. This will be dealt with next.

According to Figure 1.9, the phenomenon is that, as radius of curvature increases, the voltage required to actuate the device lowers. As the radius of the arm increases, the distance to the substrate is lowered. If one recalls, due to (1.31), the electrostatic force between the two plates increases and the voltage required goes to zero according to (1.34).

The three-layer case was the only one modeled in this situation as opposed to the five-layer case. It was reasoned that the five and three-layer cases were similar as far as conductivity. The extra two layers were other metal conductors surrounding the gold. However it was reasoned that their conductivity was similar to that of the gold and therefore should simply be treated as one-layer.

1.5 Conclusion

The first goal of this investigation was to accurately the forces which cause the film (two, three, or five-layers) to bend. Using a combination of models, we constructed systems of equations describing these curvatures that allow us to describe the radii of the structure for other given factors. Numerically, it was shown that the behavior of our model was qualitatively similar to the results gathered in the laboratory. This was a necessary result to complete the second goal.

The second goal of this paper was to model the electric forces acting upon the MEMS when attempting to actuate the device. Modeling the voltage over the length of the structure was an definitely an area of interest. The numerics of our model further validated its accuracy by giving us the trends that analysis of our voltage modeling equations led us to believe would occur.

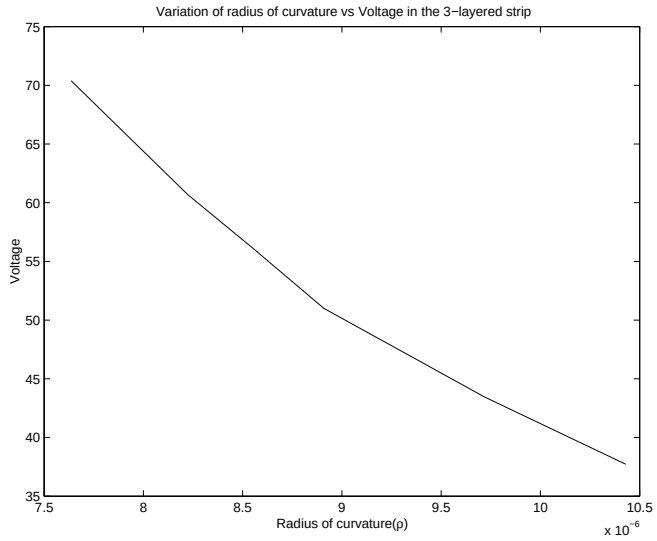

Figure 1.9: Voltage required to actuate the lever arm as a function of the radius of curvature.

Bibliography

[1] M. Capozzoli, J. Gopalakrishnan, K. Hogan, J. Massad, T. Tokarchik, S. Wilmarth, H.T. Banks, K.M. Mossi and R.C. Smith, "Modeling aspects concerning THUNDER actuators," Proceedings of the SPIE, Smart Structures and Materials 1999, Volume 3667, pp. 719-727, 1999.

[2] A.K. Chinthakindi and P.A. Kohl, "Electrostatic actuators with intrinsic stress gradient," *Journal of the Electrochemical Society,* 149(8), H139-H145, 2002.

[3] G. Daspit, C. Martin, J-H. Pyo, C. Smith, H. To, K.M. Furati, Z. Ounaies and R.C. Smith, "Model development for piezoelectric polymer unimorphs," Proceedings of the SPIE, Smart Structures and Materials 2002, Volume 4693, pp. 514-524, 2002.

[4] M.W. Judy, Y-H. Cho, R.T. Howe and A.P. Pisano, "Self-adjusting microstructure (SAMS)", IEEE, pp. 51-56, 1991.

[5] S. Timoshenko "Analysis of bi-metal thermostats," *Journal of the Optical Society of America*, 11, 233-255, 1925.

[6] R.J. Roark and W.C. Young, *Formulas for Stress and Strain*, McGraw-Hill, New York, 1975.

Chapter 2

Rational Price Limits/Circuit Breakers in Futures/Equity Markets

Deanna Bergeron[1] Billy Jackson[2] George Rus[3] Bo Zeng[4] Yingchun Zhou[5]

Problem Presenter:
William C. Hunter
Federal Reserve Bank of Chicago

Faculty Consultants:
Tao Pang and **Robert Buche**
Department of Mathematics, NC State University

Abstract

In this problem, we extend and generalize the model given by Ackert and Hunter to optimize price limits/circuit breakers on futures contracts via minimizing what is termed the Long Run Average Cost (LRAC). In their paper [A-H], Ackert and Hunter derive a model that successfully deals with futures markets modelled by the standard Brownian Motion. We attempt to generalize their ideas by considering the generalized and geometric Brownian Motion models. While we are unable to derive a closed form determination of the optimal price in terms of the running cost and the cost of trading interruptions due to the limit moves as they do in their paper, we are able to find the optimal price through numerical investigation of the problem, and in so doing, are able to derive likely candidates for closed form solutions.

2.1 Introduction and Motivation

Following the disastrous financial results of the market crisis in 1987, the Commodities Futures Trading Commission (CFTC), the Securities and Exchange Commission (SEC), the securities exchanges, and other regulators such as the Federal Reserve began to reconsider how securities markets and trading practices were regulated. The major outcome of this examination was the implementation of a more comprehensive system of trading halts and circuit breakers across the market along with the coordination of the functioning of these interventions between the equity and futures markets. In the case of futures markets, attention was focused on daily limits on futures prices. These limits in some sense regulate because if the price of the contract reaches

[1]Louisiana State University
[2]University of Georgia
[3]Western Illinois University
[4]Purdue University
[5]Boston University

these limits due to panic or excessive speculation, all activity in that market stops for a certain amount of time. The idea is that by stopping activity, traders in that market are given time to stop and rethink their positions. The hope is that by giving traders the chance to think rationally, the market will return to its normal operations. Thus, one advantage of price limits is that they allow for rationality to determine the market. Another advantage of limits is that their existence decreases the margin that brokers and exchanges require since the financial risks that they must bear is decreased by these limits in comparison with the larger risks that they would have to bear in a completely unregulated market (see [A-H]). Thus, determining appropriate limits can be extremely beneficial to the market.

However, one intrinsic problem with invoking price limits is that there is an associated cost with doing so. This cost comes at the expense of the market participants. By imposing limits, participants can sustain significant financial losses that are compounded daily in some markets by the failure of prices to move and their inability to trade into or out of positions in these periods. Inactivity and consistent losses are of course unattractive to any participant, and so markets in which the limits are inadequately set will become unappealing.

Thus, our problem is to find the optimal limit. Currently, there is no rigorously systematic way of determining these limits. Financial and economic analysts generally look at market history to determine them, but of course this is by no means necessarily optimal. With this in mind, it seems a mathematical analysis/procedure for determining the optimal limit would be both necessary and beneficial.

We are forced to keep in mind that our optimization problem is controlled by existing physical constraints. We know that if our limit is too wide, then participants (traders, brokers, and dealers) will withdraw from the market due to the significant risks that they will bear. In contrast, if our limit is too narrow, then the market is stopped more frequently, and the costs to the participants will be substantial. Thus our model will have to use these constraints in some way.

In [A-H], Ackert and Hunter undertook an examination of price limits imposed on several contracts traded on the Chicago Board of Trade (CBOT). This study, funded by the CBOT and the Chicago Board of Trade Clearing Corporation, sought to develop a model of optimal daily price limits following the reasoning of [K-T] to determine the optimal limit when market prices tend to follow the standard Brownian Motion model. The authors empirically tested their optimizing model and found that in general it could not be rejected for the majority of the contracts (price limits) they examined. Thus, we will try to use similar reasoning to analyze the optimal limits for the generalized and geometric Brownian Motion models. However, as will be seen, these models will become significantly more complex to analyze than the standardized case. Currently, the Federal Reserve Bank of Chicago's Financial Markets and Payment Systems Risk Unit and representatives of the Chicago futures and derivatives exchanges are reviewing the procedures by which price limits are imposed in their markets in anticipation of developing limit and circuit breaker (trading halt) policies that enhance the safety and soundness of the markets while maintaining their liquidity and efficiency. We hope that our work which follows provides insight to policy-makers as they grapple with this important challenge.

2.2 Existing Model

In [A-H], Ackert and Hunter let $F(t)$ represent the normalized futures price. That is, $F(t)$ is the difference of the current price and settlement price (typically the previous day's closing price). $C(T)$ represents the total cost of maintaining a contract as a sum of the running and interruption cost. Here, T is the stopping or hitting time associated with the limit. (Note that T is a random variable.) Then $C(T)$ is expressed as:

$$C(T) = \int_0^T h[F(t)]^2 dt + K\,. \tag{2.1}$$

where the first term on the right hand side of equation (1) is the running cost, which is proportional to the square of the futures price with proportionality constant h. K represents the cost of hitting the limit, thus making it the interruption cost. As T is defined as the first time that the futures price hits the limit (call it L), mathematically T is defined as:

$$T = \inf\{\, t \geq 0 \quad | \quad |F(t)| = L\}\,. \tag{2.2}$$

The Long Run Average Cost ($LRAC$) is defined as the quotient of the expected cost incurred during one cycle (i.e. the length of time before the price hits the limit) and the expected length of the typical cycle. Thus, Ackert and Hunter wanted to find the optimal limit L so that

$$LRAC = \frac{E[\, C(T) \;\mid\; F(0) = 0\,]}{E[\, T \;\mid\; F(0) = 0\,]} \tag{2.3}$$

is minimized. From here, they use results obtained from Karlin and Taylor's book [K-T] and show that

$$\begin{aligned} E[\, C(T) \;\mid\; F(0) = 0\,] &= \frac{hL^4}{6} + K \\ E[\, T \;\mid\; F(0) = 0\,] &= L^2\,. \end{aligned} \tag{2.4}$$

Thus, the function $C(L)$ (as a quotient of the corresponding expected values) to be minimized is

$$C(L) = \frac{K}{L^2} + \frac{hL^2}{6}\,. \tag{2.5}$$

Thus, taking the derivative with respect to L and setting this result equal to zero, we find that solving for the optimal L (call it L^*) gives

$$L^* = \left(\frac{6K}{h}\right)^{\frac{1}{4}}\,. \tag{2.6}$$

Ackert and Hunter then go on to justify using this model as a reasonable first approximation of the objective function of the exchange by arguing that the exchange has a vested long-term interest in making sure that the market operates smoothly, so that minimizing cost is a natural objective to try and achieve. The validity of this objective is further supported by the fact that the CBOT and its clearing house are mutual organizations which operate with the objective of providing members maximum service at minimum cost. They also note that the model makes intuitive economic sense by showing that as K increases, the optimal limit increases, and likewise, as h decreases, the optimal limit increases, thus satisfying the physical constraints of the problem set forth earlier. Finally, they test their model against actual data and find that in the majority of the markets tested, their model cannot be rejected statistically.

2.3 Governing Equations and Processes

To generalize the model given by [A-H], we generalize the reasoning provided by [K-T] used to determine the model. In this spirit, we provide a discussion of the relevant equations and processes involved and refer the reader to [K-T] (1981, pages 157-213 of Chapter 15 on Diffusion Processes) for justifications and appropriate conditions for the equations to hold.

Let a, b be the price limits. From now on, for notation reasons, we use $X(t)$ instead of $F(t)$ to denote the price process. Denote T the stopping time of $X(t)$ hitting the limits. First, we must determine functions $w(x)$ and $v(x)$ satisfying:

$$\begin{aligned} w(x) &= E\left[\int_0^T g(X(t))dt \;\mid\; X(0) = x\right] \\ v(x) &= E\,[\, T \;\mid\; X(0) = x\,]\,. \end{aligned} \tag{2.7}$$

Assume that the price process follows:

$$dX(t) = \mu(X(t))dt + \sigma(X(t))dw(t),$$

where $w(t)$ is a 1-dimensional standard Brownian motion. Karlin and Taylor show that if $g(x)$ is continuous and bounded on an appropriate region, $X(t)$ is a suitable diffusion process (i.e. for example, standard, general, or geometric Brownian Motion), then w and v satisfy the ordinary differential equations (ODEs):

$$\begin{aligned} -g(x) &= \frac{1}{2}\sigma^2(x)\frac{d^2w}{dx^2} + \mu(x)\frac{dw}{dx}, \quad a < x < b, \quad w(a) = w(b) = 0 \\ -1 &= \frac{1}{2}\sigma^2(x)\frac{d^2v}{dx^2} + \mu(x)\frac{dv}{dx}, \quad a < x < b, \quad v(a) = v(b) = 0 \end{aligned} \tag{2.8}$$

where $\mu(x)$ represents the drift (mean) of the distribution X and $\sigma^2(x)$) is the volatility (variance) of X. Thus, w and v are solutions of non-homogeneous linear ODEs with non-constant coefficients in general. It is worth noting that v is a special case of w if we think of v as the solution to the same equation as w with $g(x) = 1$.

Thus, to generalize the model given by [A-H], we generalize the expression for the $LRAC$. This is given by:

$$LRAC = \frac{E[\ C(T)\ \mid\ X(0) = x\ ]}{E[\ T\ \mid\ X(0) = x\ ]} \tag{2.9}$$

where now we may consider $X(t)$ as a suitable diffusion process (i.e. not necessarily the standard Brownian Motion) with an initial price that is not necessarily equal to zero, and T is defined as before.

Next, we describe the processes that will be used in our generalized model. We define the standard Brownian Motion as the stochastic process with $\mu(x) = \mu = 0$ and $\sigma^2(x) = \sigma^2 = 1$. We also consider some generalized Brownian motion with $\mu(x) = \mu \neq 0$ and variance $\sigma^2(x) = \sigma^2 \neq 1$. In additon, we consider the geometric Brownian Motion, which can be modelled by $Y(t) = e^{X(t)}$, where $X(t)$ is a generalized Brownian Motion. Note that in this model, geometric Brownian Motion never has negative values as $e^x > 0$, $\forall x$. Also note that this is another way of saying that $Y(t)$ has a log-normal distribution.

We generally prefer the geometric model to the generalized model because:

1. the geometric model is never negative.
2. the geometric model allows one to calculate the cost for **any** initial price (not just 0).
3. the geometric equation is governed by the stochastic differential equation:

$$dX(t) = \mu X(t)dt + \sigma X(t)dw(t)\,. \tag{2.10}$$

So that after dividing both sides by X(t), we obtain the equation

$$d\log X(t) = \left(\mu - \frac{1}{2}\sigma^2\right)dt + \sigma dw(t)\,. \tag{2.11}$$

This last equation tells us then that the rate of return follows the generalized Brownian Motion since $\log X(t)$ is a generalized Brownian Motion, which in turn implies that the price $X(t)$ in reality tends to follow the geometric Brownian Motion.

2.4 New Models by Distribution

Recall equation (1):

$$C(T) = \int_0^T h[X(t)]^2 dt + K\,.$$

As we have already seen, [A-H] have dealt with the optimization of the model when $X(t)$ follows a standardized Brownian Motion. We now try to generalize their results by considering the cases when $X(t)$ is a generalized Brownian Motion and a geometric Brownian Motion. The generalized case will be divided into two subcases: $\mu = 0$ and $\mu \neq 0$.

2.4.1 Generalized Brownian Motion

$\mu = 0,\ \sigma^2(x) = \sigma^2 \neq 1$

This case is particularly interesting. We initially modelled this case by using two subcases, namely the case with starting price $x = 0$ and the case with starting price $x \neq 0$. But in doing this, we found (amazingly) that in actuality our solution is independent of the starting/initial price, and so we will treat these two cases as one.

Note that in this case, the ODEs from equation (8) governing our model are:

$$-hx^2 = \frac{1}{2}\sigma^2 \frac{d^2w}{dx^2}, \quad a < x < b, \quad w(a) = w(b) = 0$$

$$-1 = \frac{1}{2}\sigma^2 \frac{d^2v}{dx^2}, \quad a < x < b, \quad v(a) = v(b) = 0$$

since $\mu = 0$ and $g(x) = hx^2$. Using either elementary integration techniques for solving separable non-homogeneous linear equations with constant coefficients or a Computer Algebra System (CAS) such as Maple, one obtains the following expressions for v and w:

$$v(x) = -\frac{x^2}{\sigma^2} + \frac{(a+b)x}{\sigma^2} - \frac{ba}{\sigma^2}$$

$$w(x) = -\frac{hx^4}{6\sigma^2} + \frac{h(a^3 + ba^2 + b^2a + b^3)x}{6\sigma^2} - \frac{hba(a^2 + ba + b^2}{\sigma^2}$$

Now we are trying to find a and b such that $b - a = 2L$, thus giving a uniform limit, and so we let $a = x - L$ and $b = x + L$. Then our $LRAC$ in terms of x and L is:

$$LRAC(x, L) = \frac{w(x, L) + K}{v(x, L)} = \frac{6hx^2L^2 + hL^4 + 6K\sigma^2}{6L^2}$$

We want the optimal L (again call it L^*), and so we take the derivative with respect to L of the equation above to obtain:

$$\frac{d(LRAC)}{dL} = \frac{hL^4 - 6K\sigma^2}{3L^3}.$$

Setting this equation equal to zero and solving for L^*, we see that

$$L^* = \left(\frac{6\sigma^2 K}{h}\right)^{\frac{1}{4}}$$

This is consistent with the result that [K-T] obtained for the standardized case. Thus, varying σ in this case merely varies our solution by an appropriate constant (namely $|\sigma|^{\frac{1}{2}}$). Notice that when the derivative with respect to L is taken, our term involving the initial price vanishes from the expression, which implies that in this case the optimal solution does not depend on the initial price, a fact we find most interesting and bizarre.

$\mu \neq 0,\ \sigma^2(x) = \sigma^2 \neq 1$

The introduction of a drift term in this case complicates the model severely. First, note that for $\mu \neq 0$, the solutions to the ODEs given in equation (8) will now involve exponential functions of μ, σ, x, and L with coefficients in terms of μ, σ, x, L, K, and h. This, in turn, results in a much more complicated expression for the $LRAC$ function and its derivative. In fact, if one uses a CAS to compute the expression for the $LRAC$ and its derivative, he will obtain expressions containing a number of terms on the order of 20. Thus, we have a sum of exponentials in the 6 parameters μ, σ, h, K, x, and L, and so the there is little hope of finding a closed form solution in a short period of time as was done in the previous cases. Instead, we began looking at numerical solutions by running many simulations.

After running many simulations, we found several interesting things happening. First we noticed that the function for the $LRAC$ when graphed seemed to be symmetric with respect to the y-axis. We used Maple to

test this hypothesis by computing the difference $LRAC(-L) - LRAC(L)$ and found that indeed this difference is zero, and so our hypothesis is correct. This result is particularly important because when one uses a CAS to try to compute L^*, the CAS uses a numerical algorithm in the implementation of the CAS's numeric solve command (which in the case of Maple is the fsolve command), and the first result that is obtained is usually the one reported to the user (which means it can be positive or negative). Thus, if the system finds a negative L as a zero of the derivative function, we can simply take its absolute value and argue that the absolute value is optimal since the $LRAC$ function is symmetric with respect to the $y - axis$. We argue that our code will produce the minimum value of the $LRAC$, thus being the optimal solution, by examining the graph of the derivative. When one plots the derivative, he will find that the derivative is negative to the left of the point where the function crosses the $x - axis$, and it is positive to the right of that point. Thus, we know that elementary calculus guarantees that the point is a local minimum. We argue that this point is actually a minimum globally because if indeed there were another minimum, it would occur at a limit value that would be infeasible as a solution. We also believe that a careful analysis of the second derivative will also show that our code produces a global minimum, although we did not have time to investigate this.

The second important phenomenon that we noticed is that if one increases K and h simultaneously with ratio unchanged, then he will find that the optimal L^* is in fact the same (see Table 1 below). This observation lends itself to the hypothesis that L^* is actually an increasing function of $\frac{K}{h}$. If one considers enough plots of the value of $\frac{K}{h}$ versus L^* (see Figure 1 below), he will see as we did that there tends to be some sort of power function (with power coefficient less than 1) relationship between the two. If this is in fact the case, then we would expect the equation

$$\log L^* = A \log \frac{K}{h} + B \tag{2.12}$$

to be a linear relationship between $\log L^*$ and $\log \frac{K}{h}$. (Note that A and B in this equation are functions of μ, σ, and x). We ran several simulations to try and provide some empirical evidence of our hypothesis, and in so doing, computed the corresponding regression lines and found promising results. Our correlation coefficient (R^2) in most instances was above 0.95 and was always above 0.90. This would tend to suggest statistically that there indeed is a strong linear relationship between $\log L^*$ and $\log \frac{K}{h}$. (See Table 2 below.) We find this result favorable for another reason besides statistics however: if indeed equation (12) holds, then of course we can write this equation equivalently as

$$L^* = \left(\frac{K}{h}\right)^A e^B \tag{2.13}$$

simply by raising both sides of equation (12) to the e power. This is favorable because it resembles the results obtained earlier in the standardized and $\mu = 0$ cases. Thus, it appears that there may not be significant differences in the three previously mentioned cases after all. We also began investigating the relationship of L^* with the parameters μ and σ. Examples of findings for these parameters are given in Tables 3 and 4, and Table 5 summarizes our findings in the generalized Brownian Motion case. The numerical results demonstrates that the behavior changes at some point (call it μ^*): for μ smaller than this value, an increase in μ corresponds to a decrease in L^*, while for $\mu^* > \mu$, an increase in μ corresponds to an increase in L^*.

2.4.2 Geometric Brownian Motion

Note that in this case, our parameter estimates have changed drastically because $x \neq 0, \mu(x) = x(\mu + \frac{1}{2}\sigma^2), \sigma(x) = x^2\sigma$, where μ and σ are the corresponding estimates under the generalized model. Our ODEs in this case are now nonhomogeneous linear equations with polynomial coefficients. While we did not have sufficient time to fully investigate this case, we did do some preliminary investigation of the model and found that many of the ideas from the generalized case carry over to the geometric model, and so early evidence tends to suggest that there may not be much difference between the two cases. As we have treated the results thoroughly for the generalized case, we will not repeat them here.

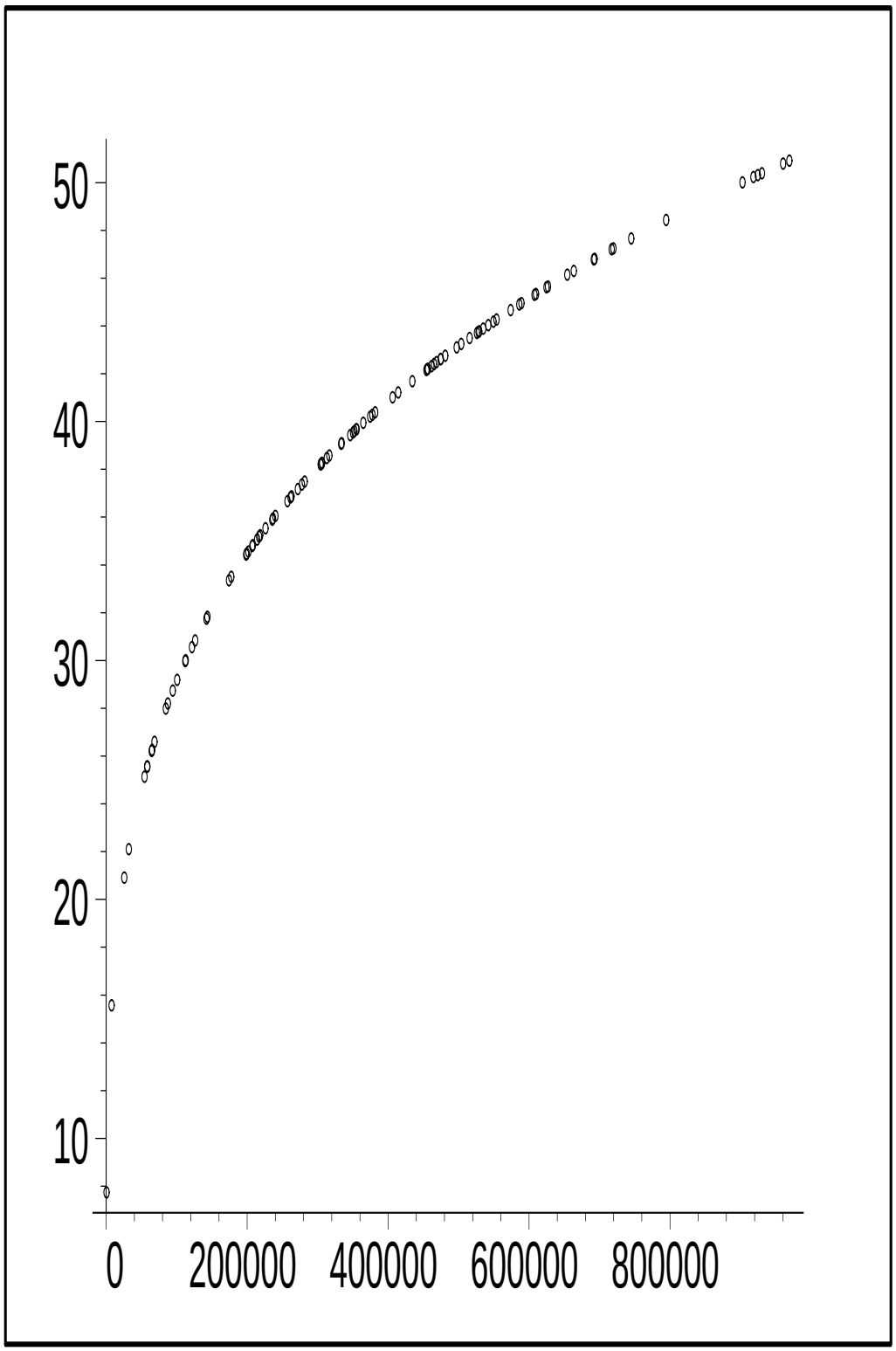

Figure 2.1: The relationship between $\frac{K}{h}$ and L^* appears to be logarithmic. (Here, $\frac{K}{h}$ is on the horizontal axis and L^* is on the vertical axis.)

K	h	L^*
19700	197	1.903455234
413700	4137	1.903455234
197000	1970	1.903455234
265950	2659.5	1.903455234

Table 2.1: If $\frac{K}{h}$ is fixed, L^* is unchanged. (In this simulation, $\mu = .028221, \sigma = .154954$ and the initial price x is zero.)

Contract	μ	σ	Actual L^*	A	B	Predicted L^*	R^2
Cattle	.028221	.154954	3.004	.3291	-.9921	2.868	.99
Gold	.135353	.554541	5.409	.3269	-.4360	4.933	.99
Index	-.044785	1.1473	7.908	.2450	.5503	7.948	.99

Table 2.2: Examples of the model. (Note that μ and σ are taken from real-world data). For computations, $x = 0, K = 1000, c = 2$, and 100 iterations were done by letting K and h vary randomly to compute the regression line.

σ	L^*
0.015	2.768158394
0.15	2.987514803
0.30	3.938394970
0.50	5.180948510
0.70	6.167192139

Table 2.3: The apparent relationship between L^* and σ. (In this simulation, $\mu = .0282221, h = 2$ and $K = 1000$.)

μ	L^*
0.005	2.879328074
0.011	2.823754436
0.0135	2.815847811
0.014	2.815831369
0.023	2.902194209
0.039	3.242709116

Table 2.4: The apparent relationship between L^* and μ. Note that there is a change in the behavior at some point μ^*. The group calculated μ^* to be $\mu = 0.0137$ in this case. (The other parameters and their corresponding values are: $x = 0, \sigma = .154594, h = 2, K = 1000$.)

Variable of Increase	Does L^* increase or decrease?
K	Increases
h	Decreases
μ	Increases for $\mu > \mu^*$
σ	Increases

Table 2.5: If K and h are increased by the same amount L^* is unchanged. (In this simulation, $\mu = .028221, \sigma = .154954$ and the initial price x is zero.)

2.5 Future Work

The group set forth many ideas for future analysis of this model. First, we were not able to examine the geometric Brownian motion model in depth, and so more confirmation of our preliminary results showing striking similarities to the generalized Brownian motion is needed. Second, another model that needs to be considered is the Ornstein-Uhlenbeck process, which assumes that the futures price is proportional to the current price. Thirdly, following the model given by Ackert and Hunter [A-H], we have assumed that our price limits our symmetric with respect to the starting price. This assumption clearly simplified the model greatly, but of course, there is no reason to believe that setting the limits in this fashion is optimal. (Although realistically, this is the manner in which it is currently done is due to considerations of practicality.) Fourth, our model is mono-cyclic: an extension to multi-cyclic versions seems necessary. Fifth, we were unable in such a short amount of time to determine closed forms for A and B in terms of x, μ, and σ. This particular fact is probably most important of all the ideas for future work as knowing the closed form could give considerable insight as to how the system is working as a whole. Finally, the authors argue that using constant limits over time may not be the best approach to setting the limits optimally. Indeed, during the last month of the contract, prices follow anything but the constant model. This being the case, we propose considering models where the limits are instead piecewise-linear or exponential, or some other form of non-constant functions over time.

Bibliography

[A-H] Ackert, L. and Hunter, W. (1994), Rational Limits in Futures Markets: Test of a Sample Optimizing Model. *Review of Financial Economics*, Vol. 4, No. 1, 93-108.

[K-T] Karlin, S. and Taylor, H. (1981), *A Second Course in Stochastic Processes*. Academic Press, New York.

Chapter 3

Modeling the Conductivity of Concrete

Sarah Grove[1], Yujun Huang[2], Dongming Jiang[3], Ilya Lavrik[4], Adnan Sabuwala[5], Joseph Twagilimana[6]

Problem Presenter:
Alan F. Karr
National Institute of Statistical Sciences

Faculty Consultants:
Mansoor Haider, North Carolina State University
Zhilin Li, North Carolina State University

Abstract

Concrete, one of the most common building materials, is highly vulnerable to deterioration. A principal mechanism is for water to permeate the concrete and then freeze, cracking concrete and creating new paths for permeation. In addition, chloride permeability — permeation of water containing dissolved salts (used to de-ice roads) can cause reinforcing bars to rust, which also lead to cracking. Permeability of concrete is both difficult and time consuming to study in the laboratory (some tests take months). This project focussed on conductivity, which has a strong physical analogy to permeability, but is easier to measure and model. In the current project we first developed a model for concrete and based on the Einstein correspondence between diffusivity and random walks, we used Brownian motion to estimate the conductivity of concrete.

3.1 Introduction and Motivation

In its simplest form, concrete is a mixture of paste and aggregates. The paste, composed of Portland cement and water, coats the surface of the fine and coarse aggregates. Through a chemical reaction called hydration, the paste hardens and gains strength to form the rock-like mass known as concrete. The key to achieving a strong, durable concrete rests in the careful proportioning and mixing of the ingredients. A concrete mixture that does not have enough paste to fill all the voids between aggregates will be difficult to place and will produce rough, honeycombed surfaces and porous concrete. A mixture with an excess of cement paste will be easy to place and will produce a smooth surface; however, the resulting concrete is likely to shrink more

[1]slgrove@ncsu.edu, North Carolina State University
[2]huang@math.gatech.edu, Georgia Institute of Technology
[3]jiangd@email.uc.edu, University of Cincinnati
[4]ilavrik@isye.gatech.edu, Georgia Institute of Technology
[5]sabuwala@math.ufl.edu, University of Florida
[6]jtwagira@louisville.edu, University of Louisville

and be uneconomical. A properly designed concrete mixture will produce the desired workability for the fresh concrete and the required durability and strength for the harder concrete. Typically, a mix is about $10-15\%$ cement, $60-75\%$ aggregate and $15-20\%$ water. Through a chemical reaction called 'hydration', the paste hardens and gains strength. The character of concrete is determined by the quality of the paste. The strength of the paste, in turn, depends on the ratio of water to cement.

Aggregates are inert granular materials such as sand, gravel, or crushed stone that, along with water and Portland cement, are an essential ingredient in concrete. Aggregates, which account for $60-75\%$ of the total volume of concrete, are divided into two distinct categories — fine and coarse. Fine aggregates generally consist of natural sand or crushed stone with most particles passing through $\frac{3}{8}$ inch sieve. Coarse aggregates are any particle greater than 0.19 inch but generally range between $\frac{3}{8}$ and 1.5 inches in diameter.

With a few simplifying assumptions, we develop a model for concrete. There are two main steps in our approach. The first step is to generate spherical aggregates with random sizes and locations but with a fixed volume fraction to mimic the structure of concrete. Once we have a geometric representation of a sample of concrete, the second step is to use the method described in [4] to estimate the conductivity. In this method, we need to solve a Laplace equation in the interior of concrete but outside of the aggregates with some mixed Dirichlet and Neumann boundary conditions. Using the samples generated by the model, we use two different approaches to solve the problem — partial differential equation (PDE) approach, which we describe in Section 3.2 and the Brownian motion approach, which can be found in Section 3.3. The simulation results are outlined in Section 3.4. Finally, conclusions and future work toward refinement are described in Section 3.5.

3.2 PDE Approach

To approximate the conductivity, we can solve the partial differential equation

$$\begin{aligned} u_{xx}+u_{yy} &= 0, \qquad (x,y)\in\Omega-\Omega_a && (3.1)\\ u(x,0) &= 0, && (3.2)\\ u(x,c) &= 1 && (3.3)\\ \frac{\partial u}{\partial n}(0,y) &= \frac{\partial u}{\partial n}(b,y)=0, && (3.4)\\ \frac{\partial u}{\partial n}(x,y) &= 0, \qquad (x,y)\in\cup\partial R_i, && (3.5) \end{aligned}$$

where we assume that Ω is a rectangular domain, $\Omega_a=\cup R_i$, the union of all aggregates, ∂R_i is the boundary of the i^{th} aggregate. In other words, we need to solve the Laplace's equation within the two or three dimensional boundaries, but outside of all inclusions. The 2D boundary is a rectangle with $c=1$ and $b=2$ while the 3D boundary is a cylinder with radius 1 and height 2. See Figure 3.1 for an illustration.

The conductivity can be approximated by

$$c=\frac{1}{\epsilon}\int_0^1 u(x,\epsilon)dx \tag{3.6}$$

In applied mathematics, it has been a challenge to solve problems numerically to a certain accuracy. There are a variety of methods in the literature that can be used to solve this problem. This is where statistician and applied mathematician can work together. More importantly, this gives an alternative approach to validate our analysis and results since no analytic solution is available.

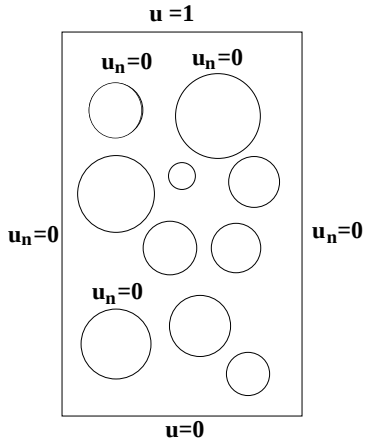

Figure 3.1: A diagram of the geometry and boundary conditions for the PDE.

First, we need to represent the aggregates efficiently. This can be done using the level set method. We can generate a uniform Cartesian grid

$$x_i = ih_x, \quad i = 0, 1, \cdots, m, \quad h_x = \frac{1}{m}, \tag{3.7}$$

$$y_j = jh_y, \quad j = 0, 1, \cdots, n, \quad h_y = \frac{b-c}{n}. \tag{3.8}$$

Then, the boundary of all aggregates can be expressed as the zero level set function $\varphi(x, y) = 0$:

$$\varphi(x, y) = \min\{\varphi_1(x, y), \varphi_2(x, y), \cdots, \varphi_i(x, y), \} \tag{3.9}$$

where

$$\varphi_i(x, y) = \sqrt{(x - x_i)^2 + (y - y_j)^2} - r_i. \tag{3.10}$$

For a general complicated domain, $\varphi(x, y)$ is the distance function to the boundary of all aggregates $\Omega_a = \cup \partial R_i$.

To solve the PDE, we use the fast immersed interface method (IIM, Z. Li [1, 2]) applied to Poisson equations on irregular domains. The computer code is available to the public at ftp.ncsu.edu under the directory /pub/math/zhilin/Packages/Helmholtz_EXTERIOR and can be directly applied to our problem without any modification.

The main idea of the fast solver is based on the fictitious domain method. We extend the PDE to the entire rectangular domain so that a fast Poisson solver based on FFT can be applied. At the grid points near or on the boundary of aggregates, some correction terms C_{ij} are added to the finite difference equations

$$\frac{U_{i-1,j} - 2U_{i,j} + U_{i+1,j}}{h_x^2} + \frac{U_{i,j-1} - 2U_{i,j} + U_{i,j+1}}{h_y^2} = C_{ij}. \tag{3.11}$$

Figure 3.2 shows the plot of the conductivity versus the volume. The results were not as conclusive as we had originally hoped. We then realized that the computer resolution may not have been fine enough to obtain accurate results. Our samples of concrete had aggregates with as little as 10^{-16} space between them.

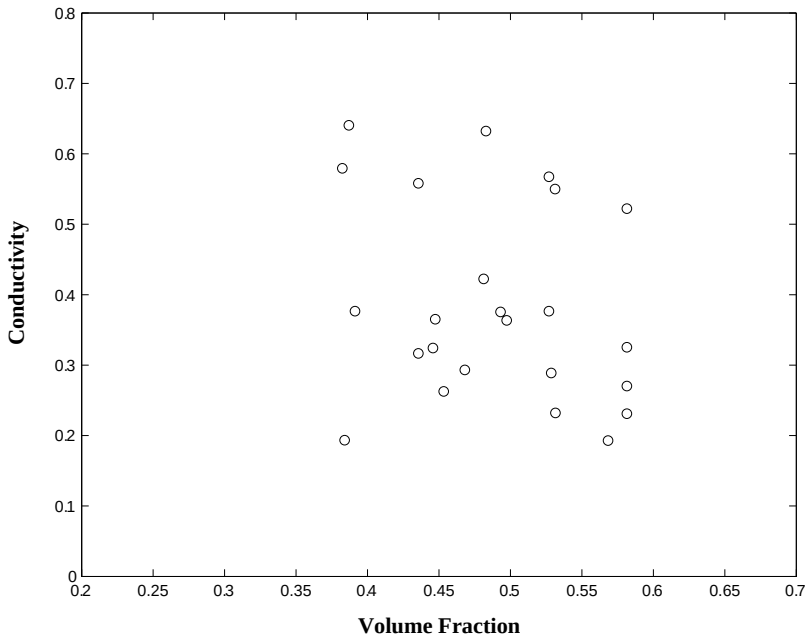

Figure 3.2: Plot of conductivity versus volume of aggregates. The computation was done using the IIM and the level set function without modification.

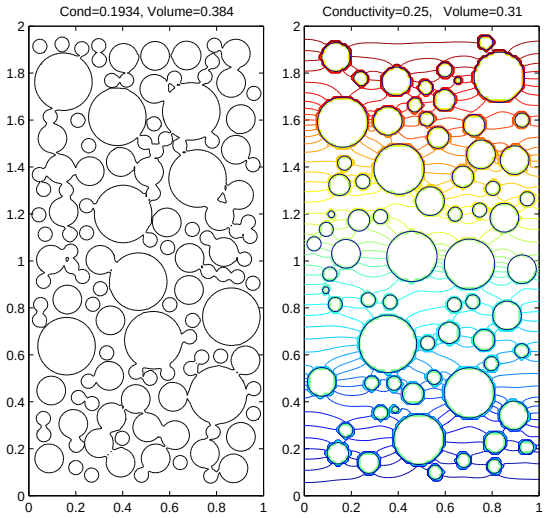

Figure 3.3: The geometry and contour plot of the potential. (a) The geometry represented by a level set function without modification. (b) The geometry and the contour plot of the potential with modified geometry on a different sample.

It is possible to increase the resolution and perform the computation on a super-computer. However, we have tried a simpler approach. We modify the geometry so that there are at least three grid points between two aggregates. Let $\mathbf{x}_i$ and $\mathbf{x}_j$ be two aggregates with radii r_i and r_j respectively. If $||\mathbf{x}_i - \mathbf{x}_j| - (r_i + r_j)| \leq \epsilon$ and $r_i \geq r_j$, then we set $r_i := r_i - C\epsilon$. C is a grid dependent constant with $C \sim 3h$. In figure 3.3, we show the original geometry and the modified geometry and the computed contour plot of the potential. In figure 3.4, we show the result using this approach. It is clear that the conductivity decreases as volume of aggregates increases.

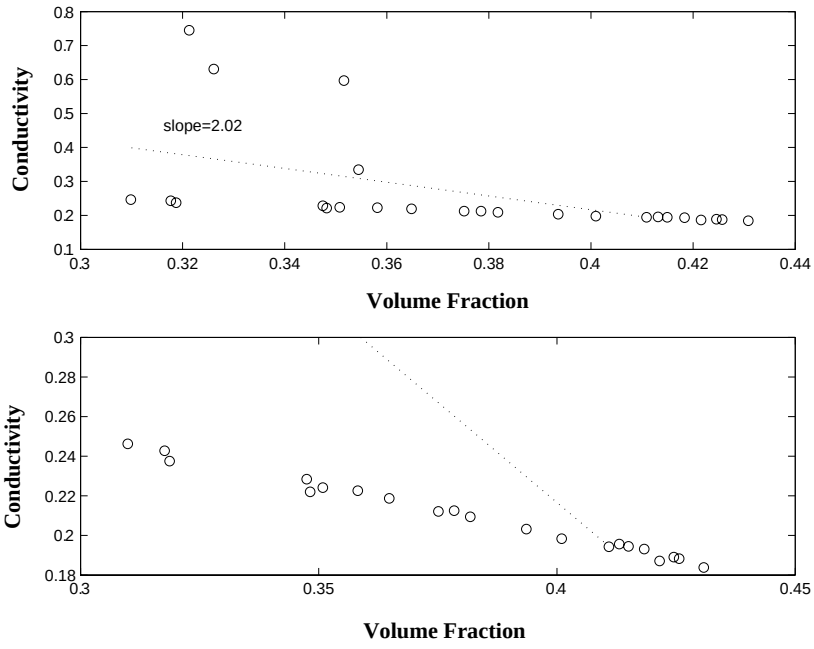

Figure 3.4: Plot of conductivity versus volume of aggregates. The geometry has been modified to guarantee the accuracy. We can see that the conductivity decreases as the volume increases. The bottom plot is a zoomed in plot of the top graph.

The simulations were performed on Sun Ultra workstations and Linux clusters. It took less than a couple of minutes for almost all the simulations. It seems to us that the conductivity may be affected by the locations of aggregates near the bottom using this PDE approach. This PDE approach works well if the aggregates are well separated. If some aggregates are too close together, it is worthwhile to investigate new fast solvers for the PDE. A $O(N)$ fast solver has been developed in [3] for chemical infiltration problems in 2D and 3D with Dirichlet boundary conditions. We hope similar methods can be developed for this problem when the aggregates are clustered together.

3.3 Brownian motion approach

In this section, we describe a method based on random walks for estimating the DC conductance of concrete. This method is particularly useful for composite materials consisting of a bulk conducting phase, the cement paste in our case, and inclusions (aggregates) of lower or no conductivity.

To develop the theory and method behind this approach, we shall assume a rectangular boundary in 2D with a width of 1 and a height of 2. The boundary is divided into four parts: two vertical walls, which are assumed to be insulated, and two conducting sides, one at the top through which the current enters, and one at the bottom through which the current leaves, as shown in Figure 3.5.

The top plate is assumed to be at a potential $\phi = 1$ while the bottom plate is at a potential $\phi = 0$. We use a simplified model of concrete composed of only two phases: the conducting (permeable) homogenous mortar, and the insulating (impermeable) aggregate. We further assume that the aggregates are of the coarse type only and that they are circular in shape. The aggregates are distributed randomly inside the rectangular boundary given a specified aggregate size distribution and a target volume fraction (VF^*). The aggregates do not overlap or cross the rectangular boundary walls. Based on the specified aggregate size distribution and target volume fraction, several samples of concrete were generated. Figure 3.6 shows a 2D sample of concrete with VF^*=0.6.

The flow of DC current through the sample is determined by a potential ϕ which satisfies the following PDE problem:

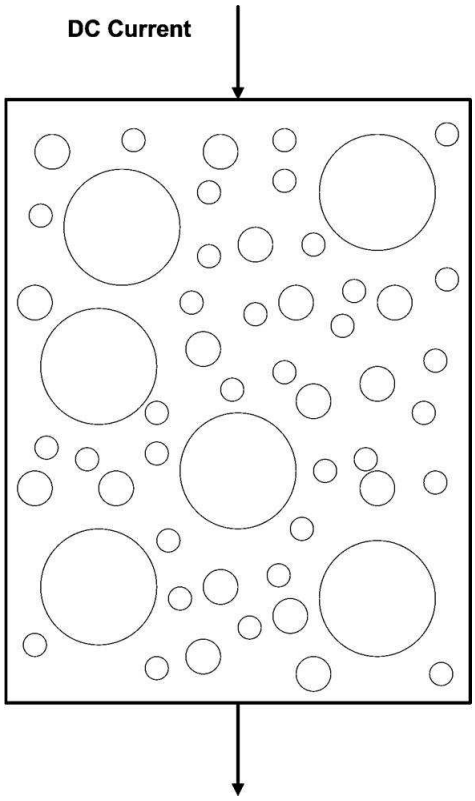

Figure 3.5: 2D Rectangular boundary model.

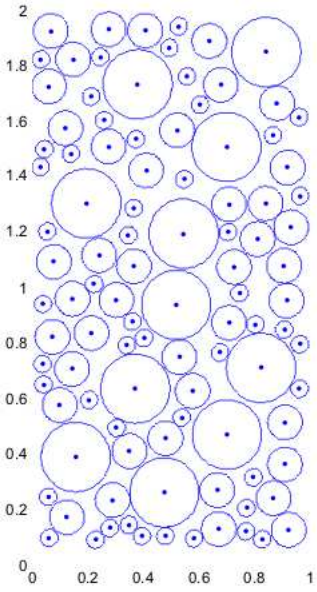

Figure 3.6: Sample of concrete generated for the 2D case with VF*=0.6.

$$\nabla \cdot [\sigma \nabla \phi] = 0 \tag{3.12}$$

where σ is an L^∞ function and the boundary conditions are

$$\phi = 1 \qquad \text{on the top plate} \tag{3.13}$$

$$\phi = 0 \qquad \text{on the bottom plate} \tag{3.14}$$

$$\frac{\partial \phi}{\partial n} = 0 \qquad \text{on the insulated walls} \tag{3.15}$$

$$\sigma \frac{\partial \phi}{\partial n} \text{ is } C^1 \text{ on the boundary of the aggregates} \tag{3.16}$$

where n is a normal vector to the insulated walls or the aggregate boundaries. Since (3.12) is an elliptic PDE with an L^∞ coefficient and since the boundary conditions are Lipschitz, there exists a unique solution ϕ to the equation. It should be noted that the above problem can easily be extended to the 3D case for specimens having arbitrary shapes and locations but reasonable boundaries (smooth). For our problem, however, we extend the 2D problem to a 3D problem under the assumptions of spherical aggregates and a cylindrical boundary with radius 0.5 and height 2. In general, it is not easy to represent the solution to the above problem in terms of power series or elementary functions. However, it is easy to estimate the value of ϕ at any point using the approach of random walks.

The conductance of a sample can be estimated from the solution $\phi(x, y)$ of the above problem using a one-term Taylor series expansion. Assume that there are no aggregates on or below the line $y = \epsilon$. The conductance is then given by the leading term in the following equation:

$$\int_0^1 \frac{\partial \phi}{\partial y}(x, 0)dx = \frac{1}{\epsilon}\varphi - \frac{\epsilon}{2}R \tag{3.17}$$

where

$$\varphi = \int_0^1 \phi(x, \epsilon)dx \tag{3.18}$$

and

$$R = \int_0^1 \frac{\partial^2 \phi}{\partial y^2}(x, \xi_i(x))dx \tag{3.19}$$

If R is similar in magnitude, the size of the remainder term will be dominated by ϵ. In our case, ϵ is chosen small enough to safely neglect the remainder term in the estimation of the conductance. Thus, the problem of estimating the conductance now reduces to one of finding the potential ϕ and then computing the integral (3.18).

Random walks are used in approximating the elliptic boundary value problem stated in the beginning of this section. With the potential fixed at $\phi = 1$ on the top plate and $\phi = 0$ at the bottom plate, we can estimate the potential at any point $\phi(x, y)$ as the following probability:

$$\phi(x, y) = \Pr[\text{Brownian motion beginning at } (x, y) \text{ crosses the top plate before crossing the bottom plate}] \tag{3.20}$$

This allows the estimation of ϕ at individual points, unlike the finite element method which requires estimating ϕ over the entire rectangular boundary. We approximate Brownian motion by random walks of fixed step length (denoted by S). A uniformly distributed random point on the line y=ϵ is first generated as a starting point of our Brownian motion (random walk).

- Generate starting point.

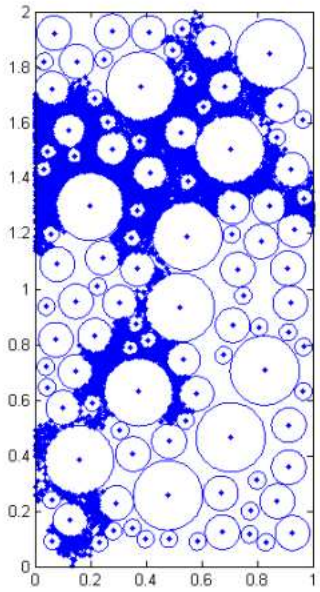

Figure 3.7: Top Exit

- Take a step by generating a point which is uniformly distributed over the boundary of a circle with center as our previous point and radius equal to S.
- If exited
  - If top exit: Top exits = Top exits +1.
- Else generate another point
- If point is outside boundary walls or inside an aggregate: Reflect point using Snell's Law of reflection. (Note: Total distance traveled must equal the step size of random walk.)
- Return to first step and repeat until total number of exits equals some given number of trials.

Once the potential has been estimated by the above probability relation, our next goal then becomes the computation of the integral in estimating the conductance. If each choice of starting point and subsequent direction are mutually independent, then the conductance is estimated as an average estimate of the potential at a uniformly distributed random point on the line y=ϵ. We run lots of Brownian motions and estimate the conductance as the proportion of top exits. Results for the 2D and 3D cases with the Brownian motion approach are presented in the next section. Mathematical details about computation of the reflection point co-ordinates given the starting point and the final point (which obviously lies either outside the walls or inside an aggregate) are omitted as it is not too hard to compute the exit points.

3.4 Results

3.4.1 2D Results

For the 2D Brownian motion case, we created five data sets for each of three volume fractions, 0.4, 0.5, and 0.6. For each data set, we ran 10,000 Brownian motions and computed the overall conductance as the proportion of top exits. Figure 3.7 shows an exit from the top plate for this case while Figure 3.8 shows an exit from the bottom plate. We then performed the same trials on inverted versions of the 2D samples generated to verify

Figure 3.8: (a)Exit from the bottom plate. (b)Same plot zoomed to show the joined steps taking during the simulation.

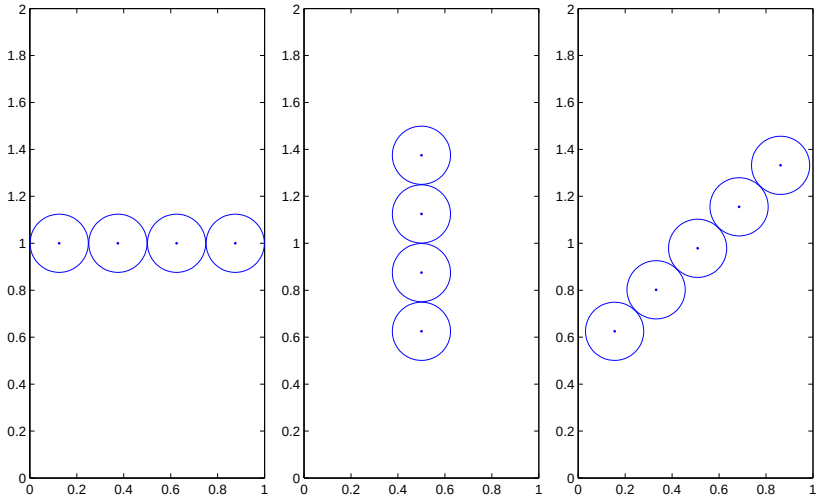

Figure 3.9: Effect of Geometry on Conductivity

that inverting the same configurations made no difference in the conductivity. The trend in conductivity was observed to be dependent on volume fraction. This is detailed later in this section. It should be noted though, that in the current project we have made the simplifying assumptions of the presence of only coarse aggregates and have further assumed their shapes to be circular in 2D and spherical in 3D.

We also created three data sets for a fixed volume fraction with different alignments (horizontal, vertical, and diagonal) to check whether geometrical positioning made any difference in the conductivities. These contrived data sets were created with space in between each of the aggregates as well as the boundary. If one were to zoom in on the diagrams one would observe this. As expected, we found that geometry does affect conductivity with the horizontal alignment having the least conductivity and the vertical alignment having the maximum conductivity. These contrived samples are illustrated in Figure 3.9.

3.4.2 3D Results

For the 3D case, we created five samples of concrete each for volume fractions of 0.25, 0.3, 0.35, and 0.4. One such sample is shown in Figure 3.10.

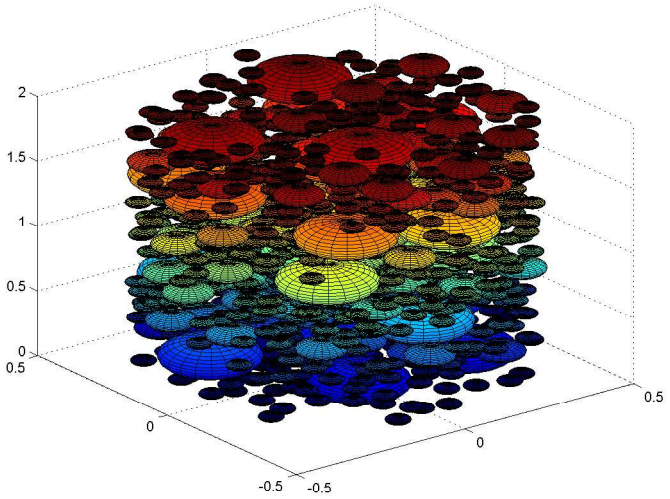

Figure 3.10: Sample of concrete generated for the 3D case with VF*=0.25

On each of these 20 samples, we ran 1,000 Brownian motions to estimate the conductivity as the proportion of top exits. Figure 3.11 shows a typical Brownian motion path (in yellow) through a sample of concrete. Also shown in Figure 3.11 is a zoomed in view of the Brownian motion. It was beneficial to view the reflections off the boundary as well as the aggregates. In running the Brownian motion we were forced to use a slightly larger step size to reduce the convergence time. Typically though, a step size of about 0.01 times the diameter of the smallest aggregate would be a good choice. Thus we were concerned about the possibility of a step to jump over the smallest aggregates. However this occurrence's probability was low enough that it did not effect the outcome overall.

The trend in conductivity of concrete with volume fraction using the Brownian motion approach is shown in Figure 3.12. From the graphs it is clear that the conductivity decreases as the number of aggregates (correspondingly, their volume fraction) inside the cement paste increases. The lines shown in the figure join the sample mean of the data.

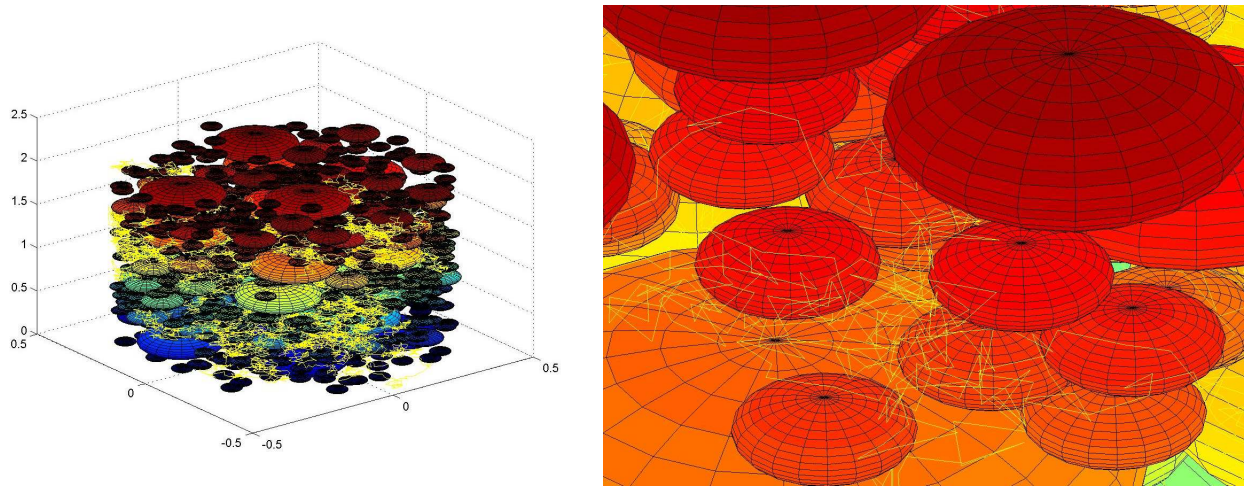

Figure 3.11: (a)Brownian motion path through 3D sample. (b)Same plot zoomed to show the joined steps taking during the simulation.

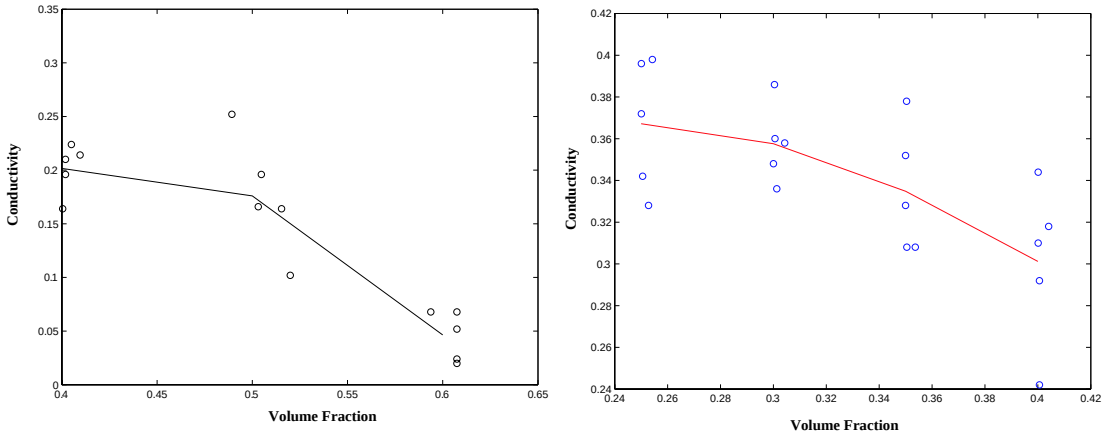

Figure 3.12: Conductivity vs. VF* (a) 2D Case. (b) 3D Case.

3.5 Conclusions and Future Work

The most important conclusion from the current project is that conductivity depends upon the volume fraction of aggregates almost linearly. It decreases linearly with increase in the volume fraction. Also, as seen in Section 3.4 conductivity is affected by possibly many other factors, one of which (geometry) was investigated in this project. The results clearly indicate that geometrical alignment of the coarse aggregates greatly influences the conductivity of concrete. Several of the simplifying assumptions made can be generalized to obtain more accurate results. 3D models which incorporate the effects of pouring, settling of aggregates, presence of sand and other fine aggregates in addition to coarse aggregates, and assuming the aggregates have arbitrary shapes can be investigated in the future to get a more accurate representation of conductivity. We also need to reduce the step size of the Brownian motion random walks to ensure greater accuracy. Finally, the relationship between conductivity and geometry must be investigated in further detail. These modifications will help in estimating the precise functional relationship between conductivity and volume fraction of aggregates.

Bibliography

[1] Z. Li. A fast iterative algorithm for elliptic interface problems. *SIAM J. Numer. Anal.*, 35:230–254, 1998.

[2] Z. Li, H. Zhao, and H. Gao. A numerical study of electro-migration voiding by evolving level set functions on a fixed cartesian grid. *J. Comput. Phys.*, 152:281–304, 1999.

[3] S. Jin, X.L. Wang, T.L. Starr, and X.F. Chen. Robust Numerical Simulation of Porosity Evolution in Chemical Vapor Infiltration I: Two Space Dimension. *J. Comput. Phys.*, 162:467-482, 2000.

[4] J.D. Picka, and K. Chermakani Random-Walk-Based Estimates of Transport Properties in Small Specimens of Composite Materials. , 2001.

[5] Portland Cement Associatic Concrete Basics, http://portcement.org

Chapter 4

Evaluating a Physiologically Based Pharmacokinetic Model Proposed for use in Environmental Risk Assessment

Jimena Davis[1], John Fricks[2], Joyce Macabea[3], Lara Stroud[1], Gentry White[4], Andrea Wong[5]

Problem Presenters:

Hugh Barton
Woodrow Setzer

Environmental Protection Agency

Abstract

Physiologically Based Pharmacokinetic (PBPK) models are compartmental models that describe the uptake, distribution, and elimination of a substance as it travels through the body. They can be used to predict parent chemical or metabolite concentrations in tissues and organs, given an exposure level and route. A PBPK model for isopropanol (IPA) and its metabolite, acetone, has been proposed by Clewell et al.(2001). The Environmental Protection Agency (EPA) would like to evaluate the model appropriateness and adequacy for dose-response assessment.

The PBPK model is composed of twenty-nine coupled differential equations with over fifty parameters. The parameters of the PBPK model include physiological, uptake/clearance, tissue distribution, and metabolic parameters. Because of the model complexity, there exists uncertainty as to correctness of the model. The uncertainty in the model outputs arises (1) from variability of the measured concentration of the chemical in the blood/tissue and (2) from the estimates of the parameters.

It is desirable to determine which parameters most strongly effect the PBPK predictions. This paper presents a sensitivity analysis to determine how the output of the model fluctuates with respect to individual parameters over time, as well as a sensitivity metric to determine how the simultaneous variance of multiple parameters affects the output of the model.

Introduction

The Environmental Protection Agency is charged with setting acceptable exposure levels for various environmental agents including toxic or potentially hazardous chemicals. Toxicity and tissue concentration can be

[1]North Carolina State University
[2]University of North Carolina-Chapel Hill
[3]Boston University
[4]University of Missouri-Columbia
[5]University of North Carolina-Greensboro

determined experimentally in animals, with the desire to see the data extrapolated to humans. In addition to animal experiments, experiments can be conducted on the effects of low-level exposure in humans. The cost of these experiments can be prohibitive in terms of both time and money. With this as a motivating factor, a mathematical model was developed to simulate the response of an organism's system to exposure to chemical agents through a variety of uptake pathways. The particular model presented in this paper was developed to simulate the effects of exposure to isopropanol(IPA) and its metabolite acetone. In order to evaluate the model, a method based on sensitivity analysis is used to estimate the dependence on the parameter estimates and subsequently, the response estimates produced by the model.

The use of physiologically based pharmacokinetic (PBPK) models for correlating tissue concentrations with toxicity is of interest due to the expense and time involved in performing experiments. The complexity of biological systems and the unavailability of data with which to evaluate these models makes traditional methods of statistical analysis of model parsimony or goodness-of-fit inaccessible to biologists. Traditional experiments have sought to simulate the biological systems' behavior in terms of chemical concentration in specific tissues with respect to time for individual intake methods. This results in a model consisting of a series of ordinary differential equations describing the chemical concentration with respect to time in a given tissue.

Previously, each of the PBPK models for different exposure routes of IPA, acetone or both has been developed and fitted based on minimal experimental data. In the model presented in this paper, we sought to combine these models in order to have a single model capable of simulating the effects of several different uptake methods. Additionally, the model was intended to fit data concerning chemical exposure in rats and then be scaled to predict responses in humans. In order to fit this model, several different datasets from experiments spanning over 50 years were utilized. Most of the results were unavailable in raw form and consisted of the means of results for experiments. In addition, physiological parameter estimates were taken from the literature; however, no direct information on the variability of the estimates was available in the datasets provided. As a result, there exists some question as to the quality of the model, in particular the goodness-of-fit, the error structure, and the variability of the parameter estimates. Because the model seeks to fit continuous time series data and because of the statistical complexity of the model, the error structure along with the variability in the parameter estimates is not easily accessible. As a result, methods based on sensitivity analysis and simulation studies are developed to observe the consequences for outputs of parameter variation.

The first section of this paper will address the form of the model presented in the workshop and the state-variable equations used to describe the system. The next two sections will describe the methods of sensitivity analysis conducted and will then discuss results. In the final sections, ideas for future consideration are discussed.

4.1 Description of the PBPK Model for Isopropanol and Acetone

Clewell et al. (2001) have developed a PBPK model for isopropanol and its metabolite acetone for both rats and humans. The model was developed from previous models of both isopropanol and acetone. The model can be translated to a system of ordinary differential equations (ODE) describing mass flow rates through various compartments, i.e., tissues and organs.

4.1.1 Model Structure

The diagram for the compartmental PBPK model is given in Figure 4.1. Both the parent chemical, isopropanol, and the metabolite, acetone, are represented in the model. Abbreviations for the compartments are given in Table 4.1.

The model describes absorption, distribution, metabolism, and elimination of the parent chemical and its metabolite. There are multiple routes of exposure, including: oral gavage, dermal application, inhalation, intraperitoneal injection, and intravenous injection. The parent chemical, isopropanol, can be distributed to the various compartments via the circulatory system or metabolized in the liver to its metabolite, acetone.

Elimination as either isopropanol or acetone occurs via urine, feces, or exhaled air. Acetone can also leave the system via further metabolism to other metabolites.

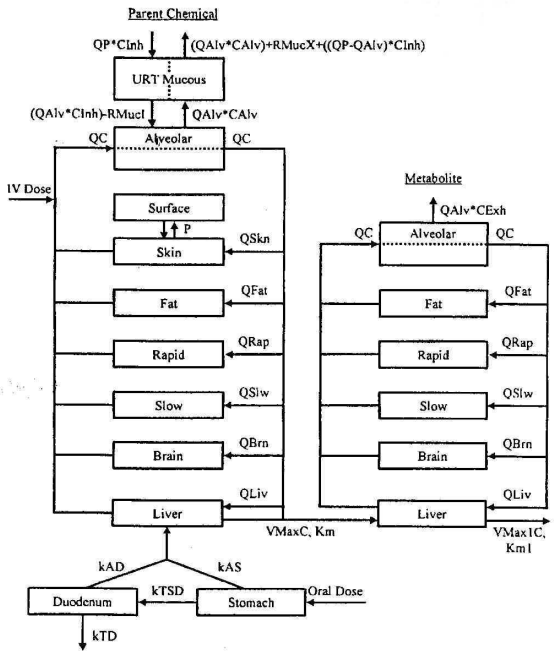

Figure 4.1: PBPK Model for Isopropanol and Acetone

4.1.2 Model Derivation

The ODE model consists of twenty-nine differential equations with more than 50 parameters that describe the change in amount or concentration of either isopropanol or acetone in each of the compartments as given below (Table 4.1). For the system of equations, movement into and out of the most basic flow-limited compartments can be described by the following equations,

$$\frac{dA}{dt} = V * \frac{dC}{dt} = Q * (C_{in} - C_{out})$$

where V is the volume of the compartment, C is the concentration of isopropanol or acetone in the compartment, A is the amount of isopropanol or acetone in the compartment, Q is the blood flow rate to the tissue, and C_{in} and C_{out} are the concentrations entering and exiting the compartment from the arterial blood to the venous blood, respectively.

Compartment	**Isopropanol**	**Acetone**
Mucous	Muc	–
Alveolar	Alv	Alv1
Surface	Sfc	–
Skin	Skn	–
Fat	Fat	Fat1
Rapidly Diffused Tissue	Rap	Rap1
Slowly Diffused Tissue	Slw	Slw1
Brain	Brn	Brn1
Liver	Liv	Liv1
Duodenum	Du	–
Stomach	St	–

Table 4.1: Compartments in the PBPK Model for Isopropanol and Acetone

Equations for Isopropanol:

$\frac{dA_{Ch}}{dt} = [Rats * (\frac{Q_{Alv} * A_{Art}}{V_{Alv} * P_B} - \frac{Q_{Alv} * C_{IZone} * A_{Ch}}{V_{Ch}} + \frac{dA_{Muc_e}}{dt})] - (k_{LC} * A_{Ch})$

$\frac{dA_{Muc_i}}{dt} = k_{Urt} * (\frac{C_{IZone} * A_{Ch}}{V_{Ch}} - \frac{A_{Muc}}{V_{Muc} * P_{Muc}})$

$\frac{dA_{Muc_e}}{dt} = k_{Urt} * (\frac{A_{Muc}}{V_{Muc} * P_{Muc}} - \frac{A_{Art}}{V_{Alv} * P_B})$

$\frac{dA_{Muc}}{dt} = \frac{dA_{Muc_i}}{dt} - \frac{dA_{Muc_e}}{dt}$

$\frac{dA_{Art}}{dt} = -\frac{Q_{Alv} * A_{Art}}{V_{Alv} * P_B} + \frac{Q_{Alv} * C_{IZone} * A_{Ch}}{V_{Ch}} - \frac{dA_{Muc_i}}{dt} + [Q_C * (C_{Ven} - \frac{A_{Art}}{V_{Alv}})]$

$\frac{dA_{Exh}}{dt} = \frac{Q_{Alv} * A_{Art}}{V_{Alv} * P_B} + \frac{dA_{Muc_e}}{dt}$

$\frac{dA_{Brn}}{dt} = Q_{Brn} * (\frac{A_{Art}}{V_{Alv}} - (A_Brn/(V_Brn * P_Brn)))$

$\frac{dA_{O_{Abs}}}{dt} = (k_{AS} * (TotDose - A_{lSt})) + (k_{AD} * A_{Du})$

$\frac{dA_{Exc}}{dt} = k_{TD} * A_{Du}$

$\frac{dA_{Du}}{dt} = (k_{TSD} * (TotDose - A_{lSt})) - (k_{AD} * A_{Du}) - (k_{TD} * A_{Du})$

$\frac{dA_{lSt}}{dt} = (k_{AS} * (TotDose - A_{lSt})) + (k_{TSD} * (TotDose - A_{lSt}))$

$\frac{dA_{Fat}}{dt} = Q_{Fat} * (\frac{A_{Art}}{V_{Alv}} - \frac{A_{Fat}}{V_{Fat} * P_{Fat}})$

$\frac{dA_{Liv}}{dt} = [Q_{Liv} * (\frac{A_{Art}}{V_{Alv}} - \frac{A_{Liv}}{V_{Liv} * P_{Liv}})] + \frac{dA_{O_{Abs}}}{dt} - \frac{dA_{MetTot}}{dt}$

$\frac{dA_{Met1}}{dt} = \frac{V_{Max} * A_{Liv}}{(V_{Liv} * P_{Liv} * K_M) + A_{Liv}}$

$\frac{dA_{Met2}}{dt} = \frac{K_F * A_{Liv}}{P_{Liv}}$

$\frac{dA_{MetTot}}{dt} = \frac{dA_{Met1}}{dt} + \frac{dA_{Met2}}{dt}$

$\frac{dA_{Rap}}{dt} = Q_{Rap} * (\frac{A_{Art}}{V_{Alv}} - \frac{A_{Rap}}{V_{Rap} * P_{Rap}})$

$\frac{dA_{Sfc}}{dt} = \frac{P * Area}{1000} * (\frac{A_{Skn}}{V_{Skn} * P_{SknL}} - C_{SFC})$

$$\frac{dA_{Skn}}{dt} = [\frac{P*Area}{1000} * (C_{SFC} - \frac{A_{Skn}}{V_{Skn}*P_{SknL}})] + [Q_{Skn} * (\frac{A_{Art}}{V_{Alv}} - \frac{A_{Skn}}{V_{Skn}*P_{SknB}})]$$

$$\frac{dA_{Slw}}{dt} = Q_{Slw} * (\frac{A_{Art}}{V_{Alv}} - \frac{A_{Slw}}{V_{Slw}*P_{Slw}})$$

$$C_{Art} = \frac{A_{Art}}{V_{Alv}}$$

$$C_{Ven} = \frac{1}{QC} * [(\frac{Q_{Brn}*A_{Brn}}{V_{Brn}*P_{Brn}}) + (\frac{Q_{Fat}*A_{Fat}}{V_{Fat}*P_{Fat}}) + (\frac{Q_{Liv}*A_{Liv}}{V_{Liv}*P_{Liv}}) + (\frac{Q_{Rap}*A_{Rap}}{V_{Rap}*P_{Rap}}) + (\frac{Q_{Skn}*A_{Skn}}{V_{Skn}*P_{SknB}}) + (\frac{Q_{Slw}*A_{Slw}}{V_{Slw}*P_{Slw}}) + IV]$$

Equations for Acetone:

$$\frac{dA_{Exh1}}{dt} = \frac{Q_{Alv}*Q_C*C_{Ven1}}{Q_{Alv}+(P_{B1}*Q_C)}$$

$$\frac{dA_{Brn1}}{dt} = Q_{Brn} * [\frac{P_{B1}*Q_C*C_{Ven1}}{Q_{Alv}+(P_{B1}*Q_C)} - \frac{A_{Brn1}}{V_{Brn}*P_{Brn1}}]$$

$$\frac{dA_{Fat1}}{dt} = Q_{Fat} * [\frac{P_{B1}*Q_C*C_{Ven1}}{Q_{Alv}+(P_{B1}*Q_C)} - \frac{A_{Fat1}}{V_{Fat}*P_{Fat1}}]$$

$$\frac{dA_{Liv1}}{dt} = (Q_{Liv} * [\frac{P_{B1}*Q_C*C_{Ven1}}{Q_{Alv}+(P_{B1}*Q_C)} - \frac{A_{Liv1}}{V_{Liv}*P_{Liv1}}]) + (Stoch * \frac{dA_{MetTot}}{dt}) - (\frac{dA_{MetTot1}}{dt})$$

$$\frac{dA_{Met1A}}{dt} = \frac{V_{Max1}*A_{Liv1}}{(V_{Liv}*P_{Liv1}*K_{M1})+A_{Liv1}}$$

$$\frac{dA_{Met2A}}{dt} = \frac{K_{F1}*A_{Liv1}}{P_{Liv1}}$$

$$\frac{dA_{MetTot1}}{dt} = \frac{dA_{Met1A}}{dt} + \frac{dA_{Met2A}}{dt}$$

$$\frac{dA_{Rap1}}{dt} = Q_{Rap} * [\frac{P_{B1}*Q_C*C_{Ven1}}{Q_{Alv}+(P_{B1}*Q_C)} - \frac{A_{Rap1}}{V_{Rap}*P_{Rap1}}]$$

$$\frac{dA_{Slw1}}{dt} = (Q_{Slw} + Q_{Skn}) * [\frac{P_{B1}*Q_C*C_{Ven1}}{Q_{Alv}+(P_{B1}*Q_C)} - \frac{A_{Slw1}}{V_{Slw}*P_{Slw1}}]$$

$$C_{Art1} = \frac{P_{B1}*Q_C*C_{Ven1}}{Q_{Alv}+(P_{B1}*Q_C)}$$

$$C_{Ven1} = \frac{1}{Q_C} * [\frac{Q_{Brn}*A_{Brn1}}{V_{Brn}*P_{Brn1}} + \frac{Q_{Fat}*A_{Fat1}}{V_{Fat}*P_{Fat1}} + \frac{Q_{Liv}*A_{Liv1}}{V_{Liv}*P_{Liv1}} + \frac{Q_{Rap}*A_{Rap1}}{V_{Rap}*P_{Rap1}} + \frac{(Q_{Slw}+Q_{Skn})*A_{Slw1}}{V_{Slw}*P_{Slw1}}]$$

4.1.3 Model Parameters

In the original paper by Clewell et al. (2001), physiological parameters and partition coefficients were obtained from the available literature. The metabolic and absorption/excretion parameters were estimated by fitting available data to the model. Table 4.2 presents some of the parameters and the respective abbreviations used (*'s denote chemical specific parameters, with 1 representing acetone).

Parameter Type - Compartment	**Abbreviation**
Body Weight	BW
Cardiac Output	Q_C
Pulmonary Ventilation	Q_P
Blood Flow - Skin	Q_{Skn}
Blood Flow - Fat	Q_{Fat}
Blood Flow - Rapidly Perfused Tissue	Q_{Rap}
Blood Flow - Slowly Perfused Tissue	Q_{Slw}
Blood Flow - Brain	Q_{Brn}
Blood Flow - Liver	Q_{Liv}
Tissue Volume - Alveolar Blood	V_{Alv}
Tissue Volume - URT Mucous Layer	V_{Muc}
Tissue Volume - Fat	V_{Fat}
Tissue Volume - Rapidly Perfused Tissue	V_{Rap}
Tissue Volume - Slowly Perfused Tissue	V_{Slw}
Tissue Volume - Brain	V_{Brn}
Tissue Volume - Liver	V_{Liv}
Dead Space	Ds
Skin Depth	Depth
Absorption Coefficient - from Stomach to Duodenum	K_{AS}
Transfer Coefficient - from Stomach to Duodenum	K_{TSD}
Absorption Coefficient - from Duodenum	K_{AD}
Fecal Excretion Coefficient	K_{TD}
Urinary Clearance Coefficient	Cl_{UR}
Clearance Coefficient - into Upper Respiratory Tract	Cl_{Muc}
Partition Coefficient - Blood/Air	P_B, P_{B1} *
Partition Coefficient - Brain/Blood	P_{Brn}, P_{Brn1} *
Partition Coefficient - Fat/Blood	P_{Fat}, P_{Fat1} *
Partition Coefficient - Liver/Blood	P_{Liv}, P_{Liv1} *
Partition Coefficient - Saline/Air	P_{Lq} *
Partition Coefficient - Rapidly Perfused Tissue/Blood	P_{Rap}, P_{Rap1} *
Partition Coefficient - Slowly Perfused Tissue/Blood	P_{Slw}, P_{Slw1} *
Partition Coefficient - Mucous/Air	P_{Muc} *
Skin Permeability Coefficient	P
First Order Metabolic Rate Constant	K_{FC}, K_{FC1} *
Maximum Reaction Rate	V_{Max}, V_{Max1} *
Michaelis-Menten Constant	K_M, K_{M1} *

Table 4.2: Parameters in the PBPK Model for Isopropanol and Acetone

4.1.4 Model Simulation

The system of ODE's for our PBPK model of isopropanol and acetone was written in MATLAB© code. Simulations were then carried out using the model to predict amounts and concentrations of isopropanol and acetone in the body over time following different exposure methods. Results from a simulation via an oral dose of 1,250 mg/kg are presented in Figure 4.2. The results are shown for amounts and cumulative amounts for both isopropanol and acetone. Accumulated amounts level off to a constant after the chemical leaves the body whereas amounts in the body fall back to zero.

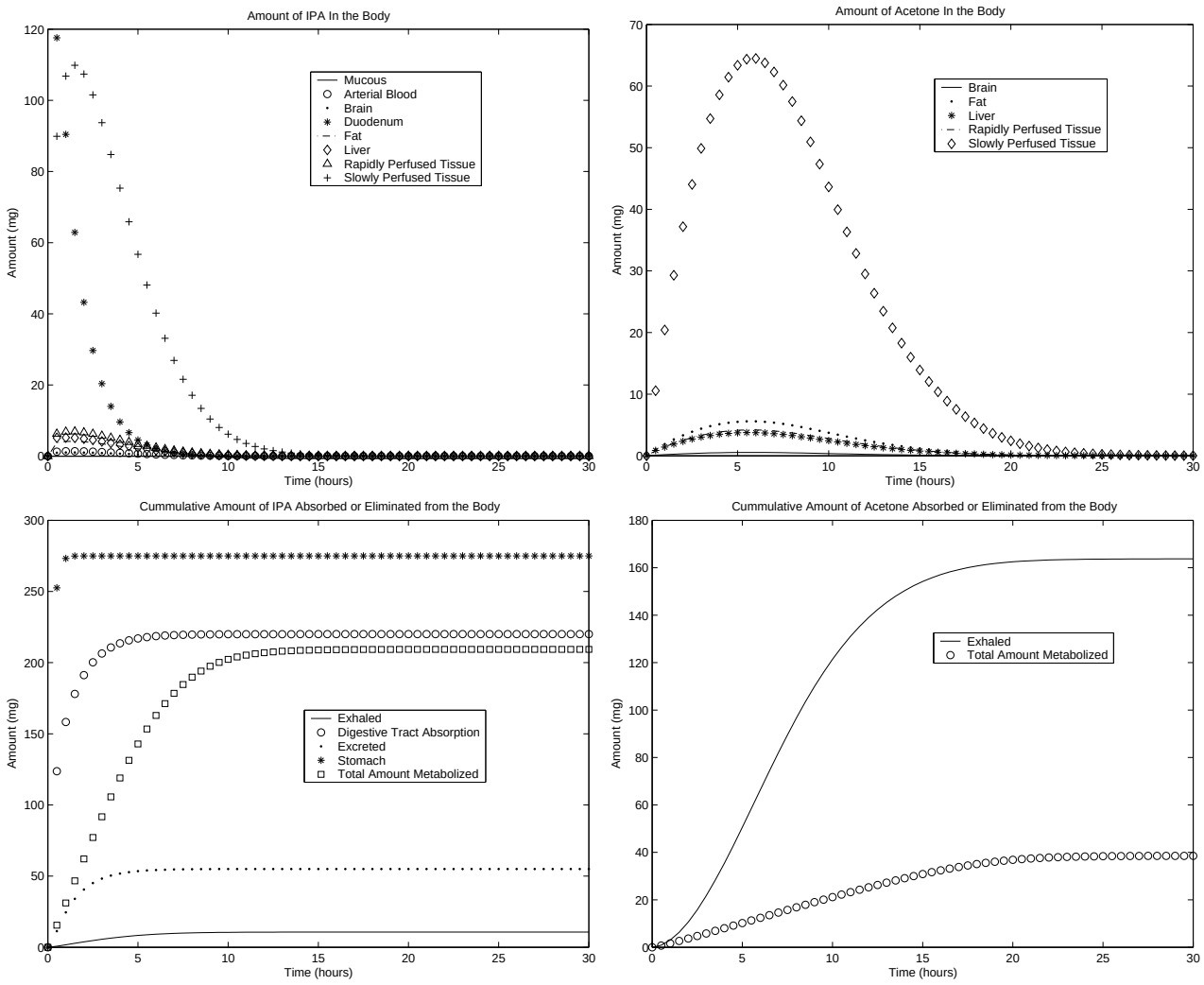

Figure 4.2: Model Simulations

4.2 Sensitivity Analysis

Due to the complexity of the biological system, the PBPK model we studied is inherently complex. The goal of modeling the system with the PBPK model is to predict risk of toxicity to humans based on small datasets and across multiple exposure routes. Mathematically this results in a system of twenty-nine coupled differential equations with over fifty parameters. Because of the high dimensionality of the system we decided to utilize MATLAB© computing software to obtain numerical solutions to the ODEs. But before we could invoke numerical techniques we had to make some choices regarding the system. We had to discern from the literature and our problem presenters, Drs. Barton and Setzer, what quantities were of most interest to biologists and the Environmental Protection Agency (EPA).

Making the distinction between variables, outcomes, constants, and parameters involved considerable discussion. At the onset we let all the amounts in the compartments (Table 4.1) be variables and set all other amounts to be parameters (with the exception of Body weight which we considered to be a constant).

For example, the rate of absorption from the duodenum to the liver (K_{AD}) is thought of as a constant in the experimental design. Yet, this rate is not directly measured in IPA PK experiments. Rather the value for K_{AD} is set based on "well established" results from other laboratories and studies. Since it is probable that

the effects of changes in K_{AD} affect the output over time, it would be reasonable if were thought of as variable (in the mathematical sense).

In the interest of time, we reduced our initial list of (mathematical) parameters to include only the metabolic parameters V_{Max}, K_M, K_{FC}, and set the body weight, blood flows, tissue volumes, uptake parameters, clearance parameters, and partition coefficients, to be constants in the mathematical sense. The numerical outputs we obtained were amounts of IPA and acetone in the tissues and blood. We chose the metabolic parameters since the literature suggests that parameter estimation schemes for the metabolic parameters may still need improvement due to the fact that different studies have cited different parameter values. If time was not an issue, all parameters should be studied, however, we have chosen to provide a sample of what should be calculated.

To evaluate the PBPK model that we were given, a sensitivity analysis was essential. The sensitivity analysis yields information about which parameters play a significant role in model outcomes, as well as the times when parameters effect model outcomes the most. Ultimately the information gained from a thorough sensitivity analysis could lead to the addition or deletion of compartments of the model and thereby provide the EPA with a guideline for the effectiveness and efficiency of the model.

4.2.1 Analytic Derivation of Sensitivity Analysis

Here we use the variational approach to derive an equation for the sensitivity of our system with respect to parameters. Our model can be represented as a system of differential equations

$$\begin{aligned} \dot{Y}(t,\mathbf{q}) &= f(t,Y(t,\mathbf{q}),\mathbf{q}) && (4.1)\\ Y(0,\mathbf{q}) &= Y_0 && (4.2) \end{aligned}$$

where $\cdot$ represents the derivative with respect to time, t is time, Y is the state of the system, and $\mathbf{q}$ is the vector of parameters.

Formally differentiating with respect to the parameters $\mathbf{q}$ we obtain

$$\begin{aligned} \frac{d}{d\mathbf{q}}\dot{Y}(t,\mathbf{q}) &= \frac{\partial}{\partial\mathbf{q}} f(t,Y(t,\mathbf{q}),\mathbf{q}) && (4.3)\\ &= \frac{\partial f}{\partial Y}(t,Y(t,\mathbf{q}),\mathbf{q})\cdot\frac{\partial Y}{\partial\mathbf{q}}(t,\mathbf{q}) + \frac{\partial f}{\partial\mathbf{q}}(t,Y(t,\mathbf{q}),\mathbf{q}). && (4.4) \end{aligned}$$

Then interchanging the order of differentiation we have

$$\frac{d}{dt}\frac{dY}{d\mathbf{q}}(t,\mathbf{q}) = \frac{\partial f}{\partial Y}(t,Y(t,\mathbf{q}),\mathbf{q})\cdot\frac{\partial Y}{\partial\mathbf{q}}(t,\mathbf{q}) + \frac{\partial f}{\partial\mathbf{q}}(t,Y(t,\mathbf{q}),\mathbf{q}). \quad (4.5)$$

If we let $z = \frac{\partial Y}{\partial\mathbf{q}}(t,\mathbf{q}_0)$, near a point where $q = q_0$ then equation (4.1) becomes

$$\dot{z} = A(t)\cdot z(t) + F(t) \quad (4.6)$$

with

$$A(t) = \frac{\partial f}{\partial Y}(t,Y(t,\mathbf{q}_0),\mathbf{q}_0) \quad (4.7)$$

$$F(t) = \frac{\partial f}{\partial\mathbf{q}}(t,Y(t,\mathbf{q}_0),\mathbf{q}_0). \quad (4.8)$$

This system of differential equations can be written for the $n\times m$ sensitivity matrix $\frac{\partial Y}{\partial\mathbf{q}}(t,\mathbf{q})$ (n = number of compartments of the PBPK model, m = number of parameters). The solution to (4.6) is the sensitivity of the system near $\mathbf{q}_0$.

4.2.2 Interpretation of the Sensitivity of Parameters Over Time

Using the MATLAB© program sys_sen.m (Molla), we obtain the solution to the system of differential equations as well as the matrix of partial derivatives of the outputs with respect to the parameters. The program was run using an inital intravenous dose of 1,000 mg/kg, as well as an oral dosage of 0.1 mg/kg. The plots of these partial derivatives show at what points in time the outputs in question are most sensitive to changes in the particular parameter values. Maximum or minimum values represent times when the parameter in question is most sensitive. This information allows for the judicious selection of parameters to adjust and improve the fit of the output at a particular point in time. Some of the resulting figures are discussed below, while the remaining figures can be found in the Sensitivity Analysis Appendix. These figures depict partial derivatives of amounts and concentrations with respect to various metabolism parameters.

Sensitivity of A_{Liv}

Figure 4.3a depicts the partial derivatives of A_{Liv} with respect to V_{Max} and A_{Liv1} with respect to V_{Max1}. Note that the maximum effect of, or sensitivity of, A_{Liv} to V_{Max} occurs at the minimum of the derivative $\frac{\partial A_{Liv}}{\partial V_{Max}}(t)$; between four and five hours after the initial dosing. The peak sensitivity of A_{Liv1} with respect to V_{Max1} similarly occurs at around hour twelve.

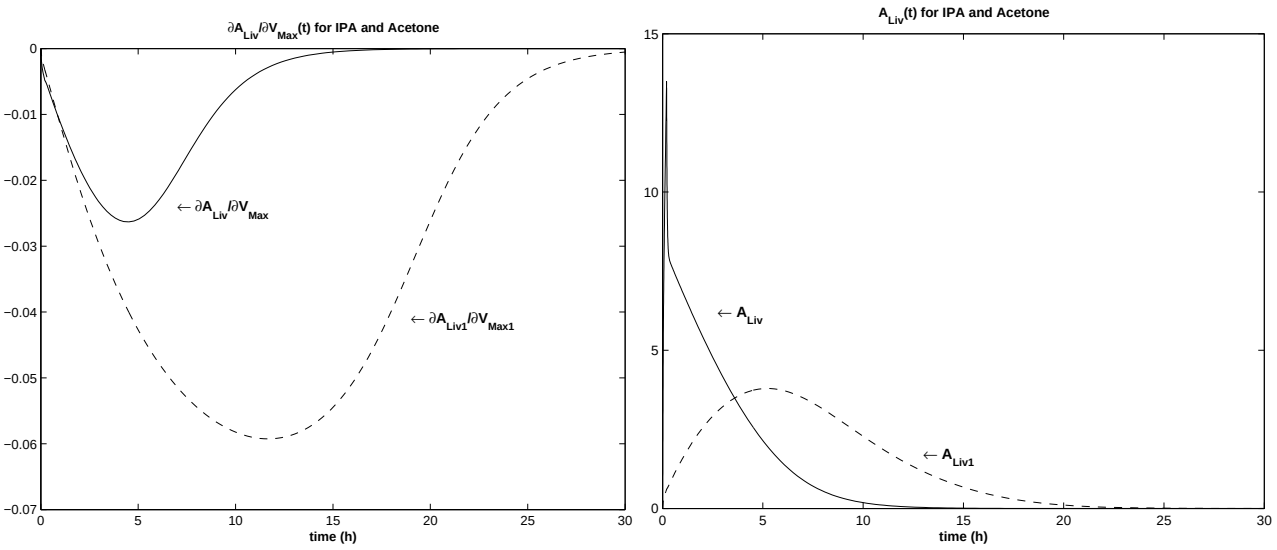

Figure 4.3: a) $\frac{\partial A_{Liv}}{\partial V_{Max}}$ and $\frac{\partial A_{Liv1}}{\partial V_{Max1}}$, b)Cumulative A_Liv and A_Liv1

In Figure 4.3b we show A_{Liv} and A_{Liv1}, the amount of isopropanol and acetone in the venous blood. The amount of IPA and acetone coincide at about five hours, just before the amount of acetone peaks. At around hour twelve there appears to be an inflection point in the amount of acetone, which corresponds to the maximum sensitivity of A_{Liv1} to V_{Max1}.

Sensitivity of C_{Ven}

Figure 4.4a depicts the partial derivatives of C_{Ven} and C_{Ven1}, the concentration of IPA and acetone in the venous blood, with respect to the IPA and acetone metabolism parameters V_{Max} and V_{Max1}, respectively. These plots show that the maximum sensitivity reaches a constant value in time at around hour fifteen for V_{Max} and hour twenty-four for V_{Max1}. These are actually the times when the concentration of the chemical has reached a steady-state in the blood stream, namely zero.

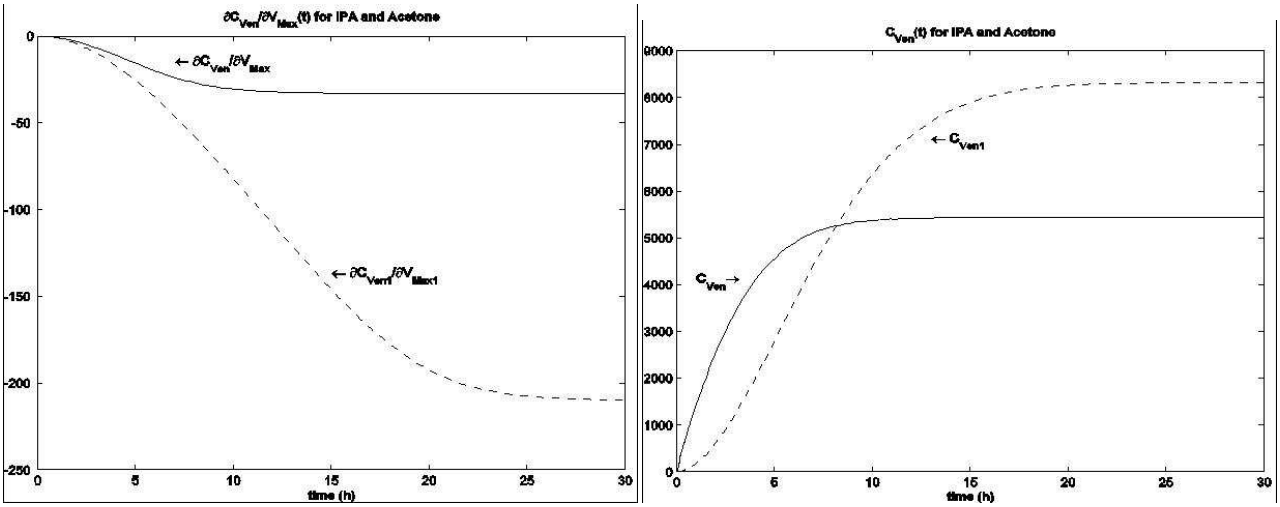

Figure 4.4: a) $\frac{\partial C_{Ven}}{\partial V_{Max}}$ and $\frac{\partial C_{Ven1}}{\partial V_{Max1}}$, b)Cumulative C_Ven and C_Ven1

Figures 4.4b depicts cumulative concentrations C_{Ven} and C_{Ven1}, the concentration of IPA and acetone in the venous blood. This reiterates the impression obtained from Figure 3, in that the concentration reaches a constant at around hour fifteen for C_{Ven} and around hour twenty-four for C_{Ven1}. Intuitively, this makes sense because isopropanol is being metabolized into acetone, which then remains in the body for a longer period of time.

4.3 A Sensitivity Metric Using Stochastic Simulation

We used random variables to model the consequences of the inherent uncertainty in the values of the parameters. Traditional sensitivity analysis, which we illustrated above, allows us to observe change in output of a system when altering the value of one parameter while holding the others constant. In addition, it is of interest to observe how the output is affected when multiple parameters are simultaneously adjusted, effectively giving some idea of the interaction between parameters. By varying the parameter space, we may observe changes in variance of the output of the system.

The method employed in this system begins with generating random values for the parameters. We may use previously estimated values from the literature to determine mean and possibly variance of the generated random variables. The system is then solved numerically for a specified time, exposure method, and exposure level. The resulting variation for the state variables of interest can then be observed. The primary elements of interest in this system are the venous blood concentrations for both Isopropanol and Acetone, as well as the arterial blood integrals evaluated over time.

The three parameters that Clewell, et al., cited as having calculated differing values are the three parameters we decided to observe: metabolism maximum reaction rate(Vmax), upper respiratory tract uptake (Clmuc) and absorption from the stomach(kAS). A lognormal distribution was placed on the parameters and 100,000 random values were generated. The system was then solved for each random parameter at a dosage of 1000 mg/kg of oral exposure of Isopropanol. Values for area under the concentration curve in arterial blood for both Isopropanol and Acetone were outputted using the numerical solver MCSim. These values were imported into the following histograms (Figures 4.5a and b).

Interpretation for Isopropanol (Figure 4.5a): The distribution for the area under the arterial blood concentration curve is skewed left with values ranging from approximately 3,000 to 5,000 mg-hr/liter. The typical value obtained without varying parameters was 4,807 mg-hr/liter, which lies at the peak. Roughly 50% of the

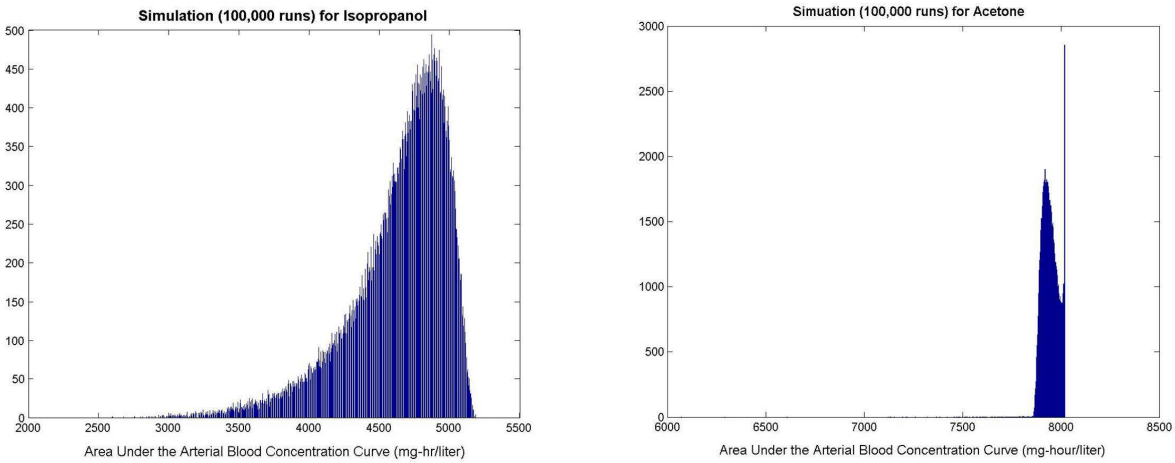

Figure 4.5: a) IPA b) Acetone

values for area under the curve (AUC) fall between 4,300 and 5,200 mg-hr/liter. It appears that varying the three parameters can cause the area under the concentration curve for arterial blood to differ.

Interpretation for Acetone (Figure 4.5b): The distribution for the area under the arterial blood concentration curve is relatively small. It too is skewed left with values lumped between 7,750 and 8,000 mg-hr/liter. Because of the tight concentration interval, varying the three parameter values did not appear to effect the AUC, which was expected since the parameters that were varied were parameters for isopropanol and not acetone. We would expect a greater variability of AUC for IPA. The apparent spike in AUC at 8,135 mg-hr/liter (typical value) occurs because the body can only clear acetone from its system so quickly. For large levels of V_{Max}, isopropanol enters the system very quickly and is metabolized into acetone almost immediately. This leaves large amounts of acetone that has to be cleared from the body.

We were also interested in the effect scaling the variance of the parameters had on area under the arterial blood concentration curve. For example, with the parameter kAS, we ran simulations using halved and doubled variance. The results are shown below Table 4.3):

Scale Factor of Variance for kAS	Variance of AUC for IPA	Variance of AUC for Acetone
2	566,120	166,180
1	127,290	1,855.2
0.5	26,160	520.48

Table 4.3: Scaled KAS

Interpretation for Scaling the kAS parameter (Table 4.3): In studying the variance of AUC for IPA when scaling the kAS parameter, there appears to be a five-fold difference for each scale factor. This means that one would expect the variance in values for kAS to increase/decrease by a multiple of five. The more variance placed on kAS, the greater the variability in area under the concentration curve for IPA, or the greater the uncertainty in the model output. In contrast, there appears to be a three-fold difference for the variance of AUC for acetone when the variance for kAS is halved, while there appears to be a ninety-fold difference for the variance of AUC for acetone when doubling the variance of kAS. Since the parameters that were varied were parameters for isopropanol, we would not expect to observe a constant difference for the variance of AUC for acetone when scaling the variance of kAS.

4.4 Conclusions and Further Discussion

The focus of work over the past week has been on sensitivity analysis. There is quite a bit of work still left to do on this aspect of the model. We looked at only a small set of parameters; increasing this set would be the first step to take. Also, our analysis only looked at sensitivity near the parameter values that biologists hypothesized. A wider range of values should be investigated. A good way to present such results would be to use cumulative arterial/venous blood concentrations for a large enough time so that this value has reached steady state. This would represent the area under the curve (AUC). We then could investigate sensitivity for these large times. These results could be interpreted as the sensitivity of AUC with respect to certain parameters. Parameters could be eliminated based on their sensitivity with respect to AUC–since this value seems to be of such importance to biologists.

Another method we utilized was analyzing sensitivity by putting random distributions on the parameters and then evaluating the distribution of the output. This method could be expanded to a larger number of parameters. We could then match this output to experimental data, to see if the data fits into these distributions. Along these lines, a Bayesian analysis of the data should be performed. A Bayesian analysis would allow for not only an integration of multiple sources of data, but would also allow for a more solid interpretation of uncertainty in the parameters. A problem with this approach is the scarcity of data. For an appropriate interpretation of uncertainty in the parameter, one would need a substantial amount of data. Otherwise, we will only see the uncertainty attached to the model via the prior distributions of the parameters. However, Bayesian parameter fitting might be the most promising for such a large model.

4.4.1 Acknowledgments

We would like to thank our problem presenters, Dr. Hugh Barton and Dr. Woodrow Setzer, from the Environmental Protection Agency, and our faculty consultant Dr H.T. Banks from North Carolina State University. We would also like to thank Karen Chiswell from NCSU and Dr. Leona Harris Clark from the EPA for their help throughout this project.

Bibliography

[1] Kubiak et al., *Modeling Control of HIV Infection Through Structured Treatment Interruptions with Recommendations for Experimental Protocol,* CRSC Technical Report, CRSC-TR01-27, November 2001. Raleigh, NC.

[2] Molla, V. M. Garcia and R. Gomez Padilla. " Description of the MATLAB functions SENS_SYS and SENS_IND." Universidad Politecnica di Valencia Webpage.

[3] Kumagai, S and Matsunaga, I. "Physiologically based pharmacokinetic model for acetone", *Occup Environ Med.* , 1995, Vol 52, No 5:344-52.

[4] Fisher et al. "Analysis of Respiratory Exchange of Methanol in the Lung of the Monkey Using a Physiological Model." *Toxicological Sciences* , 2000, Vol 53 : 185-193.

[5] Clewell et al. "Development of a Physiologically Based Pharmacokinetic Model of Isopropanol and Its Metabolite Acetone." *Toxicological Sciences* , 2001, Vol 63 : 160-172.

[6] Clark, Leona Harris. "PBPK Isopropanol/Acetone Model." Model encoded for MCSim Software, United States Environmental Protection Agency, 2002.

[7] Isukapalli, Sastry and Georgopoulos, Panos. "Computational Methods for Sensitivity and Uncertainty Analysis for Environmental and Biological Models." EPA Technical Report, 2001.

[8] Firestone, Michael (chair). "Guiding Principles for Monte Carlo Analysis." EPA Technical Report, 1997.

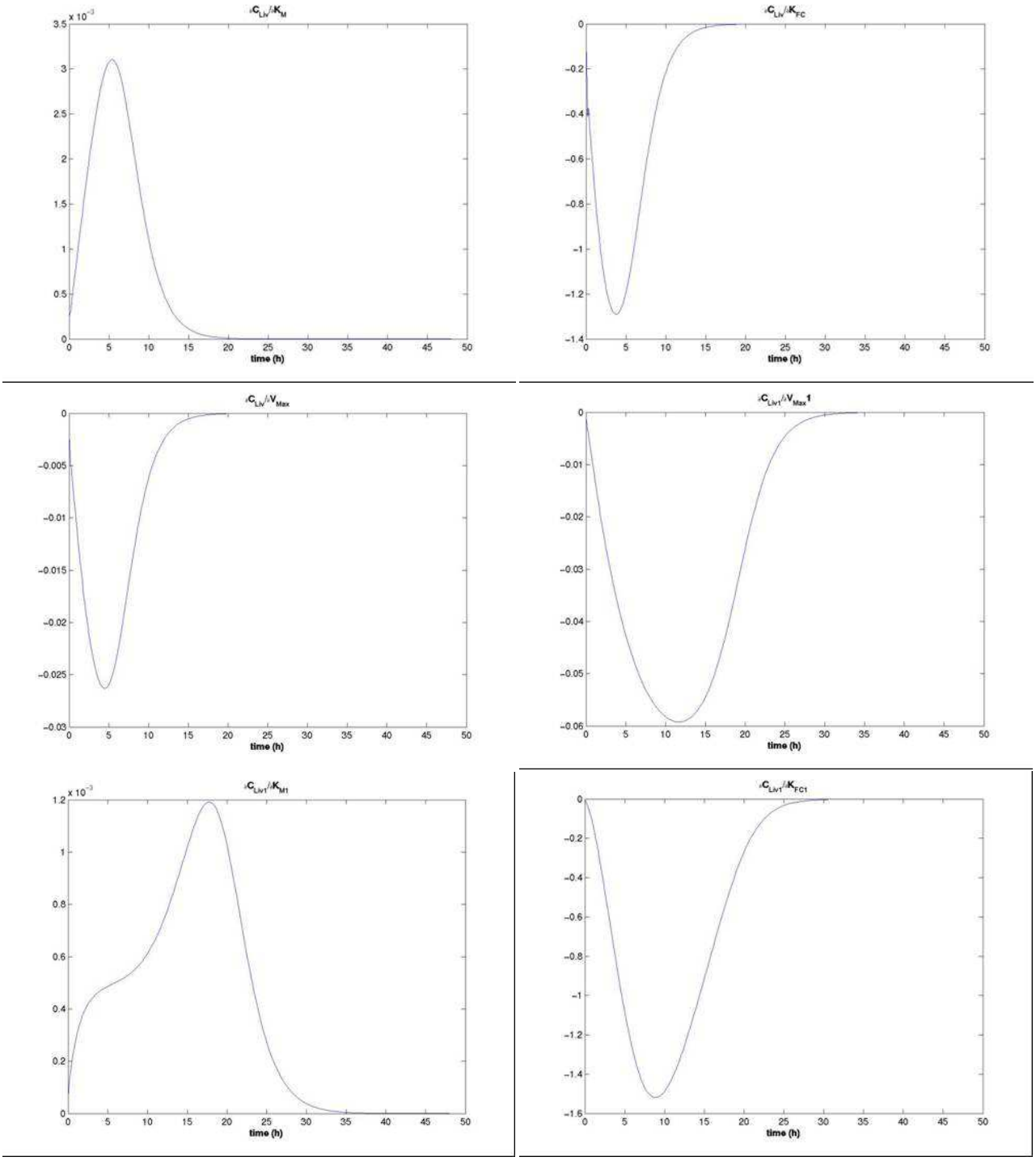

Figure 4.6: Sensitivity Analysis

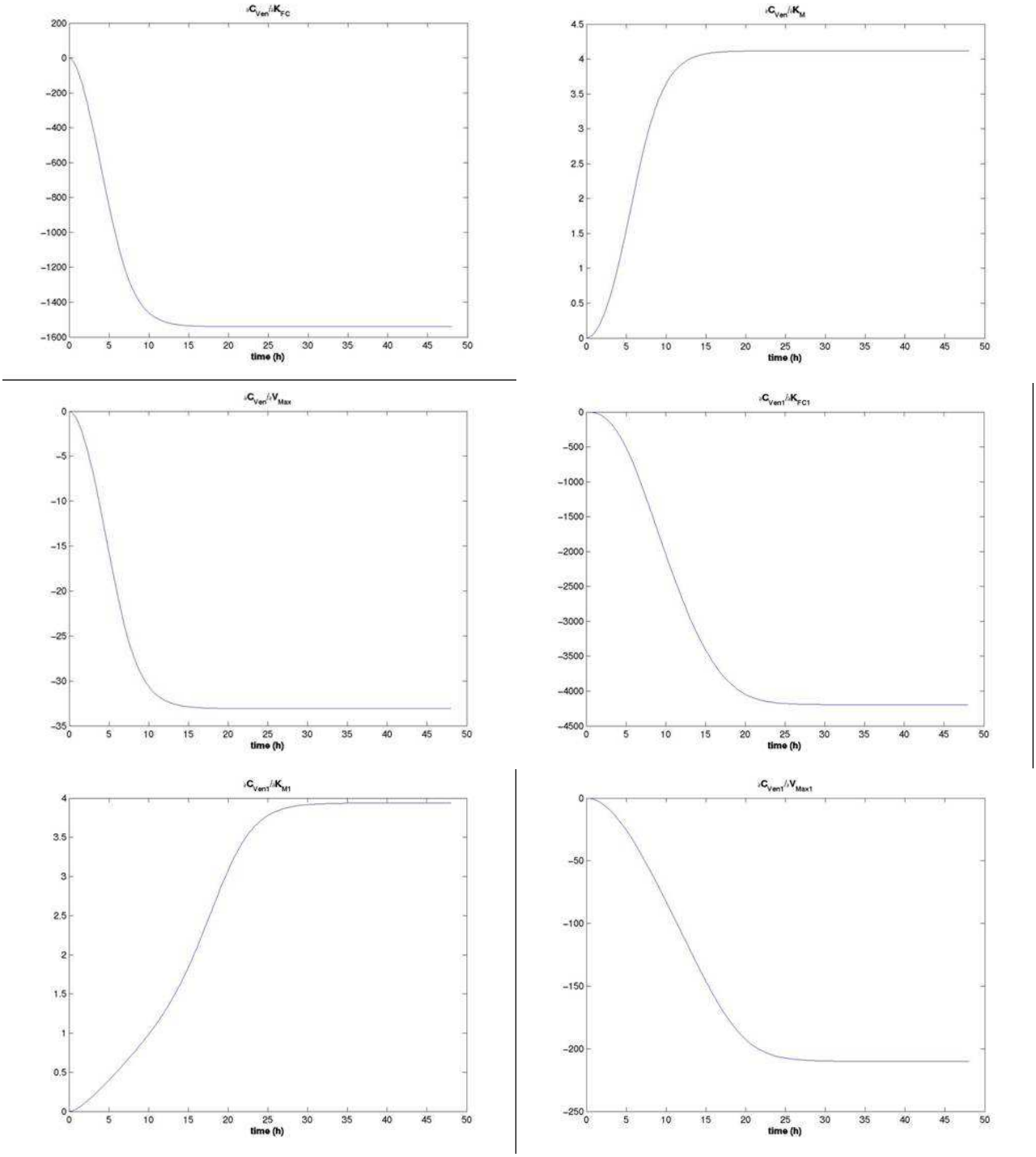

Figure 4.7: Sensitivity Analysis

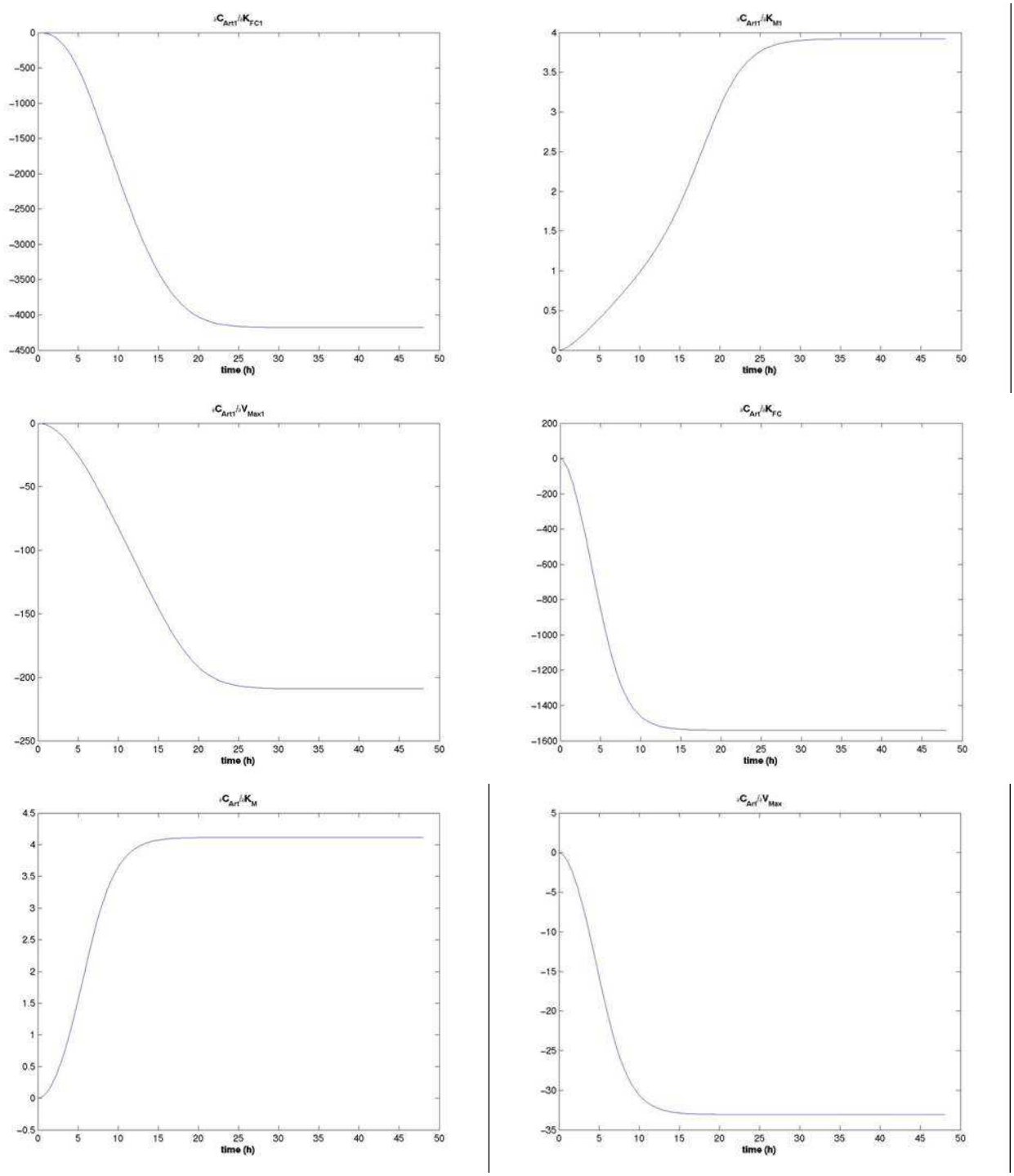

Figure 4.8: Sensitivity Analysis

Chapter 5

Effect of Interstitial Gas on Powder Flow

Balajee Ananthasayanam[1], Yujuan Bao[2], Edna Chan[3], Pengwen Chen[4], James Gibert[5], Serguei Lapin[6]

Problem Presenter:
T. Anthony Royal
Jenike & Johanson, Inc.

Faculty Consultant:
Dr. Pierre Gremaud
NCSU

Abstract

The problem of flow and consolidation of fine-grained bulk solids through a vessel comprised of cylinders, cones and a cylinder-cone combination is modeled in this paper. Unlike coarse-grained bulk solids, the pressure of the gases trapped between the solid particles is substantial when the powder is fine. Therefore, the flow of powder is treated as a two-phase interaction between gases and solids. To simplify the modeling of the problem, spatial averaging is adopted. This formulation, even though 1-D in space, includes geometry effects of the container. The model is derived using mass continuity and force equilibrium resulting in three partial differential equations that describe the density of the solid, the velocity of the solid and the pressure of the gas. Apart from the three partial differential equations, the model also contains an ordinary differential equation that describes the height of the powder in the vessel, or the free boundary, in time. Furthermore, a numerical method based on finite difference approximations in space and a Runge-Kutta method in time are implemented. Computational results are presented to discuss the validity of this approach.

5.1 Introduction and Motivation

A powder is defined as a material made up of many individual solid particles of sizes ranging from 10^{-7}m to 10^{-5}m. Fine particles poses unique challenges in filling and discharge through a vessel. If the filling rate is very large, the gas will not immediately escape which leads to the development of excessive gas pressure. This phenomenon causes the powder to become fluidized. Fluidization can lead to easy withdrawal of the

[1]Clemson University
[2]Duke University
[3]North Carolina State University
[4]University of Florida
[5]Clemson University
[6]University of Houston

powder. However, it poses problems since the increase in pressure can cause structural failure in the vessel. In addition to structural problems, the easy withdrawal can lead to flooding, a sudden, rapid discharge of fine powder. Fluidization is a transient condition; over time, the gas will escape and consolidation will occur. This paper derives the mathematical model that arises from the analysis of the flow and consolidation of powder in a vessel. The application of this model is to develop an engineering tool to predict and prevent flooding without severely limiting the flow rate of powder out of the vessel. Section 2 of the paper deals with the underlying physical principles that govern the behavior of the problem and the resulting mathematical model. The model is based on conservation of mass, force equilibrium and Darcy's law. The model proposed differs from previous works by including the inertial effects of the solid particles. This addition allows the study of both steady and transient effects of powder flow. In Section 3, a numerical method is proposed to solve the governing equations for the system. The mathematical structure of the problem consists of three partial differential equations (PDEs) and an ordinary differential equation (ODE). The equations can be separated by spatial and temporal derivatives. This leads to a finite difference approximation of the spatial derivatives resulting in a system of 1st order differential equations in time that is solved using a classical Runge-Kutta method. Finally, various computational results are presented to explore the nature of the predicted response. Numerical results are presented in Section 4. Concluding remarks and future work are described in Section 5.

5.2 Derivation of the model

The model derived here can be applied to cylindrical silos of general cross-section. Cylindrical towers, funnel-shaped structures or combinations of those two where the cylindrical tower is mounted on top of the funnel-shaped structure are typical examples, see Figure 5.1. The problem formulation is simplified by considering averages on horizontal cross-sections. The cross-sectional area is denoted by $A(z)$ where z represents the vertical spatial coordinate, taken positive in the upward direction. Powder can be filled into the silo from the top and/or retrieved from outlets at the bottom. Further, even in the absence of those two issues, the material settles under gravity. As a consequence, the height of the powder, $z_T(t)$, in the silo changes with respect to time t. Consider a slice of height Δz across the vessel. The derivation of the model relies on two essential

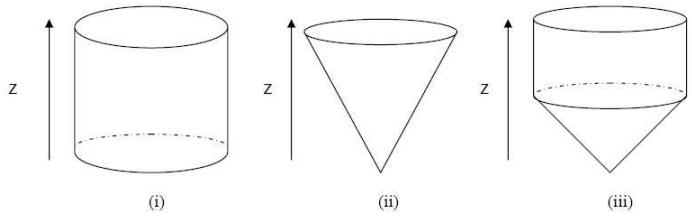

Figure 5.1: Silos

conditions: continuity of gas and solids on the one hand, and and equilibrium of forces and pressures on the other hand. This mimics the equations found in the work of Jenike and Johanson [4].

Continuity of Gas and Solid

The analysis begins by considering the control volume in Figure 5.2. The flow of the solid and gas in and out, and the storage terms in the control volume are allowed to change with time. The continuity of the gases in the control volume is

$$\dot{m}_{i,g} - \dot{m}_{st,g} = \dot{m}_{o,g}, \tag{5.1}$$

while the continuity of the solids is represented by the following equation

$$\dot{m}_{i,s} - \dot{m}_{st,s} = \dot{m}_{o,s}. \tag{5.2}$$

Rearranging Eqs.(5.1) and (5.2) yields

$$\dot{m}_{st,g} = (\dot{\nu\rho})A\Delta z = -\dot{m}_{o,g} + \dot{m}_{i,g} \tag{5.3}$$

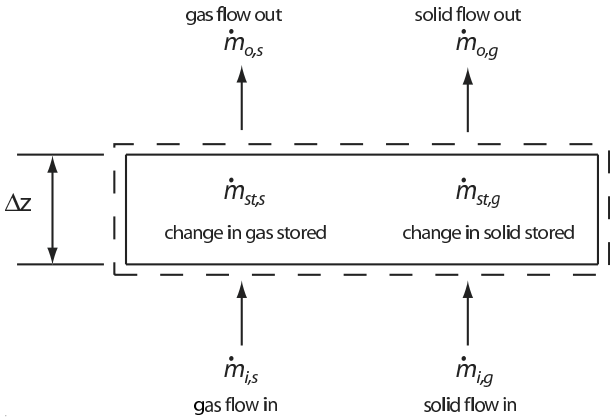

Figure 5.2: Control Volume Analysis

$$\dot{m}_{st,s} = \frac{\dot{\gamma} A \Delta z}{g} = -\dot{m}_{o,s} + \dot{m}_{i,s} \tag{5.4}$$

where $\nu = 1 - \gamma/\Gamma$ is the voids ratio and γ is the bulk density of each cross-section. It has been shown by well supported experimental studies [6] that bulk density γ is a function of vertical stress σ and is given by the expression

$$\gamma = \gamma_m \left(1 + \frac{\sigma}{\sigma_m}\right)^{\beta} \tag{5.5}$$

where $0 \leq \beta < 1$ is the coefficient of compressibility, $\sigma_m > 0$ and $\gamma_m > 0$ are material constants. We can now simplify the above equations to obtain

$$(\dot{\nu\rho}) A \Delta z = -\Delta \dot{m}_g, \tag{5.6}$$

$$\frac{\dot{\gamma} A \Delta z}{g} = -\Delta \dot{m}_s. \tag{5.7}$$

Dividing by Δ_z in both equations yield

$$(\dot{\nu\rho}) A = \frac{-\Delta \dot{m}_g}{\Delta z}, \tag{5.8}$$

$$\frac{\dot{\gamma} A}{g} = \frac{-\Delta \dot{m}_s}{\Delta z}. \tag{5.9}$$

We can rewrite the equations as two PDEs,

$$\frac{\partial(\nu\rho)}{\partial t} + \frac{1}{A}\frac{\partial \dot{m}_g}{\partial z} = 0 \tag{5.10}$$

and

$$\frac{\partial \gamma}{\partial t} + \frac{g}{A}\frac{\partial \dot{m}_s}{\partial z} = 0, \tag{5.11}$$

by taking the appropriate limits. Substituting the physical relationships for mass flow rate into the above two PDEs, the respective conservation of mass for gas and solids equations become

$$\frac{\partial(\nu\rho)}{\partial t} + \frac{1}{A}\frac{\partial(\nu\rho A V_g)}{\partial z} = 0, \tag{5.12}$$

$$\frac{\partial \gamma}{\partial t} + \frac{1}{A}\frac{\partial(\gamma A V_s)}{\partial z} = 0. \tag{5.13}$$

The velocity of the gas can never truly be known and can be eliminated from the previous equations by introducing Darcy's law, a relation between velocity and pressure. It is given as

$$V_g - V_s = -K\frac{\partial p}{\partial z} \tag{5.14}$$

A	=	cross-sectional area of silo
g	=	gravitational constant
k	=	ratio of wall normal stress, σ_w to average vertical stress, σ. $k = \sigma_w/\sigma$
K	=	permeability of bulk to fluid flow given by Darcy's law
$\dot{m}_g$	=	mass flow rate of gas
$\dot{m}_s$	=	mass flow rate of solid
p	=	interstitial fluid pressure
t	=	time
V_s	=	velocity of solid
V_g	=	velocity of gas
z	=	spatial coordinate, up is positive
ρ	=	fluid mass density
σ	=	average vertical compressive stress
Γ	=	solid particles weight density
γ	=	bulk weight density
ν	=	porosity $\nu = 1 - \gamma/\Gamma$
θ	=	hopper wall angle measured from the vertical axis
ϕ'	=	wall friction angle

Table 5.1: Summary of notations

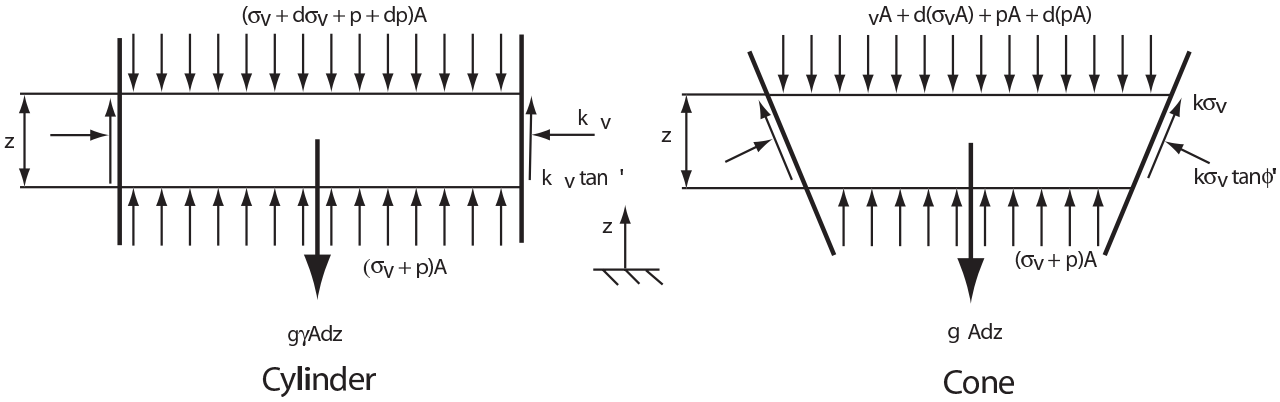

Figure 5.3: Force Balance

where $K = K_0 \left(\frac{\gamma}{\gamma_0}\right)^{-\alpha}$ is the permeability. Here K_0, γ_0 are reference values and α is a positive constant.

Conservation of Momentum
The equation of motion for the solid particles can be seen by examining a freebody of the control volume, refer to Figure 5.3. The equilibrium of forces in the vertical direction can be written as

$$\begin{aligned}&(\sigma + p)A - (\sigma + \Delta\sigma + p + \Delta p)(A + \Delta A) + \oint_c \sigma_n(\tan\theta + m_f \tan\phi')dc\Delta z + p\Delta A - \gamma A\Delta z \\ &= A\Delta z \frac{\gamma}{g}\left(\frac{\partial V_s}{\partial t} + V_s\frac{\partial V_s}{\partial z}\right).\end{aligned} \tag{5.15}$$

Dividing the equilibrium equation by A and Δz and taking the appropriate limits, yields the following PDE

$$\frac{d\sigma}{dz} = -\frac{\sigma}{A}\frac{dA}{dz} - \frac{dp}{dz} + \frac{1}{A}\oint_c k\sigma(m_f \tan\phi' + \tan\theta)dc - \gamma - \frac{\gamma}{g}\left(\frac{\partial V_s}{\partial t} + V_s\frac{\partial V_s}{\partial z}\right) \tag{5.16}$$

where m_f = 1 for flow down, m_f = -1 for flow up, and k is the ratio of the normal stress to the wall to the average vertical stress.

Height of the Powder
An equation describing the height of the powder can be obtained by considering the entire silo as a control volume. The mass in the silo can be written as

$$M = \int_{z_B}^{z_T} A\frac{\gamma}{g} dz. \tag{5.17}$$

The flow of mass in and out of the silo can be described by the following continuity relationship

$$\frac{dM}{dt} = \dot{m}_T - \dot{m}_B. \tag{5.18}$$

Substituting Eq.(5.18) into Eq.(5.17) and simplifying yields

$$\frac{dM}{dt} = \int_{z_B}^{z_T} \frac{A}{g}\frac{\partial \gamma}{\partial t} dz + A(z_T)\frac{\gamma(z_T)}{g}\frac{dz_T}{dt} - \cancelto{0}{A(z_B)\frac{\gamma(z_B)}{g}\frac{dz_B}{dt}}. \tag{5.19}$$

The expression for $\frac{\partial \gamma}{\partial t}$, Eq.(5.13), can be substituted into Eq.(5.19) yielding

$$\dot{m}_T - \dot{m}_B = -\frac{\gamma(z_T)A(z_T)V_s(z_T)}{g} + \frac{\gamma(z_B)A(z_B)V_s(z_B)}{g} + \frac{A(z_T)\gamma(z_T)}{g}\frac{dz_T}{dt}. \tag{5.20}$$

It can now be noted that $\dot{m}_B = -\gamma(z_B)A(z_B)V_s(z_B)/g$. This allows the preceding equation to become

$$\dot{m}_T = \left(\frac{dz_t}{dt} - V_s(z_T)\right)\frac{A(z_T)\gamma(z_T)}{g}. \tag{5.21}$$

This expression can be rearranged to an ordinary differential equation describing the movement of the top boundary in time.

$$\frac{dz_T}{dt} = \frac{g\dot{m}_T}{\gamma(z_T)A(z_T)} + V_s(z_T). \tag{5.22}$$

It can be easily seen that if no material is poured into the silo, the top boundary changes at the same rate as the velocity of the particles at the top.

Model Equations
Summarizing the above derivation, the following mathematical formulation is obtained

$$\frac{\partial(\nu p)}{\partial t} + \frac{1}{A}\frac{\partial(A\nu p(-K\frac{\partial P}{\partial z} + V_s))}{\partial z} = 0, \tag{5.23}$$

$$\frac{\partial \gamma}{\partial t} + \frac{1}{A}\frac{\partial(AV_s\gamma)}{\partial z} = 0, \tag{5.24}$$

$$\frac{\partial \sigma}{\partial z} = -\frac{\sigma}{A}\frac{dA}{dz} - \frac{\partial P}{\partial z} + \frac{1}{A}\oint_c k\sigma(m_f \tan\phi' + \tan\theta)dc - \gamma - \frac{\gamma}{g}\left(\frac{\partial V_s}{\partial t} + V_s\frac{\partial V_s}{\partial z}\right), \tag{5.25}$$

$$\gamma = \gamma(\sigma), \tag{5.26}$$

$$\dot{m}_T = \left(\frac{dz_t}{dt} - V_s(z_T)\right)\frac{A(z_T)\gamma(z_T)}{g}, \tag{5.27}$$

In order to simplify the modeling of the problem, we mapped the problem into a fixed spatial domain by introducing the variable

$$y = \frac{z}{z_T}. \tag{5.28}$$

Hence, the following relationships between spatial and time derivatives hold true

$$\frac{\partial}{\partial z} = \frac{1}{z_T}\frac{\partial}{\partial y}, \qquad \frac{\partial^2}{\partial z^2} = \frac{1}{z_T^2}\frac{\partial^2}{\partial y^2}, \qquad \frac{dy}{dt} = \frac{-y}{z_T}\frac{dz_T}{dt}. \tag{5.29}$$

Now, let $C = \oint_c k(m_f tan\phi' + tan\theta)dc$ and mapping to the new domain, Eqs.(5.23)-(5.25) can be written as

$$\frac{\partial(\nu p)}{\partial t} - \frac{\partial(\nu p)}{\partial y}\frac{y}{z_T}\frac{dz_T}{dt} + \frac{1}{Az_T}\frac{\partial(A\nu p(\frac{-K}{z_T}\frac{\partial P}{\partial y} + V_s))}{\partial y} = 0, \tag{5.30}$$

$$\frac{\partial \gamma}{\partial t} - \frac{\partial \gamma}{\partial y}\frac{y}{z_T}\frac{dz_T}{dt} + \frac{1}{Az_T}\frac{\partial(AV_s\gamma)}{\partial y} = 0, \tag{5.31}$$

$$\frac{1}{z_T}\frac{\partial \sigma}{\partial y} = -\frac{\sigma}{A}\left(\frac{dA}{dy}\frac{1}{z_T} - C\right) - \frac{1}{z_T}\frac{\partial P}{\partial y} - \gamma - \frac{\gamma}{g}\left(\frac{\partial V_s}{\partial t} - \frac{y}{z_T}\frac{dz_T}{dt}\frac{\partial V_s}{\partial y} + \frac{V_s}{z_T}\frac{\partial V_s}{\partial y}\right). \tag{5.32}$$

The porosity ν is dependent on the bulk density γ by $\nu = (1 - \gamma/\Gamma)$. Hence, $\partial\nu/\partial t = -1/\Gamma\partial\gamma/\partial t$. Expressing $\partial(\nu p)/\partial t = \nu\partial p/\partial t + p\partial\nu/\partial t$, and after substituting $\frac{\partial\gamma}{\partial t}$ from Eq.(5.31), we can rewrite Eqs.(5.30)-(5.32) as

$$\frac{\partial p}{\partial t} = \frac{1}{\nu}\left[\frac{p}{\Gamma}\left(\frac{\partial\gamma}{\partial y}\frac{y}{z_T}\frac{dz_T}{dt} - \frac{1}{Az_T}\frac{\partial(AV_s\gamma)}{\partial y}\right) + \frac{\partial(\frac{\Gamma p}{\Gamma-\gamma})}{\partial y}\frac{y}{z_T}\frac{dz_T}{dt} - \frac{1}{Az_T}\frac{\partial(A\nu p(\frac{-K}{z_T}\frac{\partial p}{\partial y} + V_s))}{\partial y}\right], \tag{5.33}$$

$$\frac{\partial \gamma}{\partial t} = \frac{\partial \gamma}{\partial y}\frac{y}{z_T}\frac{dz_T}{dt} - \frac{1}{Az_T}\frac{\partial(AV_s\gamma)}{\partial y}, \tag{5.34}$$

$$\frac{\partial V_s}{\partial t} = -\frac{g}{\gamma}\left[\frac{1}{z_T}\frac{\partial\sigma}{\partial y} + \frac{\sigma}{A}\left(\frac{dA}{dy}\frac{1}{z_T} - C\right) + \frac{1}{z_T}\frac{\partial p}{\partial y} + \gamma\right] + \frac{y}{z_T}\frac{dz_T}{dt}\frac{\partial V_s}{\partial y} - \frac{V_s}{z_T}\frac{\partial V_s}{\partial y}, \tag{5.35}$$

$$\frac{dz_T}{dt} = \frac{g\dot{m}_T}{\gamma(z_T)A(z_T)} + V_s(z_T). \tag{5.36}$$

Eqs. (5.30)-(5.32) are nonlinear in space but can be viewed 1st order ODEs in time.

5.3 Discretization

The spatial domain can be divided into N intervals with a mesh step size $\Delta y = \frac{1}{N+1}$. Now, we introduce semidiscrete variables corresponding to the ones given in Table 1:

$$\begin{aligned}
\boldsymbol{y} &= [y_1, y_2, \dots y_{N+1}]^T, & \boldsymbol{p} &= [p_1, p_2, \dots p_{N+1}]^T,\\
\boldsymbol{p^+} &= [p_3, p_4, \dots p_{N+1}]^T, & \boldsymbol{p^-} &= [p_1, p_2, \dots p_{N-1}]^T,\\
\boldsymbol{p^c} &= [p_2, p_3, \dots p_N]^T, & \boldsymbol{V}_s &= [V_{s,1}, V_{s,2}, \dots V_{s,N+1}]^T,\\
\boldsymbol{\gamma} &= [\gamma_1, \gamma_2, \dots \gamma_{N+1}]^T, & \boldsymbol{\nu} &= [\nu_1, \nu_2, \dots \nu_{N+1}]^T,\\
\tilde{\boldsymbol{\nu}} &= [\nu_1^{-1}, \nu_2^{-1}, \dots \nu_{N+1}^{-1}]^T, & \boldsymbol{A} &= [A_1, A_2, \dots A_{N+1}]^T,\\
\tilde{\boldsymbol{A}} &= [A_1^{-1}, A_2^{-1}, \dots A_{N+1}^{-1}]^T.
\end{aligned}$$

Here, the first subscript corresponds to the mesh node at the bottom of the tank and $N+1$ corresponds to the top of the tank. We discretize Eqs. (5.33)-(5.36) using centered finite differences in space.

Equations for Pressure (Open Tank Case)

The partial differential equation, describing the change in pressure in both time and space, discrete form depends on the boundary conditions imposed on the problem. If the tank is open, the pressure at the top and bottom is fixed for all time. For $i = 1$

$$p_1 = 1 \Rightarrow \frac{\partial p_1}{\partial t} = 0. \tag{5.37}$$

For $i = 2, \dots N$

$$\begin{aligned}\frac{\partial p_i}{\partial t} = \frac{1}{\nu_i}\Bigg\{ & \frac{p_i}{\Gamma}\left[\frac{\gamma_{i+1}-\gamma_{i-1}}{2\Delta y}\frac{y_i}{z_T}\left(V_{S_{N+1}} + \frac{\dot{m_T}}{A_{N+1}\gamma_m}\right)\right. \\ & \left. -\frac{1}{A_i z_T}\left(\frac{A_{i+1}V_{S_{i+1}}\gamma_{i+1} - A_{i-1}V_{S_{i-1}}\gamma_{i-1}}{2\Delta y}\right)\right] \\ & + \frac{y_i}{z_T}\left(\frac{\nu_{i+1}p_{i+1} - \nu_{i+1}p_{i+1}}{2\Delta y}\right)\left(V_{S_{N+1}} + \frac{\dot{m_T}}{A_{N+1}\gamma_m}\right) \\ & + \frac{1}{A_i z_T^2}\left[\frac{p_{i+1}}{(\Delta y)^2}(\nu p A K)_{i+\frac{1}{2}} - \frac{p_i}{(\Delta y)^2}\left((\nu p A K)_{i+\frac{1}{2}} + (\nu p A K)_{i-\frac{1}{2}}\right) + \frac{p_{i-1}}{(\Delta y)^2}(\nu p A K)_{i-\frac{1}{2}}\right] \\ & - \frac{1}{A_i z_T}\frac{A_{i+1}V_{S_{i+1}}\nu_{i+1}p_{i+1} - A_{i-1}V_{S_{i-1}}\nu_{i-1}p_{i-1}}{2\Delta y}\Bigg\}.\end{aligned} \tag{5.38}$$

For $i = N+1$

$$p_{N+1} = 1 \Rightarrow \frac{\partial p_{N+1}}{\partial t} = 0. \tag{5.39}$$

Furthermore, we can introduce the following matrices:

$$\mathbf{C} = \begin{pmatrix} 0 & 0 & 0 & \cdots & 0 \\ \frac{1}{2} & -1 & \frac{1}{2} & \cdots & 0 \\ 0 & \ddots & \ddots & \ddots & 0 \\ 0 & \cdots & \frac{1}{2} & -1 & \frac{1}{2} \\ 0 & \cdots & 0 & 0 & 0 \end{pmatrix} \in R^{(N+1)\times(N+1)}, \tag{5.40}$$

$$\mathbf{D'} = \begin{pmatrix} 0 & 0 & 0 & \cdots & 0 \\ -\frac{1}{2} & 0 & \frac{1}{2} & \cdots & 0 \\ 0 & \ddots & \ddots & \ddots & 0 \\ 0 & \cdots & -\frac{1}{2} & 0 & \frac{1}{2} \\ 0 & \cdots & 0 & 0 & 0 \end{pmatrix} \in R^{(N+1)\times(N+1)}. \tag{5.41}$$

Then we can rewrite Eqs. (5.37)-(5.39) in a matrix form:

$$\begin{aligned}\frac{\partial \mathbf{p}}{\partial t} = \tilde{\boldsymbol{\nu}}.*\Bigg\{ & \frac{1}{\Gamma}\mathbf{p}.*\left[\frac{1}{\Delta y z_T}\mathbf{D'}\boldsymbol{\gamma}.*\mathbf{y}\left(V_{s,N+1} + \frac{\dot{m}_T}{\gamma_m A_{N+1}}\right) - \frac{1}{\Delta y z_T}\tilde{\mathbf{A}}.*\mathbf{D'}(\mathbf{A}.*\mathbf{V}_s.*\boldsymbol{\gamma})\right] \\ & + \frac{1}{\Delta y z_T}\mathbf{y}.*\mathbf{D'}(\boldsymbol{\nu}.*\mathbf{p})\left(V_{s,N+1} + \frac{\dot{m}_T}{\gamma_m A_{N+1}}\right) \\ & + \frac{1}{\Delta y^2 z_T^2}\tilde{\mathbf{A}}.*\left[\frac{1}{2}(\mathbf{p}^+.*\left(\boldsymbol{\alpha}^{\mathbf{c}} + \boldsymbol{\alpha}^+\right) - \mathbf{p}^{\mathbf{c}}.*\left(\boldsymbol{\alpha}^+ + 2\boldsymbol{\alpha}^{\mathbf{c}} + \boldsymbol{\alpha}^-\right) + \mathbf{p}^-.*\left(\boldsymbol{\alpha}^{\mathbf{c}} + \boldsymbol{\alpha}^-\right))\right] \\ & - \frac{1}{\Delta y z_T}\tilde{\mathbf{A}}.*(\mathbf{D'}(\mathbf{p}.*\boldsymbol{\nu}.*\mathbf{A}*.\mathbf{V}_s))\Bigg\}\end{aligned} \tag{5.42}$$

In Eq. (5.42) and thereafter

$$\boldsymbol{a}.*\boldsymbol{b} = [a_1 b_1, a_2 b_2, \dots a_{N+1} b_{N+1}]^T \quad \forall \mathbf{a} \text{ and } \mathbf{b}.$$

where $\mathbf{a}$ and $\mathbf{b}$ represent any vector used in the discretization. This results in the following relationships

$$\boldsymbol{\alpha}^- = [\nu_1 p_1 A_1 K_1, \nu_2 p_2 A_2 K_2, \dots \nu_{N-1} p_{N-1} A_{N-1} K_{N-1}]^T, \tag{5.43}$$

$$\boldsymbol{\alpha}^+ = [\nu_3 p_3 A_3 K_3, \nu_4 p_4 A_4 K_4, \dots \nu_{N+1} p_{N+1} A_{N+1} K_{N+1}]^T, \tag{5.44}$$

$$\boldsymbol{\alpha}^{\mathbf{c}} = [\nu_1 p_1 A_1 K_1, \nu_2 p_2 A_2 K_2, \dots \nu_N p_N A_N K_N]^T. \tag{5.45}$$

Equations for Pressure (Closed Tank Case)
In this case when the bottom of the tank is closed, the boundary condition is $\frac{\partial p}{\partial y} = 0$ at the bottom. Now the discrete analog of Eq. (5.33) becomes: For $i = 1$

$$\begin{aligned}\frac{\partial p_i}{\partial t} = \frac{1}{\nu_i}\Bigg\{ & \frac{p_i}{\Gamma}\Bigg[\frac{1}{\Delta y}(-\frac{3}{2}\gamma_1 + 2\gamma_2 - \frac{1}{2}\gamma_3)\frac{y_i}{z_T}\left(V_{S_{N+1}} + \frac{\dot{m_T}}{A_{N+1}\gamma_m}\right) \\ & -\frac{1}{A_i z_T}\left(\frac{1}{\Delta y}(-\frac{3}{2}A_1 V_{s_1}\gamma_1 + 2A_2 V_{s_2}\gamma_2 - \frac{1}{2}A_3 V_{s_3}\gamma_3)\right)\Bigg] \\ & + \frac{y_i}{z_T}\left(\frac{1}{\Delta y}(-\frac{3}{2}\nu_1 p_1 + 2\nu_2 p_2 - \frac{1}{2}\nu_3 p_3)\right)\left(V_{s_{N+1}} + \frac{\dot{m_T}}{A_{N+1}\gamma_m}\right) \\ & + \frac{1}{A_i z_T^2}\left(2\frac{p_2 - p_1}{\Delta y^2}(A_1\nu_1 p_1 k_1)\right) \\ & - \frac{1}{A_i z_T}\frac{1}{\Delta y}\left(-\frac{3}{2}A_1 V_{s_1}\nu_1 p_1 + 2A_2 V_{S_2}\nu_2 p_2 - \frac{1}{2}A_3 V_{S_3}\nu_3 p_3\right)\Bigg\}.\end{aligned} \tag{5.46}$$

For $i = 2, \ldots N$

$$\begin{aligned}\frac{\partial p_i}{\partial t} = \frac{1}{\nu_i}\Bigg\{ & \frac{p_i}{\Gamma}\Bigg[\frac{\gamma_{i+1} - \gamma_{i-1}}{2\Delta y}\frac{y_i}{z_T}\left(V_{s_{N+1}} + \frac{\dot{m_T}}{A_{N+1}\gamma_m}\right) \\ & -\frac{1}{A_i z_T}\left(\frac{A_{i+1}V_{s_{i+1}}\gamma_{i+1} - A_{i-1}V_{s_{i-1}}\gamma_{i-1}}{2\Delta y}\right)\Bigg] \\ & + \frac{y_i}{z_T}\left(\frac{\nu_{i+1}p_{i+1} - \nu_{i+1}p_{i+1}}{2\Delta y}\right)\left(V_{s_{N+1}} + \frac{\dot{m_T}}{A_{N+1}\gamma_m}\right) \\ & + \frac{1}{A_i z_T^2}\left[\frac{p_{i+1}}{(\Delta y)^2}(\nu p A K)_{i+\frac{1}{2}} - \frac{p_i}{(\Delta y)^2}\left((\nu p A K)_{i+\frac{1}{2}} + (\nu p A K)_{i-\frac{1}{2}}\right) + \frac{p_{i-1}}{(\Delta y)^2}(\nu p A K)_{i-\frac{1}{2}}\right] \\ & - \frac{1}{A_i z_T}\frac{A_{i+1}V_{s_{i+1}}\nu_{i+1}p_{i+1} - A_{i-1}V_{s_{i-1}}\nu_{i-1}p_{i-1}}{2\Delta y}\Bigg\}.\end{aligned} \tag{5.47}$$

For $i = N + 1$

$$p_{N+1} = 1 \Rightarrow \frac{\partial p_{N+1}}{\partial t} = 0. \tag{5.48}$$

By introducing matrix

$$\mathbf{F} = \begin{pmatrix} -\frac{3}{2} & 2 & -\frac{1}{2} & \cdots & 0 \\ -\frac{1}{2} & 0 & \frac{1}{2} & \cdots & 0 \\ 0 & \ddots & \ddots & \ddots & 0 \\ 0 & \cdots & -\frac{1}{2} & 0 & \frac{1}{2} \\ 0 & \cdots & 0 & 0 & 0 \end{pmatrix} \in R^{(N+1)\times(N+1)}, \tag{5.49}$$

we can represent Eqs. (5.46)-(5.48) in matrix form as

$$\begin{aligned}\frac{\partial \mathbf{p}}{\partial t} = \tilde{\boldsymbol{\nu}}.* \Bigg\{ & \frac{1}{\Gamma}\mathbf{p}.*\left[\frac{1}{\Delta y z_T}\mathbf{F}\boldsymbol{\gamma}.*\mathbf{y}\left(V_{s,N+1} + \frac{\dot{m}_T}{\gamma_m A_{N+1}}\right) - \frac{1}{\Delta y z_T}\tilde{\mathbf{A}}.*\mathbf{F}(\mathbf{A}.*\mathbf{V}_s.*\boldsymbol{\gamma})\right] \\ & + \frac{1}{\Delta y z_T}\mathbf{y}.*\mathbf{F}(\boldsymbol{\nu}.*\mathbf{p})\left(V_{s,N+1} + \frac{\dot{m}_T}{\gamma_m A_{N+1}}\right) \\ & + \frac{1}{\Delta y^2 z_T^2}\tilde{\mathbf{A}}.*\left[\frac{1}{2}(\mathbf{p}^+.*\left(\boldsymbol{\alpha}^{\mathbf{c}} + \boldsymbol{\alpha}^+\right) - \mathbf{p}\mathbf{c}.*(\boldsymbol{\alpha}^+ + 2\boldsymbol{\alpha}^{\mathbf{c}} + \boldsymbol{\alpha}^-) + \mathbf{p}^-.*\left(\boldsymbol{\alpha}^{\mathbf{c}} + \boldsymbol{\alpha}^-\right))\right] \\ & - \frac{1}{\Delta y z_T}\tilde{\mathbf{A}}.*\mathbf{F}(\mathbf{p}.*\boldsymbol{\nu}.*\mathbf{A}*.\mathbf{V}_s)\Bigg\}.\end{aligned} \tag{5.50}$$

Equations for Bulk Density
The discrete analog of Eq.(5.34) verifies the following system of equations: For $i = 1$

$$\frac{\partial \gamma_i}{\partial t} = \frac{1}{\Delta y}(-\frac{3}{2}\gamma_1 + 2\gamma_2 - \frac{1}{2}\gamma_3)\frac{y_i}{z_T}\left(V_{s,N+1} + \frac{\dot{m}_T}{\gamma_m A_{N+1}}\right) \quad + \frac{1}{A_i z_T \Delta y}\left(-\frac{3}{2}A_1 V_{s,1}\gamma_1 + 2A_2 V_{s,2}\gamma_2 - \frac{1}{2}A_3 V_{s,3}\gamma_3\right). \tag{5.51}$$

For $i = 2, \dots N$

$$\frac{\partial \gamma_i}{\partial t} = \frac{\gamma_{i+1} - \gamma_{i-1}}{2\Delta y}\frac{y_i}{z_T}\left(V_{s,N+1} + \frac{\dot{m}_T}{\gamma_m A_{N+1}}\right) \quad + \frac{1}{A_i z_T}\left(\frac{A_{i+1}V_{s,i+1}\gamma_{i+1} - A_{i-1}V_{s,i-1}\gamma_{i-1}}{2\Delta y}\right). \tag{5.52}$$

For $i = N + 1$

$$\gamma_{n+1} = \gamma_m \Rightarrow \frac{\partial \gamma_{N+1}}{\partial t} = 0. \tag{5.53}$$

We rewrite (5.51)-(5.53) in matrix form:

$$\frac{\partial \boldsymbol{\gamma}}{\partial t} = \left(\frac{1}{\Delta y z_T}\mathbf{F}\boldsymbol{\gamma}.^*\,\mathbf{y}\right)\left(V_{s,N+1} + \frac{\dot{m}_T}{\gamma_m A_{N+1}}\right) - \frac{1}{\Delta y z_T}\tilde{\mathbf{A}}.^*\mathbf{F}(\mathbf{A}.^*\boldsymbol{\gamma}.^*\mathbf{V}_s), \tag{5.54}$$

where $\boldsymbol{F}$ and $\tilde{\boldsymbol{A}}$ are as introduced earlier.
Equations for Velocity of Solid
The discrete equation for the velocity of solid along with the boundary conditions is stated as For $i = 1$

$$V_{s,1} = 0 \Rightarrow \frac{\partial V_{s,1}}{\partial t} = 0. \tag{5.55}$$

For $i = 2, \dots N$

$$\frac{\partial V_{s,i}}{\partial t} = -\frac{g}{\gamma_i}\left[\frac{1}{z_T}\frac{\sigma_{i+1} - \sigma_{i-1}}{2\Delta y} + \frac{\sigma_i}{A_i}\left(\left(\frac{dA}{dy}\right)_i \cdot \frac{1}{z_T} - C_i\right) + \frac{1}{z_T}\frac{p_{i+1} - p_{i-1}}{2\Delta y} + \gamma_i\right].$$
$$+\frac{y_i}{z_T}\frac{V_{s,i+1} - V_{s,i-1}}{2\Delta y} \cdot \left(V_{s,N+1} + \frac{\dot{m}_T}{\gamma_m A_{N+1}}\right) - \frac{V_{s,i}}{z_T}\frac{V_{s,i+1} - V_{s,i-1}}{2\Delta y}. \tag{5.56}$$

For $i = N + 1$

$$\frac{\partial V_{s,N+1}}{\partial t} = -\frac{g}{\gamma_{N+1}}\left[\frac{1}{\Delta y z_T}\left(\frac{1}{2}\sigma_{N-1} - 2\sigma_N + \frac{3}{2}\sigma_{N+1}\right) + \frac{\sigma_{N+1}}{A_{N+1}}\left(\left(\frac{dA}{dy}\right)_{N+1} \cdot \frac{1}{z_T} - C_{N+1}\right)\right.$$
$$\left.+\frac{1}{\Delta y z_T}\left(\frac{1}{2}p_{N-1} - 2p_N + \frac{3}{2}p_{N+1}\right) + \gamma_{N+1}\right] + \frac{1}{\Delta y z_T}\left(\frac{1}{2}V_{s,N-1} - 2V_{s,N} + \frac{3}{2}V_{s,N+1}\right)$$
$$\left(y_{N+1}\left(V_{s,N+1} + \frac{\dot{m}_T}{\gamma_m A_{N+1}}\right) - V_{s,N+1}\right). \tag{5.57}$$

Let us further introduce the matrix

$$\mathbf{B} = \begin{pmatrix} 0 & 0 & 0 & \cdots & 0 \\ -\frac{1}{2} & 0 & \frac{1}{2} & \cdots & 0 \\ 0 & \ddots & \ddots & \ddots & 0 \\ 0 & \cdots & -\frac{1}{2} & 0 & \frac{1}{2} \\ 0 & \cdots & \frac{1}{2} & -2 & \frac{3}{2} \end{pmatrix} \in R^{(N+1)\times(N+1)} \tag{5.58}$$

and the correction vector $\boldsymbol{\psi} = [0, 1, \cdots, 1]^T$. We can now represent Eqs.(5.55)-(5.57) in the following form:

$$\frac{\partial \boldsymbol{V}_s}{\partial t} = -g\tilde{\boldsymbol{\gamma}}.*\left[\frac{1}{\Delta y z_T}\mathbf{B}\boldsymbol{\sigma} + \boldsymbol{\psi}.*\boldsymbol{\sigma}.*\tilde{\mathbf{A}}.*(\frac{\boldsymbol{dA}}{\boldsymbol{dy}} \cdot \frac{1}{z_T} - \boldsymbol{C}) + \frac{1}{\Delta y z_T}\mathbf{B}\mathbf{p} + \boldsymbol{\gamma}.*\boldsymbol{\psi}\right]$$

$$+\frac{1}{\Delta y z_T} * \left[\mathbf{y}. * \left(V_{s,N+1} + \frac{\dot{m}_T}{\gamma_m A_{N+1}}\right) - \frac{1}{z_T}\mathbf{V}_s\right] . * \mathbf{BV_s}. \tag{5.59}$$

Final System of Equations
We combine Eqs.(5.42) or (5.50), (5.54), (5.59) and the discrete analog of Eq.(5.36) to form a system of ordinary differential equations, which are linear in time

$$\begin{cases} \dfrac{\partial \mathbf{p}}{\partial t} = F_1(\mathbf{p}, \boldsymbol{\gamma}), \\ \dfrac{\partial \boldsymbol{\gamma}}{\partial t} = F_2(\mathbf{V_s}, \boldsymbol{\gamma}), \\ \dfrac{\partial \mathbf{V_s}}{\partial t} = F_3(\mathbf{p}, \boldsymbol{\gamma}, \mathbf{V_s}), \\ \dfrac{dz_T}{dt} = \dfrac{g\dot{m}_T}{A_{N+1}\gamma_{N+1}} + V_{s,N+1}. \end{cases} \tag{5.60}$$

The system presented in Eq.(5.60) is a set of $3N + 4$ equations which can be solved by using existing ODE solvers, such as Runge-Kutta or forward Euler. In this paper the equations are solved using the ODE45 routine in Matlab.

5.4 Numerical results

Initially, the geometry, boundary conditions and material parameters are specified. However, before the system in Eq.(5.60) can be solved the initial condition on γ must be known. In order to obtain this condition the inertial effects of Eq.(5.16) are dropped resulting in

$$\frac{d\sigma}{dz} = -\frac{\sigma}{A}\frac{dA}{dz} - \frac{dp}{dz} + \frac{1}{A}\oint_c k\sigma(m_f \tan\phi' + \tan\theta)dc - \gamma. \tag{5.61}$$

This can be readily solved using any existing ODE Solver. In our case we again use the ODE45 routine found in the Matlab software program. This method is physically equivalent to examining a vessel that is initially full of material that is not flowing. The vessel contains some initial stress field which determines its density. After the initial stress field and density is determined the system of 1st order equations is solved. We present results for the more involved open tank case. Three cases will be discussed: steady-state, single fill-rate and dual fill-rate. We will first need to initialize the model by specifying both the geometry of the vessel and the initial boundary conditions. The following shows the parameters used in all three experiments.

- Geometry: Cylinder
- Material Parameters:

$\beta = 0.15$	$\alpha = 5$
$\Gamma = 200$ lbs/ft^3	$\sigma_m = 13$
$\gamma_0 = 100$ lbs/ft^3	$\gamma_m = 100$ lbs/ft^3
$\tan(\phi') = 0.5$	

- Boundary and Initial Conditions:
  - Initially, the atmospheric pressure at the boundaries and inside the tank are set to 2155.68 lbs/ft^2.
  - The stress at the top is 0 lbs/ft.

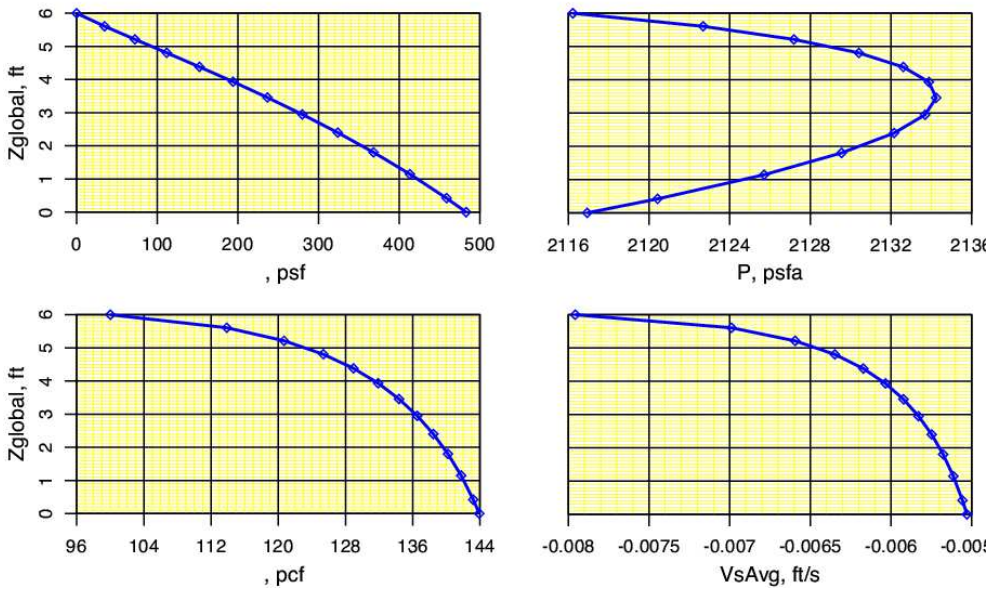

Figure 5.4: Stress(σ), pressure(P), density(γ) and velocity($VsAvg$) versus spatial domain (z) plots generated using the JJI software

5.4.1 Case 1: Steady-state

We want to compare our result with that generated by a proprietor software developed by Jenike & Johanson, Inc. We will refer to the software as JJI[7]. The solids flow rate, both in and out, were set at 10 lbs/sec. Hence, resulting in the steady-state case. Also, $K_0 = 0.000208$ ft/sec and $Vs_b = -0.005529$ ft/sec^2. The initial powder height was set at $z_T(0) = 6$ ft. Figure 5.4 shows four plots generated using the JJI software. They are:

- Stress (σ) versus spatial coordinate z,
- Pressure(P) versus spatial coordinate z,
- Density(γ) versus spatial coordinate z and
- Velocity($VsAvg$) versus spatial coordinate z.

These are 2-D graphs. Figures 5.5, 5.6, 5.7 and 5.8 show the corresponding plots generated using our program. However, instead of the spatial domain z, these plots are plotted with respect to the fixed spatial domain y. Refer to Eq. 5.28 for the relation between z and y. The plots generated by our code are 3-D graphs. By slicing the 3-D plots in time, one can quickly verify that the respective plots generated by both models are comparable.

5.4.2 Case 2: Single Fill-Rate

In this section, we want to study the effect of fill-rate on powder height (z_T) in the cylinder when the same total amount of material is added into the bin. We set $K_0 = 0.001$ ft/sec and $Vs_b = -0.025$ ft/sec^2.The initial powder height was set at 2 ft and no in-flow, i.e., $\dot{m}_t = 0$, during the first 5 seconds of the experiment. We then changed the fill-rate ($\dot{m}_t$) to some constant for the remaining time of the experiment. By varying the fill-rate, four plots were generated. Refer to Figure 5.9. It can be observed that with a higher fill-rate, the height of the powder in the vessel rises higher since the material has lesser time to deaerate given that the same total mass of solids were added in all cases.

[7]For more information, refer to http://www.jenike.com/

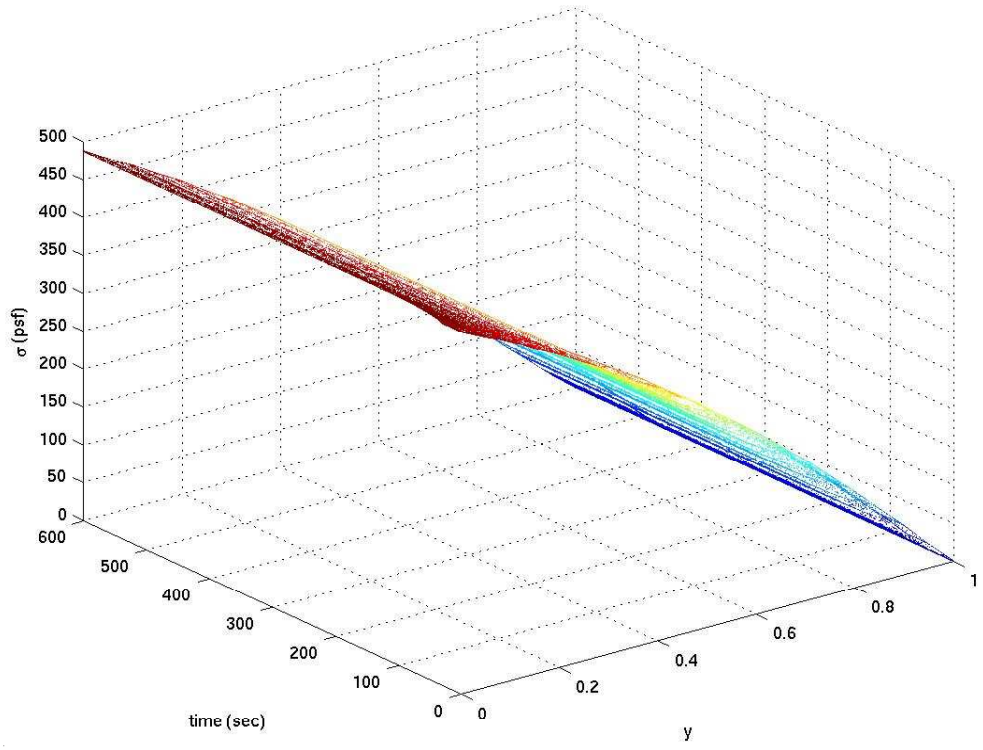

Figure 5.5: Plot of stress (σ) versus fixed spatial domain y versus time t

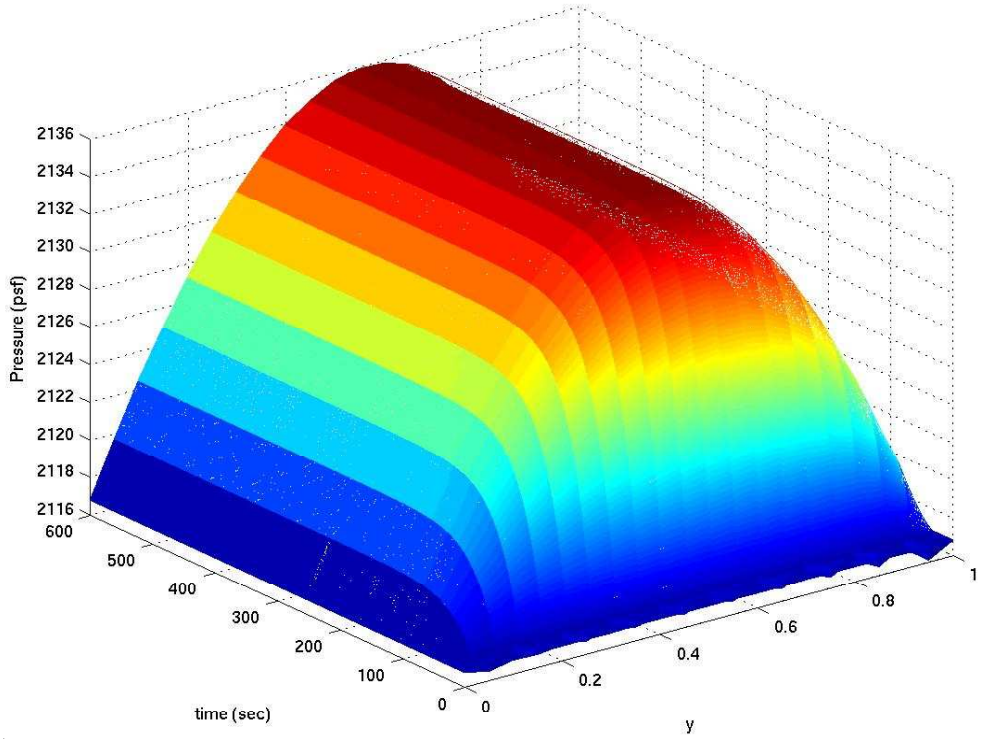

Figure 5.6: Plot of pressure (P) versus fixed spatial domain y versus time t

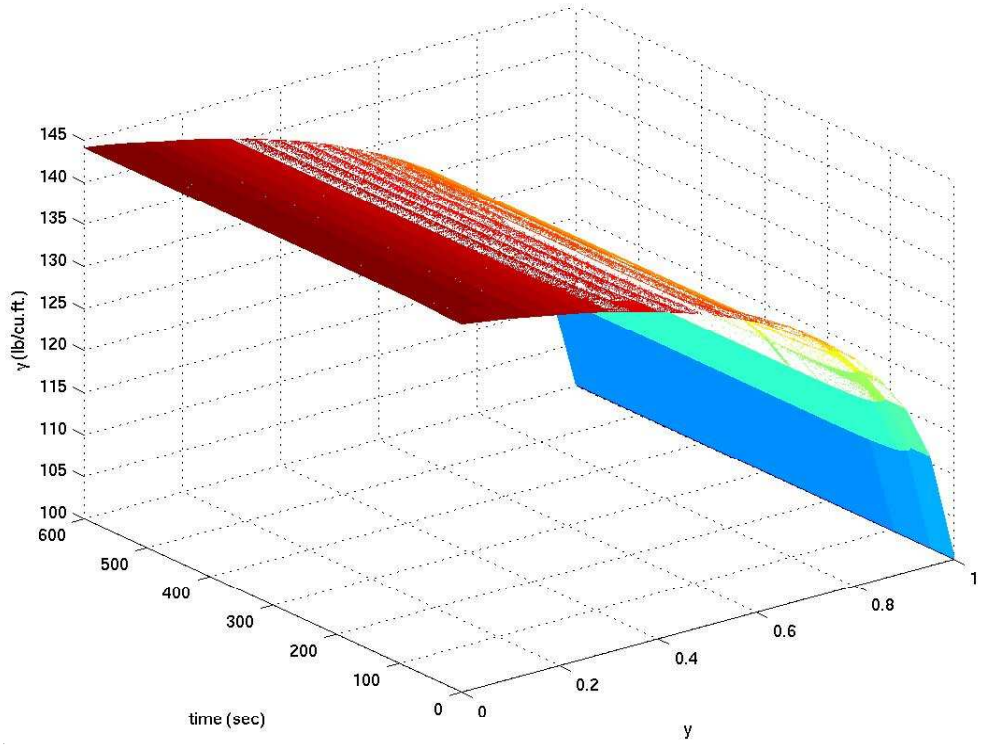

Figure 5.7: Plot of density (γ) versus fixed spatial domain y versus time t

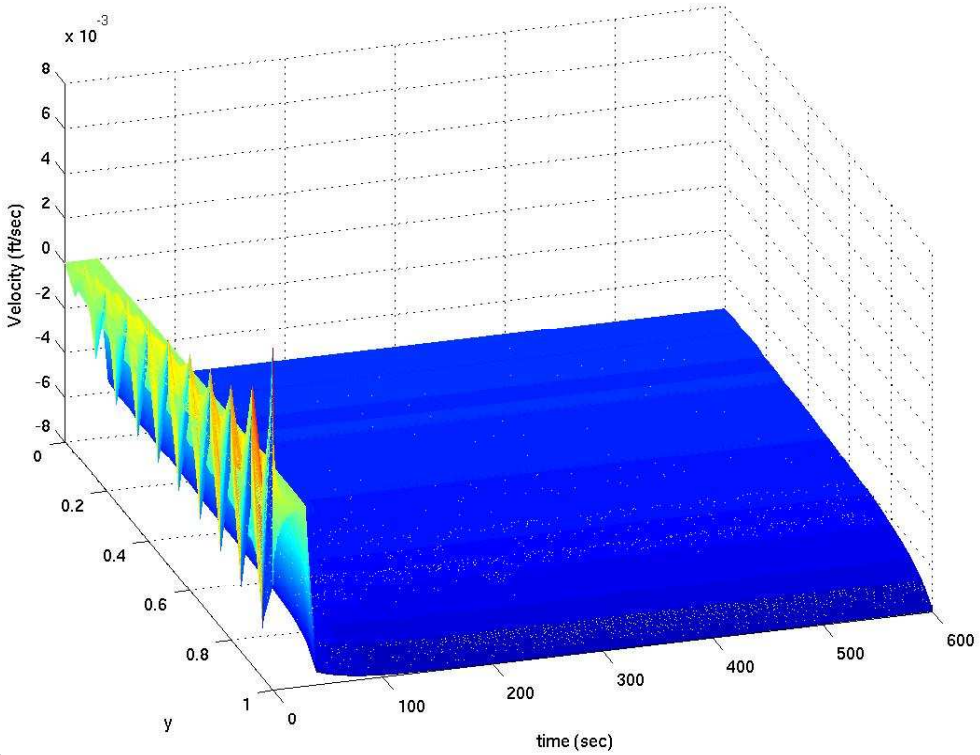

Figure 5.8: Plot of velocity V versus fixed spatial domain y versus time t

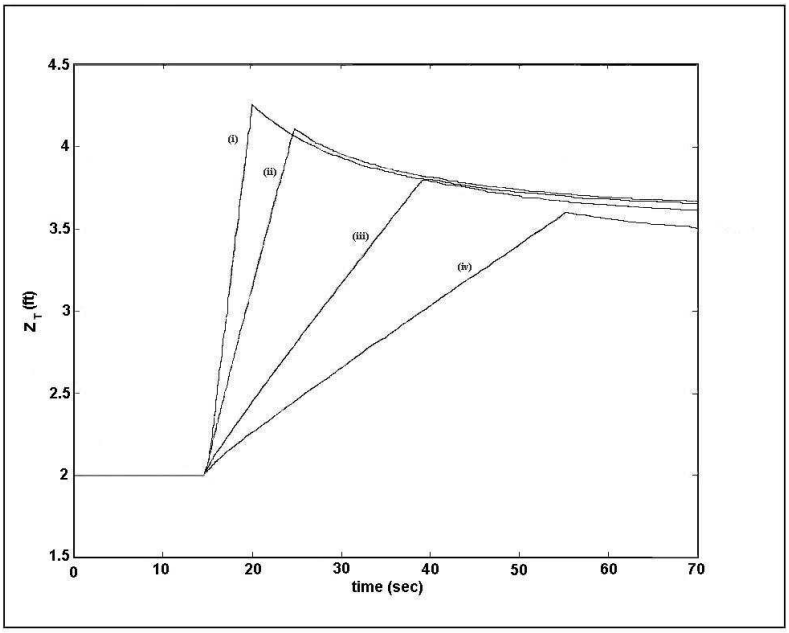

Figure 5.9: Effect of fill rate on powder height. Here, (i) fill-rate = 658 lbs/sec, (ii) fill-rate = 329 lbs/sec or half the fill-rate of (i), (iii) fill-rate = 131.6 lbs/sec or one-fifth the fill-rate of (i) and (iv) fill-rate = 65.8 lbs/sec or one-tenth the fill-rate of (i).

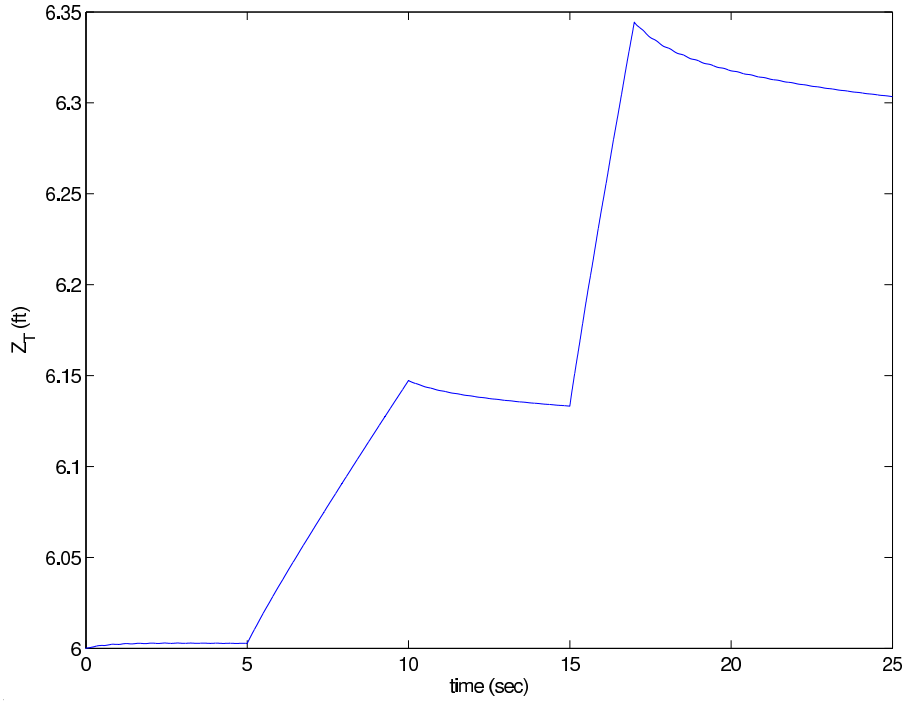

Figure 5.10: Effect of change in fill-rate on powder height.

5.4.3 Case 3: Dual fill-rate

In this experiment, we changed the fill-rate within a single experiment and examined its effect on the powder height in the vessel. Similar boundary conditions as Section 5.4.2 were used except that the initial powder height was set at 6 ft and the fill-rate was set as follows:

$$\dot{m}_t = \begin{cases} 0 \text{ lbs/sec} & \text{if } t < 5 \\ 47 \text{ lbs/sec} & \text{if } 5 \leq t < 10 \\ 0 \text{ lbs/sec} & \text{if } 10 \leq t < 15 \\ 161 \text{ lbs/sec} & \text{if } t \geq 15 \end{cases}$$

Figure 5.10 shows the change in powder height and Figure 5.11 shows the effect of pressure on the bin.

5.5 Conclusion and Future Work

The model formulation we proposed in this project is applicable to the study of the effect of interstitial gas on powder flow in various geometries of silos. Our model differs from previous research work [1, 2, 3, 5] in the sense that the effect of the inertial of solid particles is considered. In section 5.4, we demonstrated that our model was consistent in behavior to JJI, a proprietory software for steady-state calculations. Further, the effect of changing fill-rate on the powder height was also studied. Our current code appears to work well when the geometry is a cylinder. Hence, future work with such geometry can be extended to the study of solids flow with different internal friction values or even different in/out flow rates in the open tank case. A few preliminary runs were conducted with the use of a different geometry, in particular, a cylindrical structure mounted on top of a cone. With this cylinder-cone geometry, we found that when the slope of cone is too gentle or not steep enough, powder accumulates around the cone thus stopping powder discharge. Further investigation is required. It is possible that our 1-D model is over simplified and thus renders difficulties in understanding this unstable behavior. Perhaps, a 3-D model may be required to better analyze this flow problem. Other possible future work includes dimensionless analysis. Such an analysis will allow us to single out dominant terms that affects the behavior of solid flow in our model.

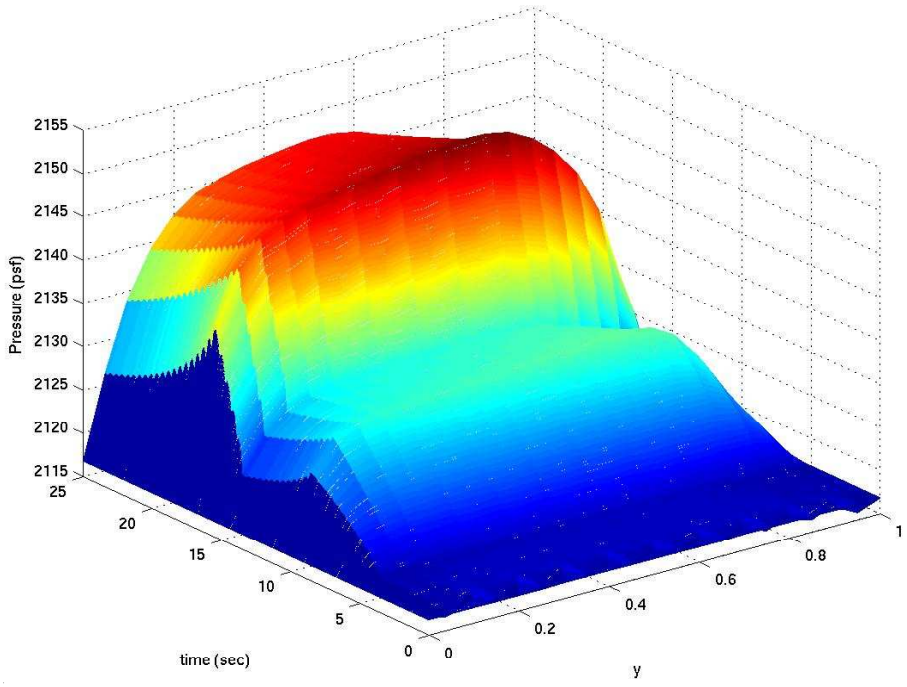

Figure 5.11: Effect of change in fill-rate on pressure on the vessel. Here, y represents the fixed spatial domain.

Acknowledgments

The participants would like to thank Dr. Pierre Gremaud and Mr. T. Anthony Royal for all their help. The project would not have been possible without their wealth of knowledge and incredible patience.

Bibliography

[1] K. A. Coffey, P. A. Gremaud, *Numerical Simulation of Aerated Powder Consolidation*, International Journal of Non-Linear Mechanics, 38 (2003) 1185–1194

[2] P. A. Gremaud, C. T. Kelley, T. A. Royal, K. A. Coffey, *On a powder consolidation problem*, SIAM Journal of Applied Mathematics, 62 (2001), pp. 1–20

[3] J. R. Johanson, A. W. Jenike, *Settlement of Powders in Vertical Channels Caused by Gas Escape*, ASME Journal of Applied Mechanics, 39 (1972), pp. 863–868

[4] T.A. Royal, *Analysis of Pressurization of Lock Hoppers and Typical Measured Flow Properties of Coal*, Technical report DOE/MC/14101-1126, DOE publication

[5] D. Schulze, *A Theoretical Model for the Prediction of the Gas Pressure Distribution in Silos at Filling and Discharge*, Proceedings: Reliable Flow of Particulate Solids III, Porsgrunn, Norway, 11th-13th August, 1999, pp. 331–340

[6] A. W. Jenike, *A theory of flow of particulate solids in converging and diverging channels based on a conical yield function*, Powder Tech., 50 (1987), pp. 229-236

Chapter 6

Planning and Scheduling Strategy for Non-Deterministic Events

Edward Bakewell[1], Dong-Kyoung Choe[2], Minh HaQuang[3], Sirisha Kala[4], Stacey Lawler[5], Robert Schoen[6]
Aaron Thatcher[7]

Problem Presenter:
Pierre Maldague
Jet Propulsion Laboratory

Faculty Consultants:
Kazufumi Ito and Hien T. Tran

Abstract

Efficient planning and scheduling of activities performed by a rover in an unknown environment requires a complex strategy. This strategy must maximize the number of tasks while maintaining a high probability of completion. The number of activities combined with their respective durations must be coordinated to fit within a finite time interval as determined by the availability of solar power. In organizing these activities, a variety of scientific and mathematical methods are helpful, including optimization techniques used in linear programming, randomized sequence generation, and the design and implementation of a command and data handling subsystem. Using these methods, we developed a system that optimizes the effectiveness of the rover in achieving specific goals.

6.1 Introduction and Motivation

The Jet Propulsion Laboratory (JPL) is the NASA center that specializes in robotic exploration of the solar system. They are currently in the process of sending two rovers to Mars as part of the Mars Exploration Rover (MER) project. In terms of planning and scheduling, the MER mission is largely based on deterministic

[1]University of North Carolina - Wilmington
[2]North Carolina State University
[3]Brown University
[4]Mississippi State University
[5]Murray State University
[6]University of North Carolina - Asheville
[7]University of North Carolina - Wilmington

strategies. A full staff is required to be at JPL at all times for handling the sol-to-sol operation of the rovers, where sol is the Martian day. A future mission called Mars Science Laboratory (MSL) will take place near the end of the decade. One of the goals of MSL is to dramatically increase the amount of onboard autonomy to reduce the amount of staff required for rover operation. The challenge that JPL faces is to develop a new methodology to achieve this goal while providing the scientists sufficient freedom to perform the experiments in which they are interested.

With the help of Dr. Pierre Maldague, a developer on the MER planning team, we formulate a planning problem adapted from the Mars missions to model some of the basic sol-to-sol activities of the actual rover. In our model, the rover is required to perform a number of tasks while complying with the constraints restricting the activities. Each task has its own range of durations that must be taken into consideration when determining whether the rover has enough time to complete the tasks. Our goals are for the rover to have minimal idle time and perform the most activities possible.

Our model is separated into three sections: linear planner, sequence generator, and final execution module. By using a linear programming package in MATLAB, we optimize the number of instances of each activity that the rover should be able to complete depending on our goals. Our goals range from conservative, with a higher probability of completion, to aggressive, with more tasks but a lower probability of completion. We organize a possible schedule of activities for each sol with the sequence generator. Each possible sequence is checked multiple times with different durations per activity to determine whether the sequence can be completed in the available time. By executing the sequence many times using the randomly generated durations, we obtain an estimation of the probability of completion. This approach is a basic implementation of the Monte Carlo method. We are interested in a system of non-deterministic events which, based on a given risk level, optimizes the number of activities performed each sol.

6.2 Preliminary

Consider the following four types of activities:

- (A) Acquisition of data, for example taking image of some object or scene.
- (D) Downlink the data from the spacecraft to Earth
- (C) Calibration of the scientific instruments used for acquiring data
- (T) Traverse

These activities obey the following rules:

I They all must occur within a Planning Horizon, denoted H, that runs from 6:00 am until 6:00 pm (in Martian time)

II The duration of each activity is unknown in advance, but the duration of each activity follows some given preliminary distribution.

III Downlink can occur only at a certain time of the sol when the spacecraft is in view of Earth. This time period is called the Window of Opportunity (O). The duration for the downlink ranges between five minutes to two hours (120 minutes). For simplicity, let us assume for now that this window starts at 11:00 am.

IV If the spacecraft is to acquire data during the sol, the instruments used for the acquisition must be calibrated.

V Each activity is given a priority which may vary from sol to sol.

VI The time is measured in Martian minutes, which are actually slightly longer than minutes on Earth.

Goal: We want to find the number of activities for each type that maximizes the weighed total number of activities and the associated probability of completion.

6.3 The Optimization Problem

6.3.1 Objective Function

Let M_i denote the number of activities of type i where $i \in \{A, D, C, T\}$. Let λ_i denote the priority of activities of type i, $i \in \{A, D, C, T\}$. We thus need to maximize the following objective function:

$$\sum_{i \in A,D,C,T} M_i \lambda_i = M_A \lambda_A + M_D \lambda_D + M_C \lambda_C + M_T \lambda_T, \tag{6.1}$$

which is **linear** in the four variables M_A, M_D, M_C, M_T.

Let us assume for now that there is only one downlink in one day (during the window of opportunity) and there is exactly one calibration in one day (whether or not any acquisition will occur). Thus we have:

$$M_D = 1, M_C = 1. \tag{6.2}$$

Because of this assumption, we can split M_A into two parts:

$$M_A = M_A^b + M_A^a, \tag{6.3}$$

where M_A^b denotes the number of acquisitions performed **before** the downlink of data, and M_A^a denotes the number of acquisitions performed **after** the downlink operation. We are thus led to the maximization of the following simpler objective function:

$$M_A^b \lambda_A + M_A^a \lambda_A + M_T \lambda_T, \tag{6.4}$$

which is **linear** in the three variables M_A^b, M_A^a, M_T.

6.3.2 Effective Duration of Activities

Let D_i^{eff} denote the effective duration of activities of type i, $i \in \{A, D, C, T\}$. We assume further that this effective duration lies in a given range $[D_i^{min}, D_i^{max}]$. We will let

$$D_i^{eff} = \frac{\alpha}{100} D_i^{min} + (1 - \frac{\alpha}{100}) D_i^{max}, \tag{6.5}$$

where the real factor $\alpha \in [0, 100]$ determines a convex combination of best and worst case scenarios of the time it takes for the spacecraft to carry out an activity: $\alpha = 0$ corresponds to the worst case (it takes the spacecraft the longest possible time to carry out activity i which is D_i^{max}), $\alpha = 100$ corresponds to the best case (it only takes time D_i^{min}).

6.3.3 Constraints

Since the downlink occurs sometime in the middle of the day, any data that is acquired after the downlink must wait until the next day to be transmitted back to Earth. Let us denote by B this amount of backlog data and B_{max} the maximum amount of space available for storage (measured in Mb).

Let R_A, R_D denote the rate of data acquisition and download in Mb/min, respectively. Then the effective duration of downlink is given by:

$$D_D^{eff} = \frac{R_A M_A^b D_A^{eff} + B}{R_D}. \tag{6.6}$$

Since this duration must lie between 5 and 120 minutes, we are led to the constraints:

$$5 \leq \frac{R_A M_A^b D_A^{eff} + B}{R_D} \leq 120. \tag{6.7}$$

The amount of data obtained after the downlink must not exceed the maximum memory capacity, thus

$$R_A M_A^a D_A^{eff} \leq B_{max}. \tag{6.8}$$

Since the window of opportunity starts at 11:00 am, all morning acquisitions plus the calibration must occur between 6:00 am and 11:00 am, that is in a time frame of 300 minutes. We thus need

$$M_A^b D_A^{eff} + D_C^{efff} \leq 300. \tag{6.9}$$

Likewise, all afternoon acquisitions and the downlink must fit within the 420 minutes time frame between 11:00 am and 6:00 pm. Thus

$$M_A^a D_A^{eff} + \frac{R_A M_A^b D_A^{eff} + B}{R_D} \leq 420. \tag{6.10}$$

The total durations of all activities must NOT exceed the duration of the horizon, hence we need the following constraint:

$$(M_A^b + M_A^a) D_A^{eff} + M_D D_D^{eff} + M_C D_C^{eff} + M_T D_T^{eff} \leq D_H. \tag{6.11}$$

In the case when $M_C = M_D = 1$ and $D_H = 12$ hours $= 720$ minutes we obtain:

$$(M_A^b + M_A^a) D_A^{eff} + \frac{R_A M_A^b D_A^{eff} + B}{R_D} + D_C^{eff} + M_T D_T^{eff} \leq 720. \tag{6.12}$$

We will add the following heuristic constraint

$$\beta(M_A^b + M_A^a) \leq M_T, \tag{6.13}$$

where $\beta > 0$ is a balancing parameter that controls the number of traverses relative to the number of acquisitions.

6.3.4 Problem Summary

We are thus led to the following **Linear Programming Problem**:
Maximize $M_A^b \lambda_A + M_A^a \lambda_A + M_T \lambda_T$ subject to the constraints

1. $5 \leq \frac{R_A M_A^b D_A^{eff} + B}{R_D} \leq 120$
2. $R_A M_A^a D_A^{eff} \leq B_{max}$
3. $M_A^b D_A^{eff} + D_C^{eff} \leq 300$
4. $M_A^a D_A^{eff} + \frac{R_A M_A^b D_A^{eff} + B}{R_D} \leq 420$
5. $(M_A^b + M_A^a) D_A^{eff} + \frac{R_A M_A^b D_A^{eff} + B}{R_D} + D_C^{eff} + M_T D_T^{eff} \leq 720$
6. $\beta(M_A^b + M_A^a) \leq M_T$
7. $M_A^b \geq 0$, $M_A^a \geq 0$, $M_T \geq 0$

6.4 Implementation

We build an **Optimizing Plan Generator** consisting of three parts:

1. A **Linear Planner** that generates the numbers of activities such that the above rules are all satisfied. We have shown that this is a linear programming maximization problem.
2. A **Random Sequence Generator** that, given the numbers of activities output by the Linear Planner, generates a sequence of activities in random order.
3. An **Execution Module** that, given the sequence of activities from the Sequence Generator, carries out a plan for these activities and computes the probability of completion of the plan.

The next section gives a more detail description of these modules.

6.4.1 Linear Planner

Module: Linear Planner

Input:
Data rates R_D, R_A Priorities $\lambda_A, \lambda_T, \lambda_C$ Duration ranges $D_A^{min}, D_A^{max}, D_C^{min}, D_C^{max}, D_T^{min}, D_T^{max}$ Aggressiveness parameter α Balancing parameter β Backlog data (from previous day) B Memory capacity B_{max} Duration of the planning horizon D_H Opportunity window (S_O, E_O)
Output:
Numbers of activities of each type: M_A^b, M_A^a, M_T

Finding the optimal number of activities for each type is an integer programming problem. However, for the sake of simplicity and high probability of completion of the activities, we relax the optimization problem to linear programming problem. When the linear programming tool finds decimal numbers for the optimal solution, our linear planner rounds down to get a integer number. This module is implemented using MATLAB's linear programming toolbox, with the constraints stated above.

6.4.2 Sequence Generator

Module: Sequence Generator

Input:
Numbers of activities of each type M_A^b, M_A^a, M_T
Output:
An ordered sequence of activities that satisfies all the defined constraints

This module is implemented by a MATLAB program using a random number generator. The program randomly generates a sequence of activities according to a chosen probability distribution. This sequence must be manipulated in such a way that it can be more applicable to the situations actually encountered by the rover. In our system, this requires the rover not to complete two consecutive traverses, as we would not expect the rover to travel to one location and leave immediately to another without collecting any data.

6.4.3 Execution

Module: Execution

Input:
Sequence of activities (plan) Duration ranges $D_A^{min}, D_A^{max}, D_C^{min}, D_C^{max}, D_T^{min}, D_T^{max}$ Backlog data (from previous day) B Opportunity window (S_O, E_O) Data rate for downlink (R_D)
Output:
Estimated probability of completion of the plan Carry over data for the next day B

The execution module, also implemented in MATLAB, takes the randomly generated sequence, which we now consider the proposed schedule of activities for a given sol. With the aid of a 'proceed' function, the module determines whether this schedule can successfully be completed by the rover with a high percentage of probability. In order to accomplish this we utilize a basic implementation of the Monte Carlo method. This method helps to estimate the probability of success by iterating the sequence through the program several times.

6.5 Experiments

Let $R_A = 5$ (Mb/min), $R_D = 60$ (Mb/min), $B = 1500$, $B_{max} = 7200$ (Mb), $\beta = 0.2$. Let the probability distribution used in the random sequence generator be the uniform distribution. We consider the following two different assumptions:

Coefficients	Assumption 1	Assumption 2
λ_A	5	3
λ_C	0	0
λ_T	3	5
λ_D	0	0
D_A^{max}	30	30
D_A^{min}	15	15
D_C^{max}	30	30
D_C^{min}	15	15
D_T^{max}	20	150
D_T^{min}	10	90

Table 6.1: Two assumptions

The results of the experiments are plotted in figures $1-4$. Figure 1 and Figure 2 show typical examples of activity sequences for a sol. As we can see, in these specific cases a rover is completing its given tasks in the time horizon. Note that each block can be a series of different instances of the same activity type occuring continuously.

In Figure 3 and Figure 4, two different approaches are implemented for the execution module. In the first approach, we use one sequence of activities for one entire sol. In the second, we use two sequences of activities: one for the period before downlink and one for the period after downlink. As we can see in the figures, the

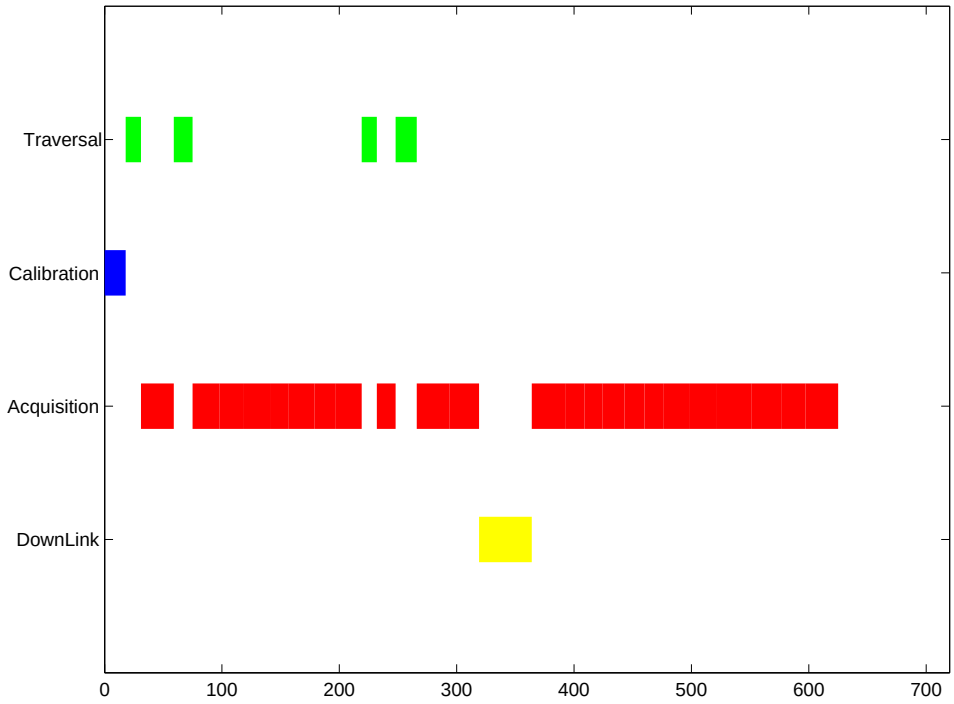

Figure 6.1: A random sequence of activities when $\alpha = 50$

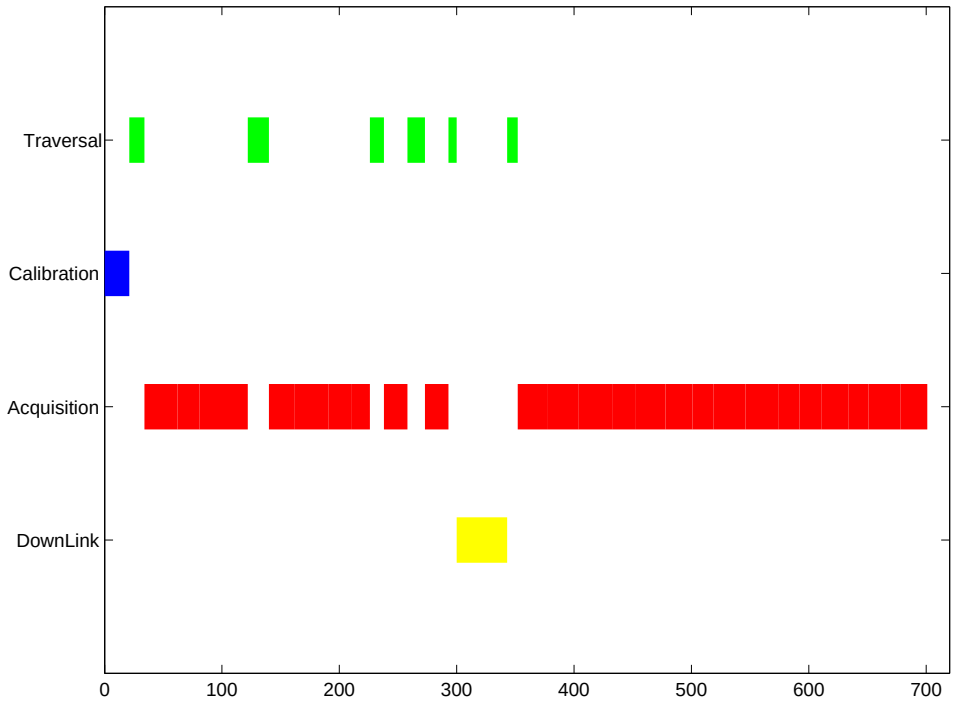

Figure 6.2: A random sequence of activities when $\alpha = 70$

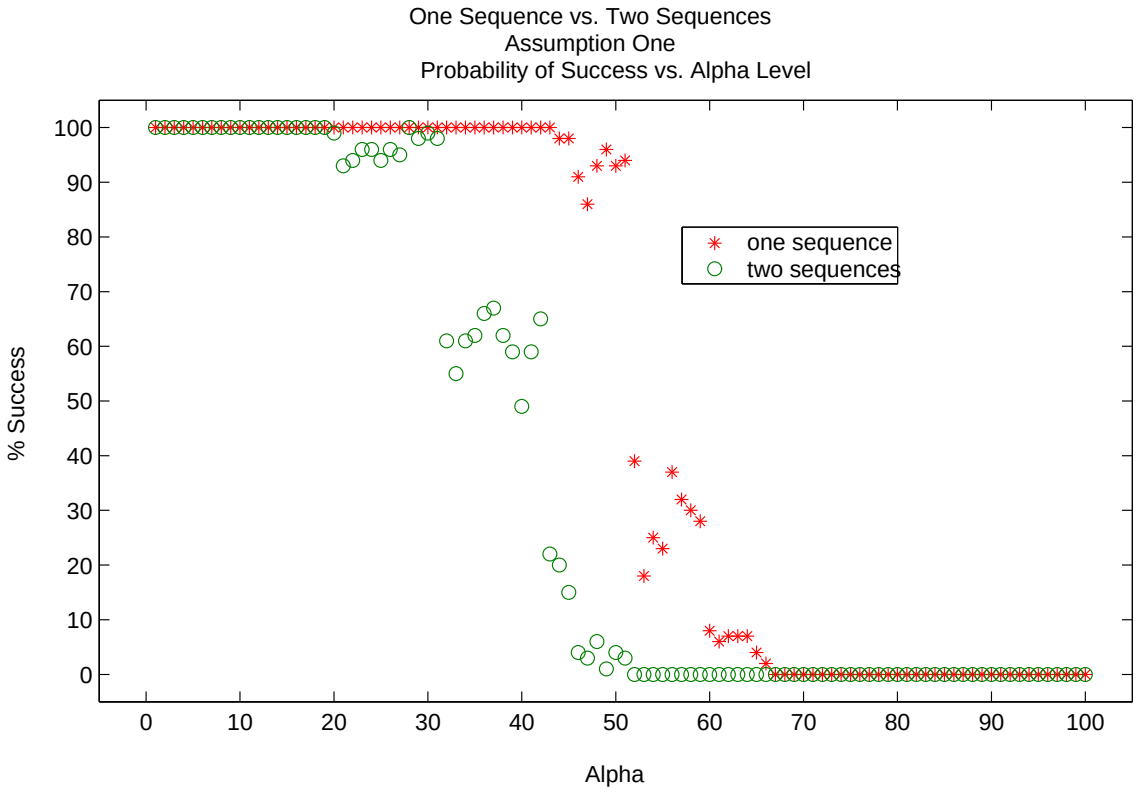

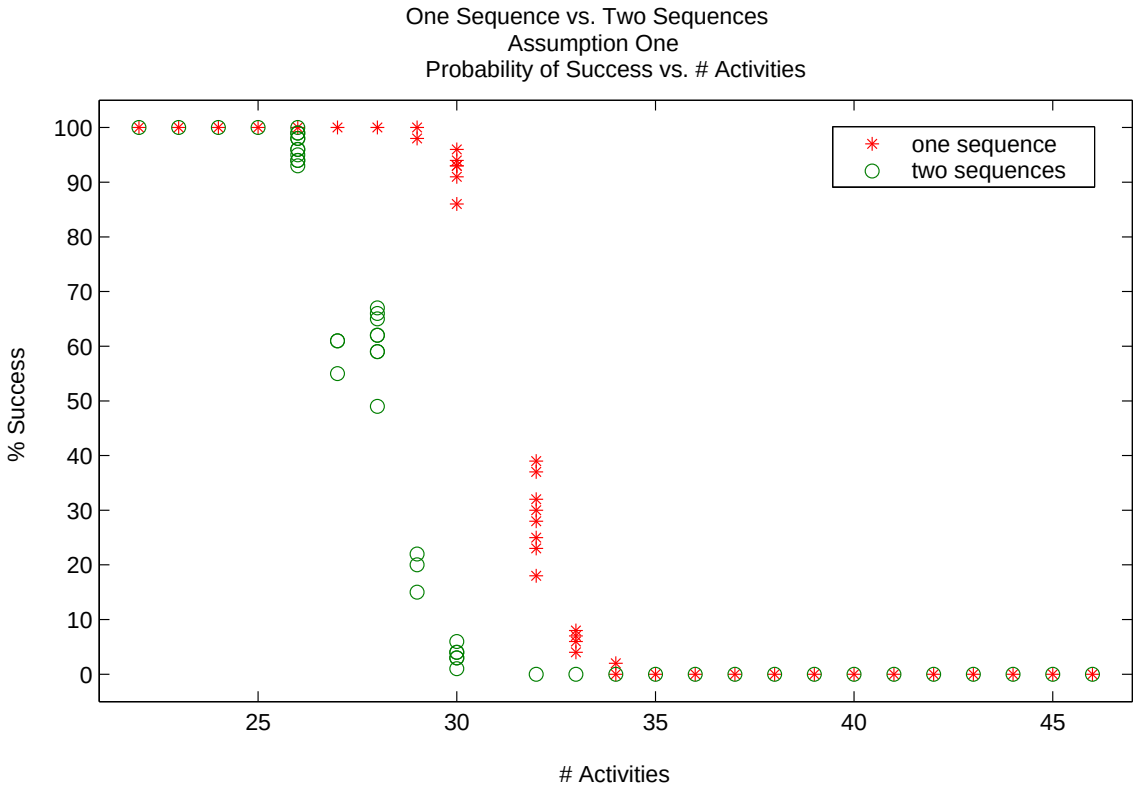

Figure 6.3: Probability of Success using Assumption One

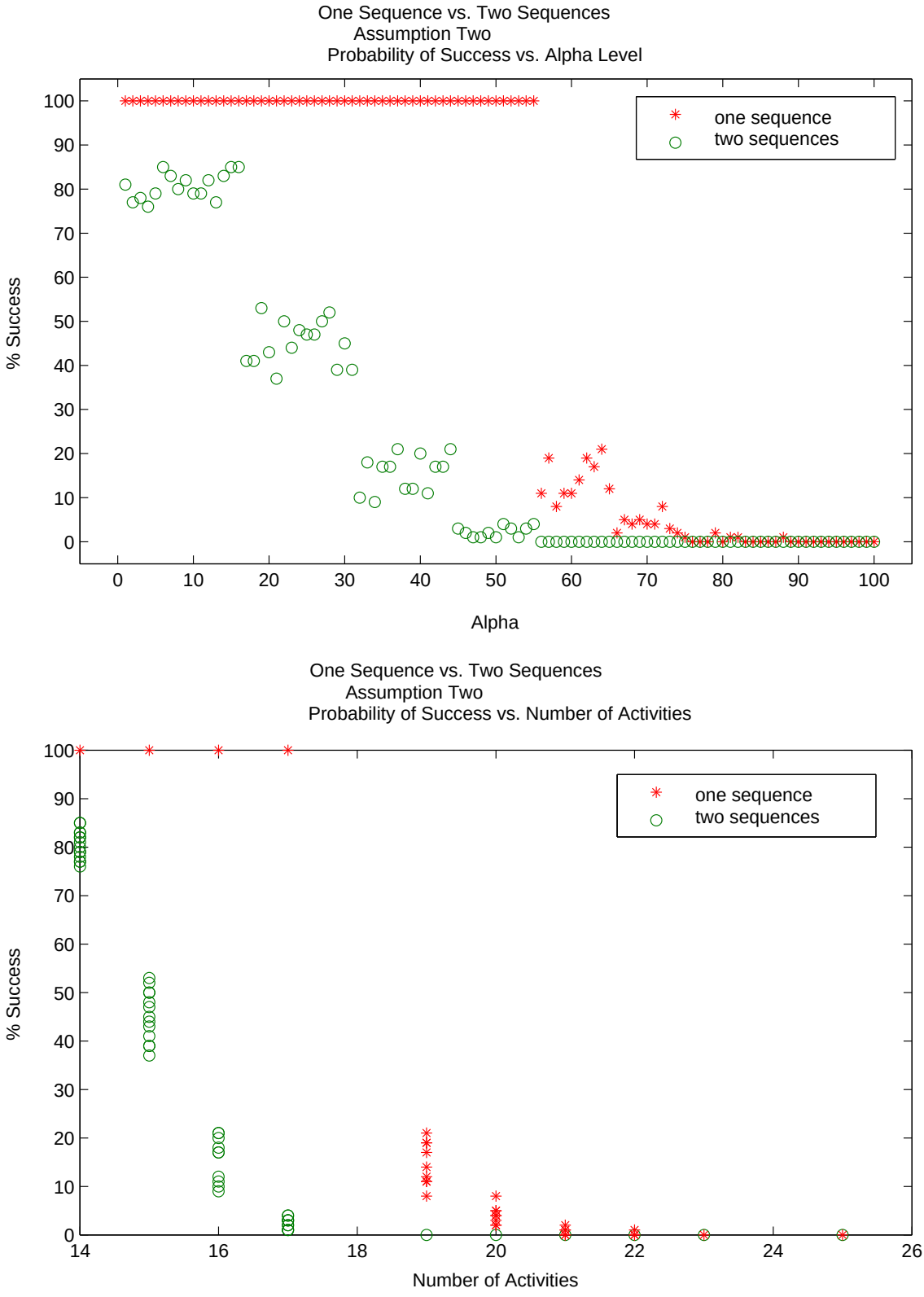

Figure 6.4: Probability of success using Assumption Two

one-sequence approach yields a higher probability of completion than the two-sequence approach does. The aggresive parameter, α, which controls the effective duration of each activity, is increased by one from zero to 100. For each plan of activities given by an α, 100 randomly selected durations of activities are applied to find the probability of completion of the plan. It can be seen that the probability of completion is high when α is small which corresponds to a conservative approach. This probability decreases when α is large, which corresponds to an aggressive approach. This result is in agreenment with our intuitition: the smaller the actual durations of the activities are, the higher the chance of a plan to be completed is.

One interesting finding is that at a certain degree of aggressiveness, the determinating factor for the total number of activities, the probability of success dramatically drops. Therefore, even though the durations of activities are not determined at the point of planning and scheduling, there is a limit for the number of activities that one can assign to the rover in a planning period. However, when we look at the points scattered between two extreme percentages of success, it is expected to see more mid-percentage points as we elaborate the increase of α. When midpoints are found, we will be able to increase the number of activities to be assigned to the rover considering the compensable loss of probability of success.

6.6 Conclusions and Future Work

We have built a planning system for non-deterministic events using a combination of linear programming and randomization techniques. In the system, an aggressiveness parameter, α, plays the most important role by outputting the probability of success for a possible plan. With the guidance of probability of success, non-deterministic events planners can control the number of activities in a plan based on their interests. Once the tolerable risk level is known, the system provides the best possible number of events that can be planned per time period.

The planning system introduced here considers a limited number of activities and constraints. It is left as a future goal to model a planning system considering a higher number of activities, particularly those that are time dependent. In addition, it would be interesting to see how the activities can be planned and scheduled when the rover can execute more than one thread of activities simultaneously.

6.7 Acknowledgements

We would like to thank Dr. Pierre Maldague for his help in our research, and for his willingness to extend the project from JPL. Not only did he contribute his time and knowledge of the project, but he offered much guidance along the way. We would also like to acknowledge the helpfulness and assistance of our faculty consultants, Dr. Kazufumi Ito and Dr. Hein T. Tran.

Bibliography

[1] Ai-Chang, Mitch; Bresina, John; Charest, Leonard; Hsu, Jennifer; Jonsson, Ari K.; Kanefsky, Bob; Maldague, Pierre; Morris, Paul; Rajan, Kanna; Yglesias, Jeffrey. Mixed-initiative activity planning for the Mars Exploration Rover mission.

http://icaps03.itc.it/satellite_events/documents/sd/01/jonsson.pdf (accessed July 2003)

[2] Athena Mars Exploration Video Simulation Page.

http://athena.cornell.edu/the_mission/rov_video.html (accessed July 2003)

[3] Backes, Paul G.; Norris, Jeffrey S.; Powell, Mark W.; Vona, Marsette A.; Steinke, Robert; Wick, Justin. The Science Activity Planner for the Mars Exploration Rover Mission: FIDO Field Test Results.

http://robotics.jpl.nasa.gov/people/jnorris/SAP-IEEEAS03.pdf (accessed July 2003)

[4] Jet Propulsion Laboratory webpage, Mars Exploration Mission: Surface Operations.

http://mars.jpl.nasa.gov/mer/mission/tl_surface.html (accessed July 2003)

[5] Rajan, Kanna. "MAPGEN Mixed Initiative Activity Plan Generator for MER" Mars Exploration Rover Planning and Sequencing Information Systems Workshop, September 5, 2002.

http://is.arc.nasa.gov/AR/slides/MERPln02.pdf (accessed July 2003)